TÉCNICO LISBOA

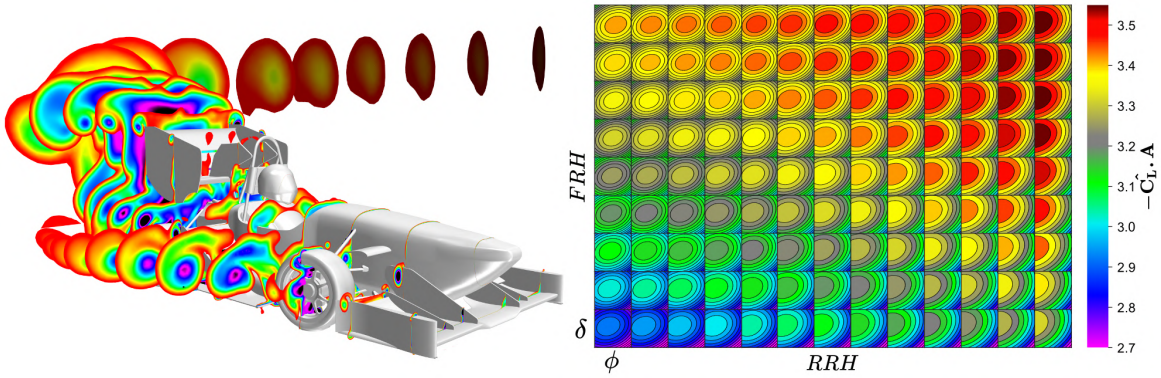

Aerodynamic Mapping of a Formula Student Prototype using Numerical Simulations and On-track Validation

Miguel Marques Carreira

Thesis to obtain the Master of Science Degree in

Aerospace Engineering

Supervisors: Prof. André Calado Marta
Prof. Luís Rego da Cunha Eça

Examination Committee

Chairperson: Prof. Filipe Szolnoky Ramos Pinto Cunha
Supervisor: Prof. André Calado Marta
Member of the Committee: Prof. José Manuel Da Silva Chaves Ribeiro Pereira

June 2022

Dedicated to my parents

Acknowledgments

The development of this dissertation would not be possible without the help and support of many people. I would like to express my gratitude and appreciation for both my supervisors Professor André Marta and Professor Luís Eça whose guidance, analysis, insights and encouragement have been invaluable throughout this study.

Many thanks to the Formula Student Técnico team for making this work possible. Much effort has been made by team members to organize and execute a testing day for aerodynamic validation and I am grateful to them all. Particular thanks go to André Correia, Pedro Oliveira, Miguel Valverde and Diogo Jerónimo for integration with the current team and test planning, Bernardo Taveira for helping with data handling from the test and João Perdigão for assisting in the preparation and development of a plan for aerodynamic testing. I would also like to thank my friends Jaime Pacheco and José Luciano for our time in FST team that culminated in FST10e aerodynamics development, which enabled me to continue further exploring it during this work.

I also wish to thank all my closest friends for their encouragement and for all throughout this academic journey.

Finally, I would like to thank all my family, especially my parents and brother for their continued support and trust throughout all these university years.

Resumo

As forças aerodinâmicas de um carro de competição variam consoante a sua atitude, que por sua vez muda ao longo da pista devido às acelerações a que é sujeito. O principal objectivo deste trabalho é perceber como estas mudanças de atitude influenciam a aerodinâmica do FST10e, o último protótipo construído pela equipa FST Lisboa.

A atitude do carro foi decomposta em 5 parâmetros de interesse: distância ao solo dos eixos dianteiro e traseiro e ângulos de rolamento, direção e guinada, onde o comportamento do veículo é estimado por simulações CFD. O foco principal de CFD foi simular em condições de curva, em que foi estimado o respetivo erro numérico ao realizar um estudo de convergência de malha. A influência de cada um destes parâmetros foi analisada individualmente revelando alguns resultados inesperados, sendo que o ângulo de guinada apresentou com a maior sensibilidade com uma mudança em 16% da força descendente ao longo do seu intervalo. O ângulo de rolamento revelou ter um comportamento monotónico e algo peculiar resultando numa alteração de 9% na força descendente e uma deslocação do centro de pressão de 12%. A distância ao solo apresentou um mudança significativa de 10% em $C_D.A$ e 20% em $-C_L.A$ entre valores máximos em condições simétricas. Um mapa aerodinâmico foi então criado tendo por base mais de 100 pontos de dados contribuindo para uma melhor compreensão sobre a janela de funcionamento. Os resultados podem ser obtidos rapidamente usando um modelo aproximado, que supera o processo moroso de análise CFD. Por fim, uma componente de validação aerodinâmica também foi abordada para estimar os coeficientes de força descendente e de arrasto com testes em pista. O maior desafio encontrado foi estimar a velocidade do ar durante os testes, que se revelou uma grande fonte de incerteza para correlacionar os resultados em pista com CFD.

Palavras-chave: CFD, Formula Student, Mapa aerodinâmico, Validação em pista, Distância ao solo, Atitude de veículo

Abstract

Aerodynamic forces on a race car depend on its attitude, which changes along the track given the accelerations they are subjected to. The main objective of this work is to understand how these attitude changes affect the FST10e aerodynamics, the latest prototype made by FST Lisboa team.

The car's attitude was broken down into five parameters of interest: front and rear ride heights, roll, steering and yaw angles, with the vehicle behaviour being estimated by CFD simulations. The primary focus of CFD was cornering condition simulation, with the corresponding numerical error estimated by performing a mesh convergence. The influence of each of these parameters was evaluated individually, revealing some unexpected results, with the most impactful sensitivity being the yaw angle with a 16% change in downforce across the interval. Roll angle revealed to have a monotonic and rather independent behaviour resulting in 9% change in downforce and a shift of 12% in pressure centre. Ride height presented a significant change with a 10% change in $C_D.A$ and 20% in $-C_L.A$ between peak values in symmetric conditions. An aerodynamic map was then created based on over 100 data points, which provided a thorough understanding across the whole working envelope. The results can be promptly obtained by using a surrogate model, which overcomes the slow CFD analyses. Lastly, an aerodynamic validation component was also addressed to estimate downforce and drag coefficients with on-track testing. The main challenge encountered was to estimate air speed during validation testing, which revealed to be a great source of uncertainty to correlate CFD with track results.

Keywords: CFD, Formula Student, Aerodynamic mapping, On-track validation, Ride height, Vehicle attitude

Contents

List of Tables

List of Figures

Nomenclature

Greek symbols

α	Angle of diffuser expansion.
β	Angle of side-slip.
δ	Angle of steering.
μ	Molecular viscosity coefficient.
Ω	Angular velocity.
ϕ	Angle of roll.
ψ	Angle of yaw.
ρ	Density.
θ	Angle of pitch.

Roman symbols

A	Reference area.
b	Reference length.
C_D	Coefficient of drag.
C_L	Coefficient of lift.
C_M	Coefficient of moment.
C_p	Coefficient of static pressure.
C_{pT}	Coefficient of total pressure.
C_Y	Coefficient of sideforce.
p	Pressure.
q	Dynamic pressure.
V	Velocity magnitude.

Subscripts

∞	Free-stream condition.
I	Inertial component.
i, j, k	Computational indexes.
R	Rotating component.
x, y, z	Cartesian components.
ref	Reference condition.

Superscripts

$\widehat{\ }$	Approximate model.
T	Transpose.

Glossary

ADS	All Possible Data Sets
AHRS	Attitude and Heading Reference System
AMR	Adaptive Mesh Refinement
Aero balance	Aerodynamic Balance
CAD	Computer Aided Design
CFD	Computational Fluid Dynamics.
CFMTFA	Centro de Formação Militar e Técnica da Força Aérea
CG	Centre of Gravity.
CSV	Comma Separated Values
CV	Cross-Validation
DES	Detached Eddy Simulation
DOE	Design of Experiments
DRS	Drag Reduction System
FRH	Front Ride Height.
FSG	Formula Student Germany
FST	Formula Student Técnico Lisboa
FS	Formula Student.
GMSE	Generalization Mean Square Error
IA	Inclination Angle
IC	Instant Centre
ID	Identification
IP	Inflation Pressure
KRG	Kriging Modeling
LES	Large Eddy Simulation
LHS	Latin Hypercube Sampling
LIC	Line Integral Convolution
NS	Navier Stokes
OA	Orthogonal Arrays
PRG	Polynomial Regression Model

RANS	Reynolds-Averaged Navier–Stokes Equations
RCH	Roll Centre Height
RC	Roll Centre
RHS	Right Hand Side
RRH	Rear Ride Height.
SSL	Standard Sea Level
SST	Shear Stress Transport
SS	Split Sample
SoC	State of Charge
TSTP	Test Specification and Test Procedure

Chapter 1

Introduction

1.1 Motivation

The aim of race cars is ultimately to win races and to do so, there are many areas where it is possible to reduce lap times and beat the competitors. One area of expertise that has been on a rise since *1970s* is aerodynamics and a lot of performance can be extracted from it. Aerodynamics plays an important role in the vehicle's stability and handling, helping the driver to achieve consistent and quick lap times.

In contrast to aircraft, negative lift (or downforce) is beneficial for the car's performance on track. For this reason, the same principles of aircraft aerodynamics are used but instead they are turned upside down in order to generate downforce.

As the car is in constant motion due to the accelerations it is subjected to (laterally when cornering and longitudinally when accelerating/braking) vehicle's attitude varies a lot across the track. These changes in the vehicle state directly affect the car aerodynamic performance and the motivation to this work was to understand how the aerodynamic forces and moments acting on a race car vary over a range of attitudes.

The comprehension of this behaviour helps to understand in which conditions aerodynamics package can be refined but is also advantageous for the vehicle dynamics point of view. It provides information to help identify zones of interest to ride the car in and adjust car setup to ride on those conditions, reaching the full potential of the prototype. Lastly, it is also possible to draw conclusions about the stability and "feeling" of the car that can help identify reasons for understeer or oversteer [1].

1.2 Topic Overview

1.2.1 Race Car Aerodynamics

The only components of the vehicle that are in contact with the road are tires, more specifically the contact patch area. All forces experienced by the vehicle are in the end supported by the tires. The

[1] Terms used to describe the sensitivity to steering the car. It undergoes understeer when it does not turn enough as commanded by the driver and oversteer when the car turns more than desired

aerodynamic loads change significantly the forces in them, and they play a very important role in race car performance.

There are three major effects of aerodynamic forces [1] :

- Downforce and its distribution: Aerodynamic vertical force enables an expansion in the tire working envelop, as seen in Fig. 1.1, increasing the size of the polar or G-G diagram [2]. Having this area increase, it affects maximum cornering, braking and traction accelerations. Its distribution between front and rear wheels affects stability due to the grip difference between these wheels.
- Drag: Resistance force has an effect in maximum speed achieved by the vehicle and also plays a part in longitudinal accelerations.
- Side force: Side component of aerodynamic forces point to the corner centre affecting centrifugal force experienced by the vehicle, that is once again related to stability. Also associated with the car handling and control are all moments created such as yaw, roll and pitch (another way to represent downforce distribution).

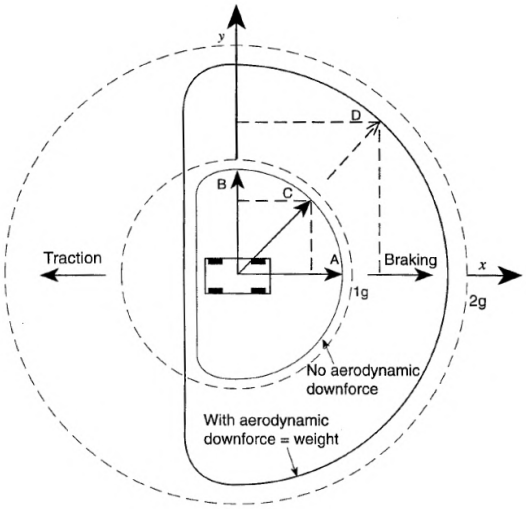

Figure 1.1: Effect of aerodynamic downforce on the polar diagram for a tire maximum performance [2]

Aerodynamic forces are generated from distributed loads in different components across the car. In race cars, particularly in formulas, some typical aerodynamic devices are front and rear wing, sidepods and a floor/diffuser. Figure 1.2 describes the different components of the aerodynamic package of FST10e prototype.

1.2.2 Formula Student

Formula Student (FS) [3] is an engineering competition for university students around the world, that consists of conceiving, designing, fabricating, developing and competing with a small formula style race car. The competition is divided into 3 classes:

[2] G-G diagram is a way to represent the performance envelop of a car where it shows the zone in which the car remains stable with respect to longitudinal and lateral acceleration in G's

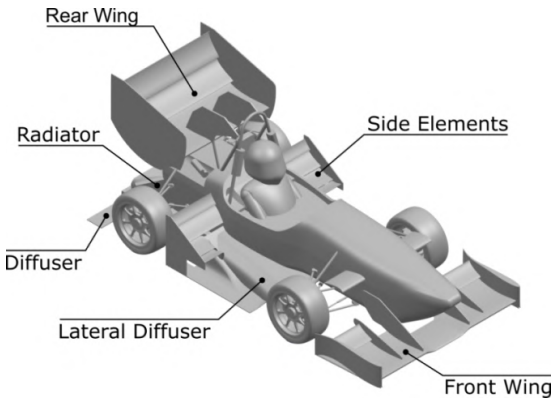

Figure 1.2: FST10e components

- Internal Combustion Engine Vehicle (CV);
- Electric Vehicle (EV);
- Driverless Vehicle (DV), which can be either CV or EV.

Formula Student Técnico Lisboa (FST Lisboa) recently competed with an EV and a DV-EV vehicles following Formula Student Germany (FSG) rules. The EV competition is split into Static and Dynamic Events [4] that include:

- Static Events
  - Business Plan Presentation: develop a business model around the prototype race car to generate profit;
  - Cost and Manufacturing: understanding of manufacturing processes and cost associated with a prototype race car but also the difference to a mass production;
  - Engineering Design: evaluate the engineering process involved in the vehicle design.
- Dynamic Events
  - Skid Pad: Evaluate cornering performance by running in a figure of eight pattern;
  - Acceleration: Straight line acceleration with a length of 75m;
  - Autocross: Achieve the best laptime around a track;
  - Endurance: 22 km around a lap circuit similar to autocross layout;
  - Efficiency: Energy efficiency during endurance event.

This Thesis work fits into 1 static event that is Engineering Design. In this event, a panel of judges evaluate the engineering process and effort made by the students to design the whole vehicle. Regarding aerodynamics, an aerodynamic mapping provides information about the performance in different attitudes. It is important to design an aerodynamic package that works as intended in all working envelope, and integrating aerodynamic mappings into the design process helps in achieving this goal (for example, to prevent a diffuser stalling when the ground clearance reduces and cause an unstable behaviour). With respect to vehicle dynamics design, aerodynamic mappings can play an important role into lap time simulators, as they can be an input for each time step calculation. By updating the aerodynamic behaviour along the track, it enables a better estimate of the car response and with these results, it is possible to evaluate lap time change for multiple designs and even try different car tunings to ride

in the zones of interest. This is yet to be done in FST simulators, but developments are currently being made to implement this tool in the future.

Regarding dynamic events, static ride heights and wings angles/position can be adjusted based on the information provided by aerodynamic mappings as seen in Fig. 1.3 with the rear wing angles adjusted for a low drag configuration for acceleration event.

Figure 1.3: FST10e in FSG 2021 during acceleration event

The FS track layouts follow certain guidelines [5] :

- Straights: No longer than 80 m;
- Constant turns: up to 50 m diameter;
- Hairpin turns: Minimum of 9 m diameter;
- Slaloms: cones in a straight line with 9 m to 15 m spacing;
- Miscellaneous: chicanes, multiple turns, decreasing radius turns, etc.
- Track width: minimum 3 m;
- Length of a lap: around 1 km for endurance and 1.5 km for autocross.

A track layout of a FS competition is displayed in Fig. 1.4 together with velocity and power usage prediction from a point mass simulator by FST's vehicle dynamics department. It is clear that there are only a few sections that the car runs in a straight line or is in constant turning and acceleration. These track characteristics support the idea of studying the vehicle in all attitudes due to being in constant motion.

1.2.3 Aerodynamic Mapping

Aerodynamic mapping is a visual representation of aerodynamic performance for a given set of independent variables (at least two). In motorsport, this tool is used to understand how the car behaves across its working envelope and usually they include front and rear ride height (which represent the distance between the ground to the front and rear axis respectively). An example of a ride height envelope is shown in Fig. 1.5 . At the bottom left corner, we have brake dip that happens when the car pitches forward due to longitudinally deceleration resulting in a decrease of front and increase of rear ride heights.

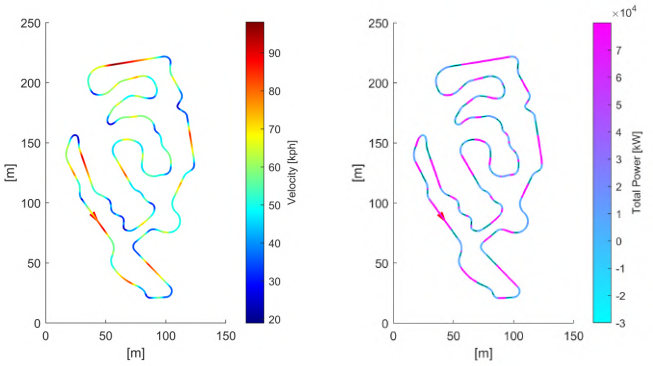

(a) Velocity across a lap (b) Power usage over a lap

Figure 1.4: Formula Student track layout

After this transitory effect, the remaining braking will progressively reduce speed and consequently aerodynamic forces, translating into both front and rear ride heights to increase (suspension springs extend with lower applied forces). When the driver releases the brake pedal and starts throttling at corner entry the opposite occurs, vehicle pitches backwards (front goes up and back goes down in top right corner) and when it gets into to a straight line again, the speed increase compresses the suspension.

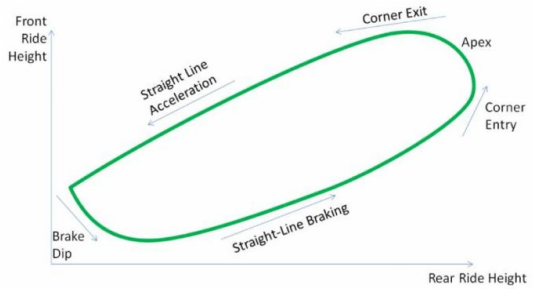

Figure 1.5: Ride height envelope for a formula car [6]

The aerodynamic performance is usually evaluated by at least three dependent variables: lift coefficient, drag coefficient and aerodynamic balance (aero balance). Lift coefficient, defined by

$$C_L = \frac{L}{\frac{1}{2}\rho A {V_\infty}^2}\,, \tag{1.1}$$

is a dimensionless number that indicates the force perpendicular to the incoming airflow. It quantifies the downforce level of the car that change the vertical load tyres are subjected to. Drag coefficient,

$$C_D = \frac{D}{\frac{1}{2}\rho A {V_\infty}^2}\,, \tag{1.2}$$

represents the force in the direction of incoming airflow and it is directly related to the power used to overcome air resistance and longitudinal behaviour. The variables necessary to calculate these coefficients are: lift force L, drag force D, air density ρ, reference area A and freestream air velocity V_∞.

Lastly, aerodynamic balance is a common way to represent pressure centre location in race cars and

it is simply a percentage of how much front axle downforce there is over total downforce expressed by

$$AeroBalance = \frac{Front\ Downforce}{Front\ Downforce + Rear\ Downforce}\,. \tag{1.3}$$

This balance is associated with stability once the magnitude of front wheel downforce can translate into understeer or oversteer.

An example of 2D aerodynamic maps is shown in Fig. 1.6 with C_L and C_D represented on the bottom two images and aero balance is pictured in a different way by using front and rear downforce separately.

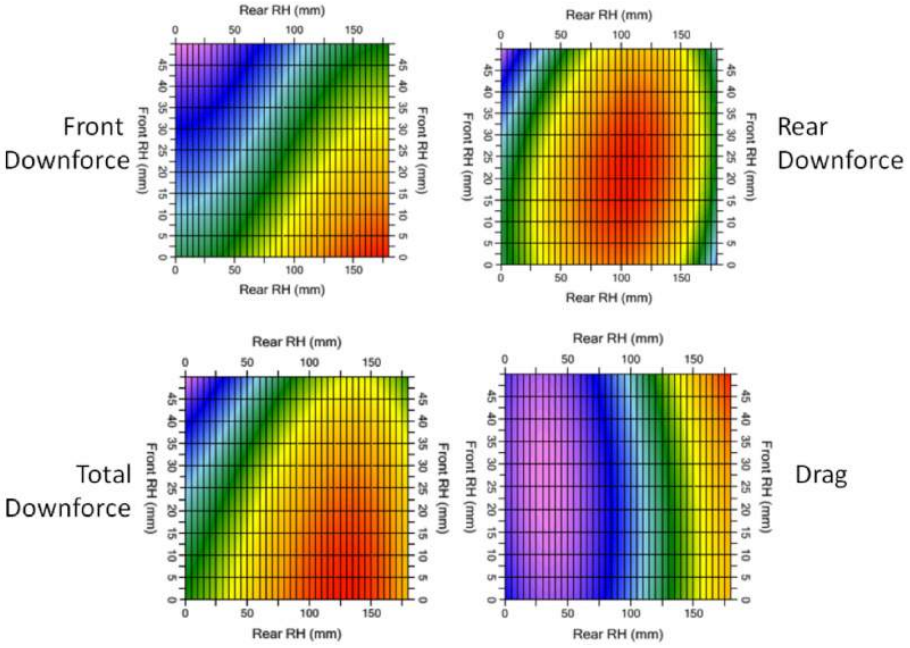

Figure 1.6: Aerodynamic maps for a formula racecar [6]

A more in depth analysis of ground effect aerodynamics of race cars can be found in [7] that display the change in downforce in an open wheel race car with absolute values comparing to wind tunnel test experiments.

Although using two variables can provide plenty of information, for a more thorough analysis the number of independent variables can be increased, which is the case of this work having a total of five that will be described into detail during Section 2.1.3. In Fig. 1.7(a) there is an example of how can an aerodynamic mapping look like when it includes more than two independent variables and, in Fig. 1.7(b), it is also possible to understand how can downforce and drag vary across an entire map.

Usually these complex mappings can be approximated by a surrogate model

1.3 Objectives and Deliverables

The main objective of this work is to create an aerodynamic map of the FST10e prototype, the latest vehicle created by FST that attended competitions in 2021. It is intended to include a maximum of five parameters - front and rear ride heights, roll, steer and yaw angles - and use full car CFD simulations.

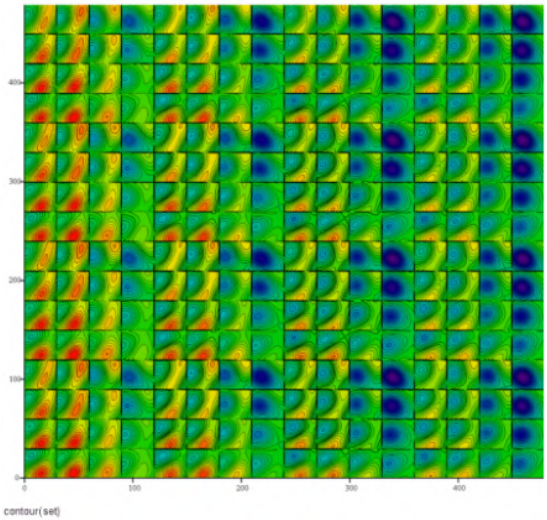

(a) Contour plots showing changes in performance

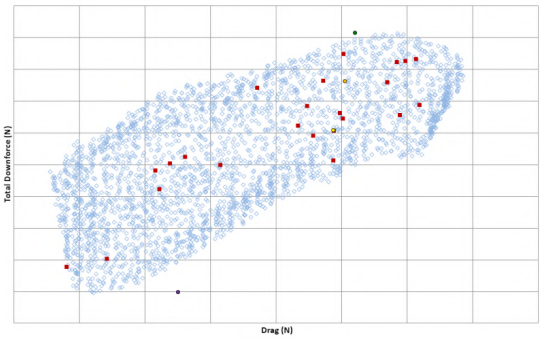

(b) A plot of drag vs. downforce of an entire map

Figure 1.7: Aerodynamic mapping and analysis by *Total Sim* [8]

Another major objective is to do on-track testing and include a validation component. This step would bridge the gap between CFD results and reality, allowing to obtain a comparison between the two. The goal with these track tests is to primarily focus on trends between different setups and not on absolute values correlation due to the uncertainties that cannot be accounted for and also some limited resources to achieve it. Nonetheless, trend evaluation would be a major step towards validation focus which is currently one of the key objectives for FST Lisboa.

In the course of this Thesis, it is expected to present the following deliverables:

- **Parametric CAD:** Making a parametric geometry with respect to the variables in study to speed up the process of making multiple iterations;
- **CFD simulation:** Setup three types of simulations that include cornering, half car symmetrical and full car in straight line giving more emphasis to corner type;
- **Mesh convergence:** Estimate numerical error from a mesh convergence study;
- **CFD process automation:** Develop a macro to fully automate CFD simulations to reduce repetitive work hours and minimize possible human input errors;
- **Aerodynamic map:** Present an aerodynamic mapping with a reduced number of simulations, as they are computationally expensive;
- **Correlation CFD-track results:** Perform on-track testing and compare it to simulation results.

1.4 Thesis Outline

During this Chapter 1, a brief introduction to the work was made. Initially, it was explained the motivation that led to this work and then some background was shown regarding race car aerodynamics, Formula student and aerodynamic maps. At the end of the present Chapter, the objectives and deliverables for this work were set and the outline of this Thesis.

Next, there is Chapter 2 where the mathematical model is described. It starts with the car geometry followed by how corner simulation were modelled and respective numerical error estimation.

In Chapter 3 the remaining type of simulations setup are presented together with the CFD automation workflow.

In Chapter 4 it is assessed the individual impact of each variable of interest with parametric studies.

Chapter 5 focus on the Surrogate Model explaining the approach used to build an approximate model based on CFD results in order to reduce computational cost.

Chapter 6 addresses the on-track validation tests, detailing the testing procedure, data processing gathered from the tests and the results obtained.

Finally, Chapter 7 is the conclusion that states the achievements in this work and also future work that can be done to improve and expand knowledge in this subject.

Chapter 2

Mathematical Modelling

In this Chapter, the models used to obtain a numerical solution for this work will be described from geometric modelling to the corner simulation settings and at the end a numerical error estimation will be addressed.

2.1 Geometric Modelling

2.1.1 Coordinate System

To study the effects of aerodynamics in vehicle dynamics, there is a need to establish a coordinate system. In this case, it was adopted an ISO 8855 coordinate system [9], where x is positive forward, y is positive to the left and z is positive upward like shown in Fig. 2.1. It was used consistently throughout this work to draw conclusions regarding forces and moments.

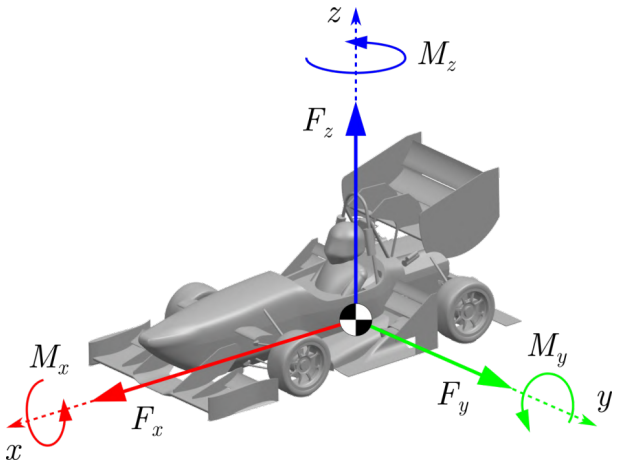

Figure 2.1: Axes systems with origin at CG

Forces are represented by $\mathbf{F} = (F_x, F_y, F_z)$, being F_x in the longitudinal direction (negative mean drag), F_y side force and F_z vertical force (downforce or lift when negative or positive respectively). Using the same idea for moments, $\mathbf{M} = (M_x, M_y, M_z)$ where M_x is rolling moment, M_y pitching moment (positive nose down) and M_z yaw moment (positive turns the car to the left).

When appropriate, all results obtained are represented in dimensionless form. Not only does it help to obtain/compare results at different speeds and air densities (temperatures) but it also eases the process of image visualization. These dimensionless coefficients are also displayed multiplied by the reference dimensions in a way that does not mislead conclusions and forces/moments can be easily obtained when multiplying by the dynamic pressure q. For example $C_L.A$ and $C_{M_y}.A.b$ where A and b are reference area and length respectively.

2.1.2 Geometry

The geometry used for CFD simulations is a simplified CAD model of FST10e and it is derived from the model used for aerodynamic simulations. This CAD is prepared to get a clean and simplified geometry for mesh generation, that include: adding/removing of all details that are not relevant to external aerodynamics (bolts, lids, internal components, etc.), simplification of surfaces to reduce element count where is not necessary (for example, uprights and rims), adding a driver and adjusting features to improve cell quality. This model was made using *Siemens NX®* with the intention to parameterize and speed up the interaction between CAD and CFD.

Suspension

The entire suspension was rebuilt to replicate the car motion depending on suspension geometry. Suspension is moving about its pivot points, even though bellcranks are not physically represented, and updates spring size based on the wheel travel. Regarding suspension parts, rims were further simplified, uprights redesigned including brake discs simplification, it was decided to include suspension brackets [1], it includes steering rack motion and other small adjustments were made to reduce cell count wherever it was found appropriate. Special attention was given to the tires as they deform under load. When tires are under vertical load, the sidewalls bend, lowering the suspension by decreasing tire loaded radius as shown in Fig. 2.2 [10] .

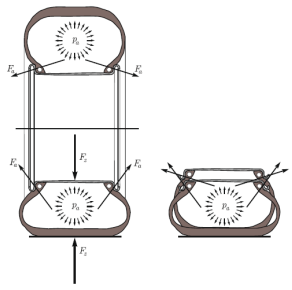

Figure 2.2: How a tire carries a vertical load if properly inflated [10]

Tire shape, particularly closer to the ground, may change the flow structures created and affect its wake. For example, an inconsistency between pressure taps (positioned in the diffuser) and wind tunnel

[1] Because there is an acute angle between monocoque and some suspension arms, there needs to be a feature to ”help” the prism layers to transit from one surface to another. Adding suspension brackets solves this issue (vs removing prism layers in some section as previously) and gives a more accurate geometry to estimate wake downstream of suspension arms to the underbody.

results was found on corner entry, result of the tire sidewall shape being different from one another in the 2012 Red Bull RB8 Formula One car. After improving the tire shape in CFD simulations, it revealed to be a much higher source of low energy air to the diffuser, decreasing downforce as described by *Adrian Newey* [11] . Bearing in mind this effect, some adjustments were made to the tire shape and position to better replicate the tire.

To replicate this motion in CAD, it was implemented a variable called *Loaded radius change* for each tire that lowers the wheel with respect to the ground. It adjusts the coordinate Z of the wheel suspension points and updates tire geometry accordingly (Fig. 2.3(a)). Besides radius change, tire shape was also a little tuned to reproduce bending of side walls. Also in Fig. 2.3(a), it is represented a perfectly round tire in blue colour, while in red includes the adjustment made to the sidewall shape near the ground. Lastly, it is also added a small plinth to each wheel at the contact patch to ensure a good mesh quality. This contact region, creates an acute angle inducing meshing problems and poorly skewed cells. This plinth is an extrusion to this intersected shape (Fig. 2.3(b) and its size can be changed in *Expression* window of CAD geometry (Fig. 2.5(a)) .

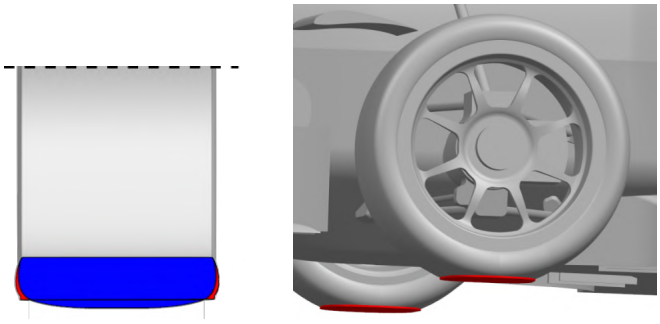

(a) Tire shape change (b) Contact patch plinth

Figure 2.3: Tire in CAD

Aerodynamic package

Regarding the aerodynamic package, trailing edges were thickened to increase the mesh quality of prism layers. It was noticed that prism layers started to decrease in number when reaching the trailing edge due to the airfoil thickness being close to zero at this point and the mesh could not adapt to this angle (shown in Fig. 2.4(a)). To solve this issue, trailing edges in every wing were increased in thickness by one millimetre to assist mesh generation while keeping the same chord. There was a very noticeable difference with this modification, with the final results presented in Fig. 2.4(b).

The wings surfaces were split into trailing edge, lower and upper surfaces allowing specific mesh controls to be implemented for each.

Adjustability

The entire CAD was constructed having in mind parametrization. Besides the five parameters in study described in Sec. 2.1.3, several other features were included to be easily updated: static camber

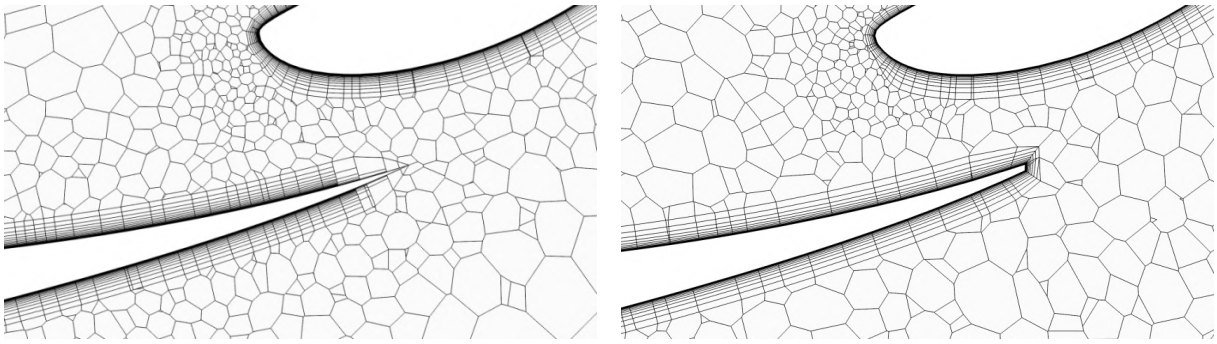

(a) Trailing edge thickness = 0 mm (b) Trailing edge thickness = 1 mm

Figure 2.4: Prism layers

and toe angles for each wheel, loaded radius tire change, contact patch size, front wing height, rear wing flap angles (DRS), suspension point coordinates and roll centre heights. Most of them are shown in Fig. 2.5(a). These features represent adjustments that can be made during car setup (for example adding shims to adjust camber angle) and others to easily update future prototypes if found fit.

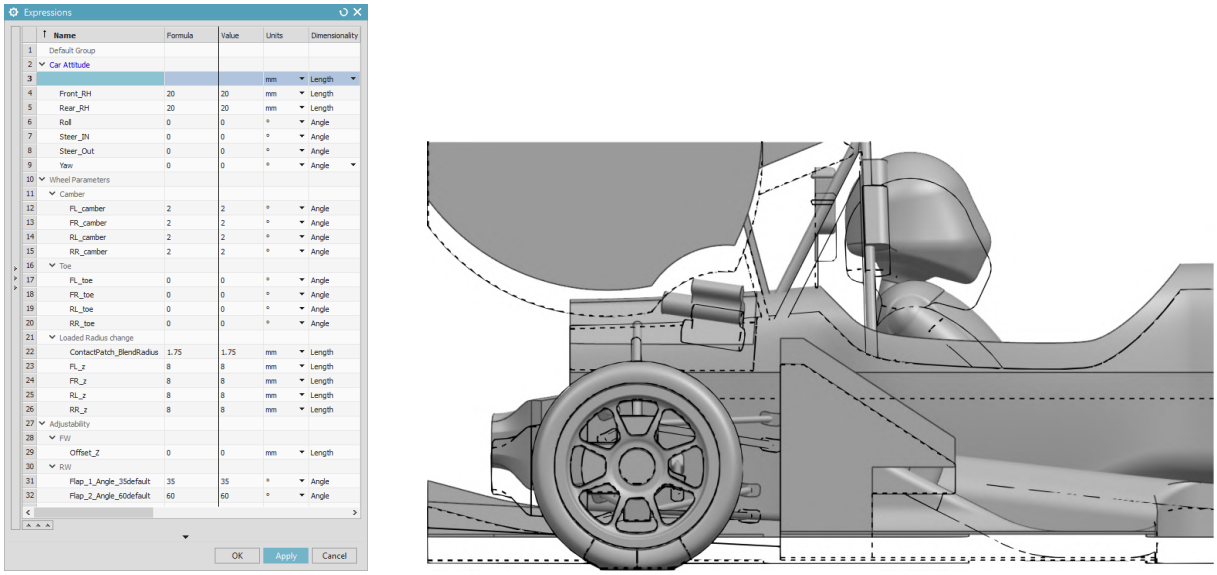

(a) *Siemens NX®* Expressions window to update car geometry

(b) Ride height change from 80mm to 20mm - Note the rear suspension arms motion and difference in spring size

Figure 2.5: Adjustability in CAD geometry

2.1.3 Parameters of Interest

Ride height

As of many race cars, FS prototypes also take advantage of ground effect. For aircraft, this effect reduces wing tip vortices generating less induced drag and also diminishes the upwash, but in race cars as wings are inverted, ground presence will lower the pressure at the suction peak increasing downforce generated. This effect is similar to that obtained for wings and can be explained with the method of images [12]. The FST10e prototype is no exception, using this concept to generate more downforce

with less drag penalty. As ground proximity affects massively the behaviour of the flow around a wing, the distance to the ground (ride height) is a key factor to consider in order to evaluate aerodynamic performance.

Ride height is the distance between the lowest part of the sprung mass body [2] and the ground. The static ride height can be changed by adding shims to the suspension push rod and dynamic ride heights change due to the car motion. Accelerations and differences in speed will vary vertical loads, changing the ride height along the track.

As each axle moves independently, this distance is commonly divided into front ride height (FRH), and rear ride height (RRH) as displayed in Fig. 2.6. Both are measured at the centre of the car ($y = 0$) and they define the vehicle's pitch angle, which directly affects to the angle of attack of all wings,

$$\theta = \arcsin\left(\frac{RRH - FRH}{Wheelbase}\right), \tag{2.1}$$

where wheelbase is the distance between the centres of the front and rear wheels.

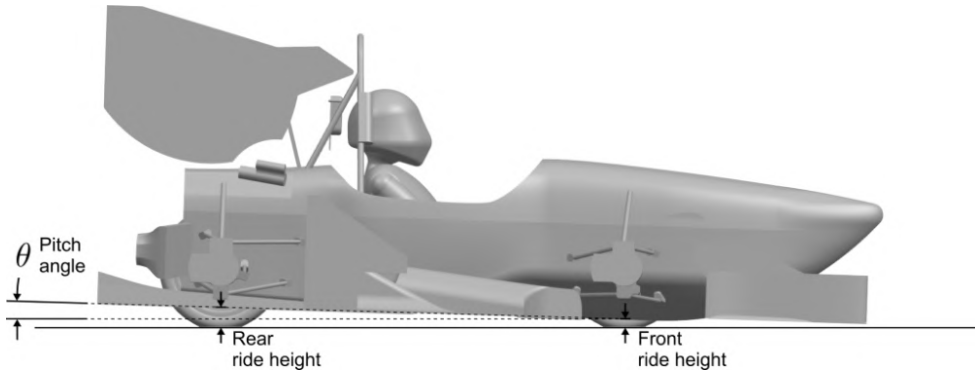

Figure 2.6: Front and rear ride heights

Roll

When a vehicle is cornering, it undergoes lateral acceleration that causes a change in its roll angle (rotation about x-axis). This rotation results in different distances to the ground at each side of the car and, once again, ground effect comes into play but in different ways depending on the side of the car. As pressure fields change from side to side, both side force F_y and rolling moment M_x will be different from zero. To take this behaviour into account, roll angle is included as one of the variables of study shown in Fig. 2.7.

Roll axis is the axis around which the car rotates longitudinally and is determined by the suspension geometry. As suspension geometry differs from front to rear, each has its own roll centre. Roll centre (RC) is an imaginary point that can be found by intersecting the lines connecting the middle of the contact patches to the instant centres. Instant centre (IC) is another projected imaginary point linking the two suspension arms for each wheel. An example of construction of these 2 imaginary points is presented in Fig. 2.8.

[2] In a vehicle, sprung mass includes all the parts that are supported by the suspension.

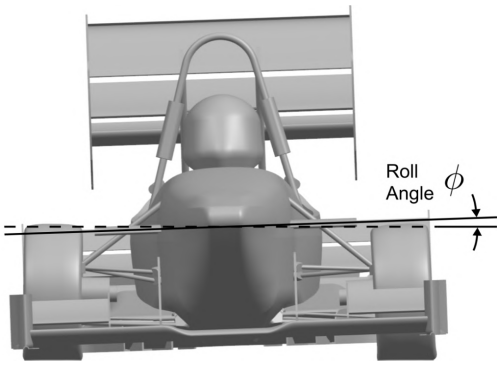

Figure 2.7: Roll angle

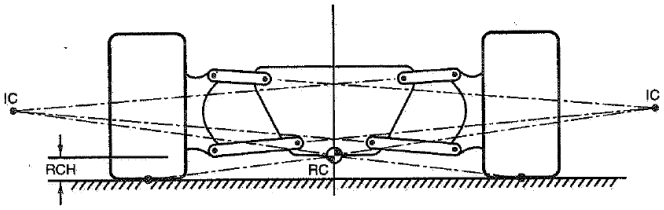

Figure 2.8: Roll centre construction [1]

The roll centre height (RCH) is an important aspect for vehicle dynamics because not only it dictates the axis of rotation but also how much the vehicle rolls due to the existing arm between this point and CG, producing a rolling moment. In fact, because roll centre depends on instant centre it is also an instantaneous point for each suspension geometry. Although the term instant means at the precise moment of time, it was found appropriate to simplify and assume the instant centres to remain fixed, therefore roll centres and roll axis is maintained constant throughout the study.

The rolling axis is obtained by connecting the front and real roll centres, as shown in Fig. 2.9.

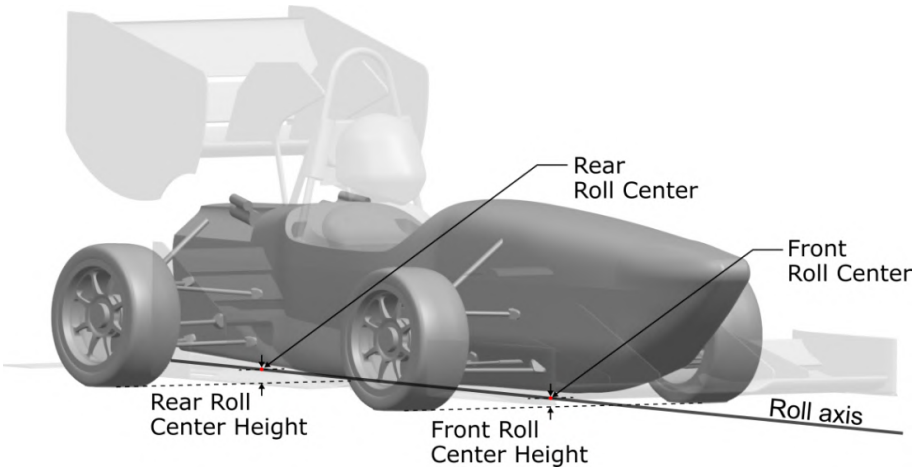

Figure 2.9: Roll axis and roll centres position

Steering

Formula style cars are open-wheeled and uncovered wheels are a major source of flow separation regions and large size wake [3] due to its considerable wake. This low energy air is produced not only by the considerable wheel size and shape but also because of its rotation. There are flow structures created by this phenomena [13] shown in Fig. 2.10, for example the tyre jet [4] is one of the more impactful vortices created for being close to the ground and entering the diffuser area. Although all of these time dependant structures will not be captured in this work it was found appropriate to at least mention the complexity around this region.

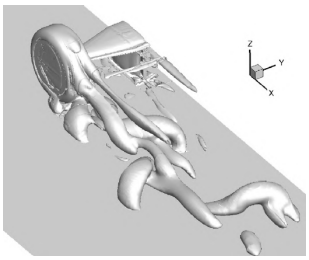

Figure 2.10: Iso-surface of Q criterion exhibiting coherent structures around a tyre wake [13]

The most efficient aerodynamic component of FST10e is the underbody (based on previous CFD during the design process) that is positioned right downstream of the front wheels and it can reveal to be quite sensitive to the wheel wake, which changes in shape, size and orientation based on the steering angle. The steering angle is the angle between the wheel orientation and the longitudinal axis of the car and they are not identical in both sides. Following an Ackermann steering geometry [1], inner wheel steers more than the outer depending on the corner radius and, therefore, they are divided into two: δ_i being inner wheel steering angle and δ_o outer wheel steering angle as represented in Fig. 2.11.

In addition to this, as the car turns differently when steering, the steering angle change is coupled to the cornering radius R. When cornering, in the frame of reference of the car, incoming airflow is no longer straight but rather curved (in circular shape assuming a steady-state condition). As free-stream angle changes depending on position, it means side-slip angle β will also vary throughout the car. For these two reasons - wheel wake and variable free-stream condition - steering angle is chosen as a parameter of interest for this study.

To find each steering angle and its corresponding corner radius, data from a suspension kinematics simulation provided by FST Lisboa vehicle dynamics department was used that consisted in rotating the steering wheel one degree at each step, and then measuring steering angles and calculating the instant turn radius.

[3] This low energy air is commonly called dirty air in motorsport and it is associated with lower total pressure values, opposed to free-stream referred to as clean air

[4] Tyres deform when subjected to loads and in some cases a low energy air region is created at the contact patch (portion of the tyre in contact with the ground)

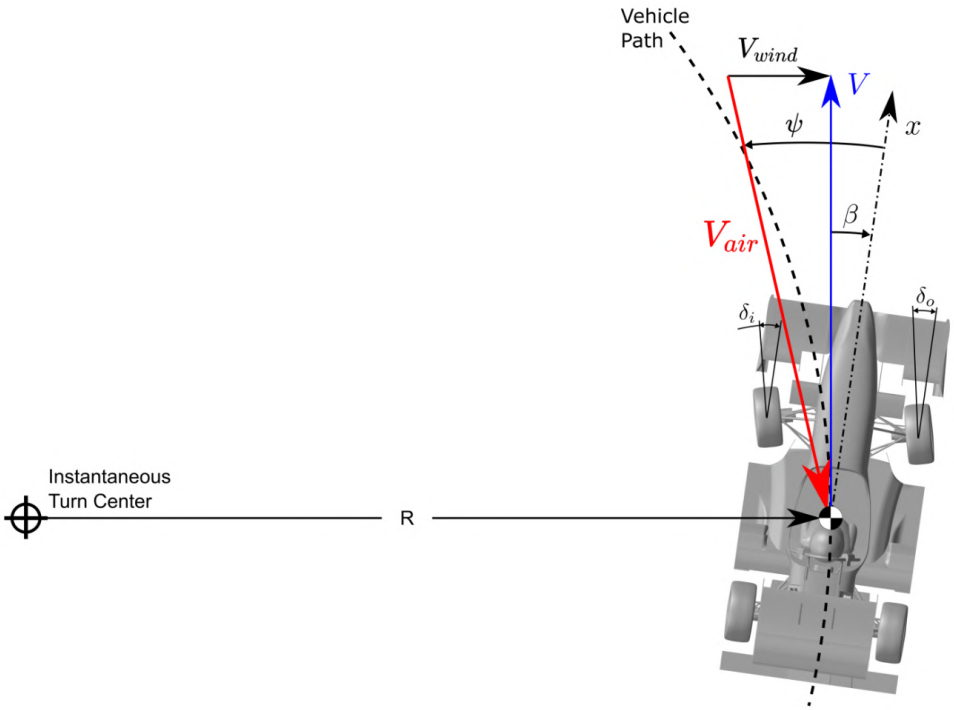

Figure 2.11: Steering and yaw angles in cornering condition

Yaw

There are two factors that change the yaw angle: the side-slip angle and wind influence. Similarly to an aircraft, β is the side-slip angle, measured between vehicle's longitudinal axis and velocity (as represented in Fig. 2.11). This change in direction is caused by the vehicle understeer and oversteer behaviour.

Due to weather conditions, there is a presence of wind, that is related to the incoming airflow direction and magnitude, differentiating car velocity relative to air from car ground velocity. As, once again, this changes the free-stream velocity (magnitude and direction), it was considered relevant for this study and yaw angle is another parameter of interest.

2.2 Cornering Simulation

FS tracks layout is regulated as explained previously in Sec. 1.2.2, having all sort of turns and straights being limited to a maximum of eighty meters. Cornering condition was chosen for a comprehensive analysis and numerical error estimation because it is the most frequent situation of a FS car and to gather more information about this type of simulation that is used less often in FST. There are three main elements of a CFD simulation workflow: pre-processing, solver and post-processing. The first two will be explained in the following sections but the latter will be shown in deeper analysis in Sec. 3.2.

2.2.1 Pre-Processing

Domain

In a steady-state corner, the vehicle is turning with a constant radius. To model this situation in a CFD simulation, it is imposed an angular velocity to the air and in order to align with free-stream orientation the domain takes a shape of a partial hollow cylinder (or a donut sector) illustrated in Fig. 2.12. The dimensions shown in this example were kept constant, resulting in different angles of revolution depending on the corner radius R in study. The domain extends about 3 times the length of the car upstream and 10 times downstream. These values were chosen to minimise the influence of domain walls on the results and are based on previous tests made within FST team.

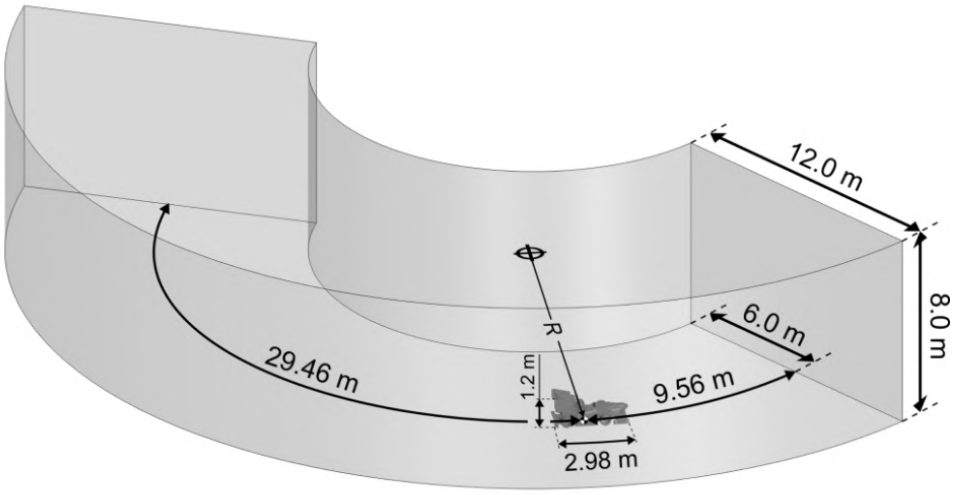

Figure 2.12: Domain dimensions - Example for a 14.9 meter corner radius

Grid generation

In order to perform CFD simulations, it is necessary to get a discretized representation of the geometry in study. To get a good surface quality, the geometry was cleaned up with a feature called *Surface Wrapper*. Using this, it was possible to get a closed surface of the domain of interest (i.e. only the volume between domain walls and the car) with all the gaps closed, non-intersecting surfaces and with better quality due to the surface remesher associated with this feature. It makes sure the base geometry for meshing is water tight, reducing the possibility of errors while generating the mesh. During this step, interfaces are also created between radiator and fluid regions that is going to be further explained later in Sec. 2.2.2.

After geometry clean-up, the next step was to generate the mesh for finite volume solver to be applied. The type of mesh chosen to perform these simulations was the Polyhedral Mesher. In *Star-CCM+®*, polyhedral mesh has been an optimization target, reducing mesh generation time in the latest versions of the software. This type of mesh originates from a tetrahedral mesh, in which the centre of tetrahedral cells are connected, giving rise to a polyhedral type mesh [14].

Polyhedral mesh are made out of polygon faces, increasing the number of surface cells, typically around 14 cell surfaces for each volume cell. This feature increases the number of neighbour cells (Fig. 2.13), allowing gradients to be more accurately calculated as they ”include” more information about the neighbourhood and also reduces numerical diffusion effects due to having more faces in multiple directions [15].

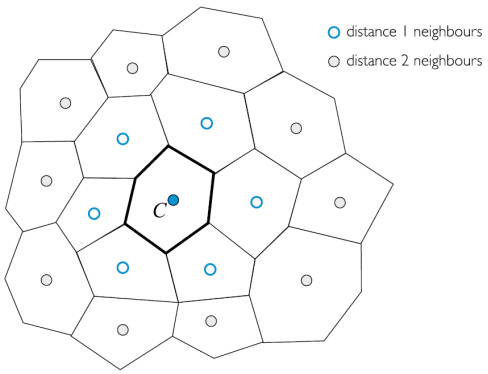

Figure 2.13: A control volume with its immediate neighbours [15]

To refine areas of interest, some boxes were created to efficiently control the cell size. These areas of interest are mainly to capture the car wake, and the developed flow structures (for example flow separation, vortices generation and bursting). Starting with the wake regions shown in Fig. 2.14, three different refinement areas were created:

1. The largest refinement region has a volume control size of around two hundred millimetres, extends to the outlet and aims to capture the disturbed flow from the rear wing. Rear wing wake moves upwards and this refinement area follows its height to the end of the domain.
2. Second largest region of refinement is coloured in blue and has a target volume size of around eighty millimetres. Since the polyhedral mesh elements can increase in size rapidly, this box was a way to smooth the transition from the more refined area to the coarser one.
3. The last of the largest boxes is represented in colour green having a twenty millimetres volume control size. This box has a different shape to adjust to the rear wing wake without adding unnecessary elements upstream of it.

Closer to the car, two more areas of refinement were created with the aim of capturing the wake generated by the front wing and downstream of it, mainly around the lateral diffuser:

4. Coloured in cyan blue in Fig. 2.15 and targeting around six millimetres, this box was created to better resolve flow structures generated by the front wing. Vortices created in this area affect downstream elements significantly but a grid to fully resolve them and avoid its diffusion is not affordable.
5. The last box created for refinement was targeted for seven millimetres around the lateral diffuser area. As this component is quite complex, it also generates vortices to create low pressure areas and so, this box helps capturing all these structures.

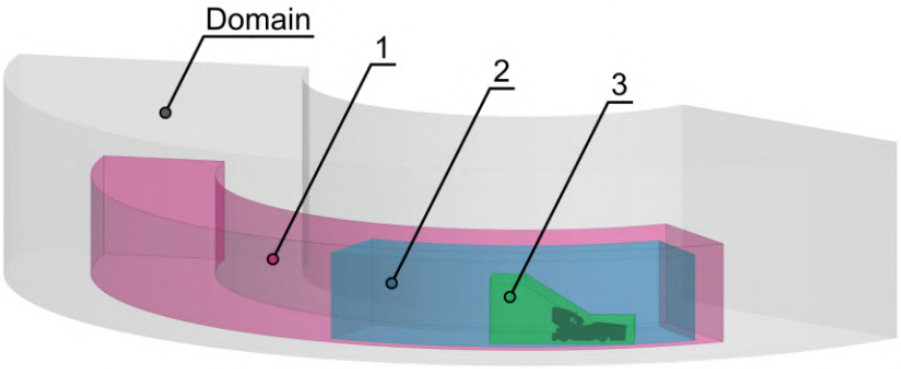

Figure 2.14: Refinement boxes - In farfield region

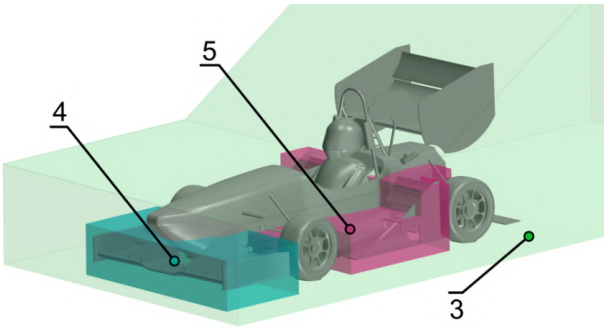

Figure 2.15: Refinement boxes - In near wake region

At the wing trailing edges, reducing minimum size keeps its shape and allows prism layers to transition from top to bottom. A finer control was associated with the upper surface compared to the lower one, to focus on the steeper adverse pressure gradients present in this surface without adding unnecessary cells to the lower surface that can capture smoother favourable pressure gradients with fewer cells.

Mesh settings varied quite a lot throughout the components of the car. Twenty two custom controls (excluding the five explained above) were created to regulate target and minimum sizes, surface curvature refinement for leading edges, number of prism layers and respective height, and to disable prism layers for some components. This customization was performed to decrease the computational cost of each simulation keeping the numerical uncertainty at acceptable levels. This is the main advantage of unstructured flow solvers and in particular of those that accept cells of arbitrary shape. In Fig. 2.16 it is possible to see the volume mesh, and the different surface controls with different colours.

2.2.2 Solver

To model the physical phenomena involved in these simulations, mathematical models, boundary conditions, material properties, numerical solution techniques and discretization schemes have to be chosen that fit into the type of study. The options used in the CFD simulations in this work were:

1. Mathematical Models

   - Reynolds-averaged Navier–Stokes(RANS) equations using the $k-\omega$ **SST two-equation, eddy-viscosity turbulence model** [16]: Explained during this Section;

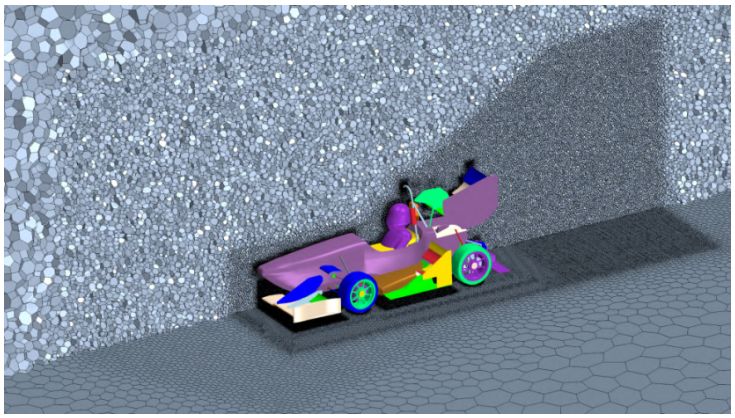

Figure 2.16: Volume mesh and different named surfaces

- **Steady:** Time-averaging is applied to define the mean flow and so the flow is three-dimensional but steady;
- **Turbulent:** Fully turbulent free-stream was chosen and this topic will be approached in Sec. 2.2.2 to check if there was a need to include laminar flow;

2. Boundary conditions

   - **All y+ Wall Treatment and Wall Distance:** Shear-stress at the wall can be determined form the definition or wall functions. More details are described in the following Wall Modelling Section;

3. Material properties

   - **Air SSL:** Incompressible fluid with density equal to $\rho = 1.225\ kg/m^3$ and a dynamic viscosity of $\mu = 1.8.10^{-5}\ Pa.s$;

4. Solution techniques

   - **Segregated Flow:** Using this model, solver resolves the conservation equations of mass and momentum sequentially, as opposed to coupled flow that solves them simultaneously and converges faster;

5. Discretization techniques

   - **Gradients:** Use of gradients and limiter methods (Venkatakrishnan limiter [17]);
   - **Cell Quality Remediation:** Just as a precaution, this model was implemented to improve the robustness of the solution by modifying gradients in highly skewed cells;

Turbulence Models

First of all, an approach using RANS was the starting point. In a practical point of view, this is the only approach that allows to perform simulations in a reasonable amount of time and it fits the flow characteristics due to large region of separated flow and other strong viscous effects, having a low Reynolds number ($\mathcal{O}(10^6)$) and approximately steady-state behaviour.

To obtain the RANS equations, it is used a Reynolds decomposition in Navier-Stokes (NS) equations, that separates the flow variable into a mean and fluctuation,

$$\phi = \bar{\phi} + \phi' \,, \tag{2.2}$$

where ϕ represents an instantaneous value (in this case for velocity components and pressure), $\bar{\phi}$ the time averaged value, ϕ' the flutuation around the mean value, and then an averaging of the equations themselves.

Assuming a steady-state, incompressible fluid with no external forces applied, the RANS equations can be stated as

$$\rho \bar{u}_j \frac{\partial \bar{u}_i}{\partial x_j} = \frac{\partial}{\partial x_j} \left[-\bar{p}\delta_{ij} + \mu \left(\frac{\partial \bar{u}_i}{\partial x_j} + \frac{\partial \bar{u}_j}{\partial x_i} \right) - \underbrace{\rho \overline{u_i' u_j'}}_{\text{Reynolds Stress}} \right]. \tag{2.3}$$

Although the equations went under an averaging process, it results in a term called Reynolds Stress last term in RHS of Eq. (2.3) that includes averaged fluctuating velocity components. As fluctuations are not directly calculated, this term has to be modelled using a turbulence model to get a closure of the system of equations [18]. The turbulence model chosen was the $\boldsymbol{k-\omega}$ SST, that is known for its ability to handle adverse pressure-gradient flows when compared to other eddy viscosity models [16]. These characteristics are suitable to external aerodynamics applications, in order to have a better separation prediction.

The $\boldsymbol{k-\omega}$ is a SST eddy-viscosity model with two modelled transport equations. One equation for turbulent kinetic energy $\boldsymbol{k}$ and another for the specific dissipation rate $\boldsymbol{\omega}$. SST stands for Shear Stress Transport, and it is responsible mitigate problems related to sensitivity of this model to free-stream turbulence properties. It accomplishes this by changing to a $\boldsymbol{k-\epsilon}$ [5] model in the free-stream while resolving near wall with the $\boldsymbol{k-\omega}$ formulation.

Reference Frame

In the car's frame of reference, while driving steadily in a constant radius turn, both air and ground travels in a rotating motion. To mimic this effect, the whole domain was set into a rotating motion by adding a rotating reference frame. This technique is commonly used in turbomachinery applications, which enables the possibility of simulating constant motion of components with a steady-state model without moving the mesh (stationary mesh). In this work, a reference frame is applied to the whole region of study to simulate corner condition but it has other applications in car simulations such as to model the rotating air between the rim spokes.

By adding this rotating frame, Navier-Stokes equations will be changed. The inertial velocity vector $\vec{u}_I$ is defined by

$$\vec{u}_I = \vec{u}_R + \vec{\Omega} \times \vec{r}, \tag{2.4}$$

[5] $\boldsymbol{\omega = \epsilon/k}$ - relation between $\boldsymbol{\omega}$ and turbulent dissipation rate $\boldsymbol{\epsilon}$

where: $\vec{u}$ - velocity vector; I - Inertial notation; R - Rotating notation; $\vec{\Omega}$ - Rotation vector; $\vec{r}$ - distance vector from the cell to axis of rotation.

By applying this transformation to the incompressible, steady Navier-Stokes equations, in the rotating frame and in terms of relative velocity (new unknown instead of absolute velocity) [19], yields

$$\nabla \cdot (\vec{u}_R \otimes \vec{u}_R) + \underbrace{2\Omega \times \vec{u}_R}_{\text{Coriolis}} + \underbrace{\Omega \times \Omega \times \vec{r}}_{\text{Centrifugal}} = -\nabla(p/\rho) + \nu \nabla \cdot \nabla (\vec{u}_R) \ . \tag{2.5}$$

In addition to the convective, diffusion and pressure gradient terms from the original RANS equation (Eq. 2.3), this transformation gives rise to two additional source terms: centrifugal and coriolis forces (noted in Eq. 2.5). These terms are related to the inertial accelerations objects are subjected when rotating. By adding these two source terms to every cell present in the region of study, a rotating domain is simulated. The angular velocity of the domain varies depending on the corner radius in order to keep the car tangential velocity and respective Reynolds number as constant as possible.

Wall Modelling

A good resolution of the near-wall region is essential to predict flow separation and boundary layer growth over the car. The inner region of the boundary layer consists of three sub-layers that are represented in Fig. 2.17(a) where u^+ is non-dimensional velocity and y^+ is a non-dimensional distance from the wall to the first mesh node.

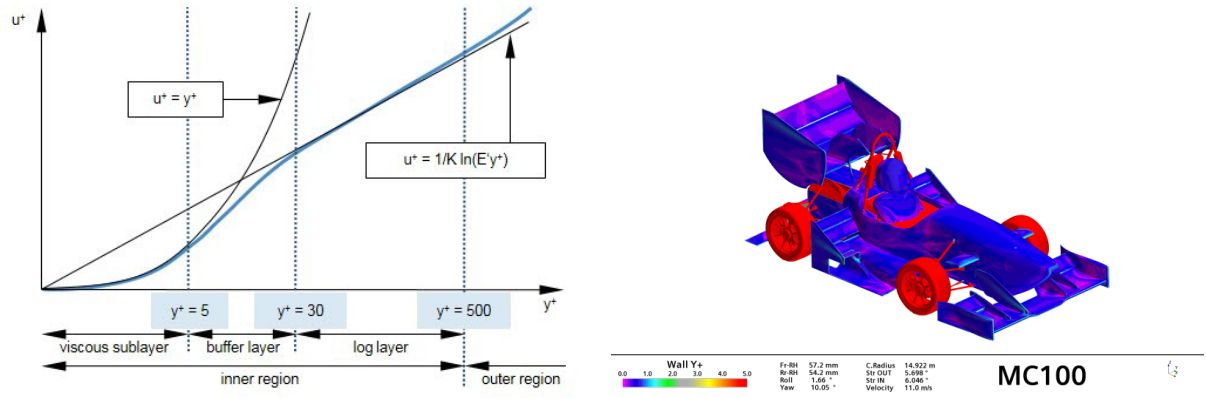

(a) Sublayers and regions of a boundary layer [20]

(b) Wall y^+

Figure 2.17: Boundary layer sublayers and simulation wall y^+

To capture all these sub layers accurately, prism layer meshing was included in relevant surfaces of the car. As these type of cells increase substantially the cell count, the prism layer heights and the number of layers were modified accordingly to the boundary layer growth. Target y+ (Fig. 2.17(b)) value for these surfaces was around one, to be positioned inside viscous sublayer.

In some locations, it was found appropriate to disable the prism layers (coloured red in Fig. 2.17(b)) and use the traditional wall function approach, which approximates the boundary layer as shown in Fig. 2.18(b). This is called a high-y^+ treatment and allows an important reduction in near-wall cells. This

wall function approach was only used in suspension parts, wheels, main hoop [6] that either have sharp corners or separation zones should not vary significantly.

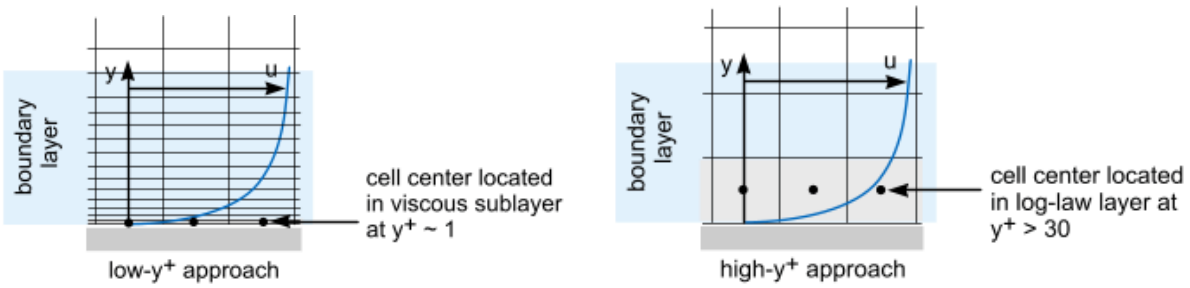

(a) Low y^+ approach- shear-stress calculated from the definition

(b) High y^+ approach - shear-stress calculated from the log-law

Figure 2.18: Wall treatment [20]

The remaining surfaces of the car (aerodynamic package, monocoque and driver) had a more accurate prediction of the boundary layer using a low-y^+ treatment (Fig. 2.18(a)) using a finer mesh. Because both high and low y^+ were used, an All y^+ treatment was chosen to model the walls.

Transition Model

Boundary layer transition is the phenomenon of laminar flow turning into turbulent. Transition affects boundary layer growth but also pressure fields due to laminar separation bubbles and reattachment that can occur for the typical Reynolds number of the wings of a FS car. To evaluate the need of integrating a transition model into the simulations, two simulations were compared, with and without a transition model.

The model chosen was the Gamma transition model. This model is a one-equation model [21] that adds a production term for the intermittency (zero for laminar flow and one for turbulent flow) [22].

Table 2.1: Transition Model study

	Computational Time [h]	Forces			Moments		
		$C_D.A$	$C_Y.A$	$C_L.A$	$C_{Mx}.A.b$	$C_{My}.A.b$	$C_{Mz}.A.b$
No Transition Model	14.6	1.575	-0.050	-3.309	0.033	-0.138	-0.344
Transition Model	16.7	1.561	-0.066	-3.330	0.029	-0.099	-0.354

It was observed that using the transition model added around two hours of computational time, while forces, moments and the residuals did not show any significant change. A further analysis was made to find the differences in the pressure field between both models. A static pressure coefficient delta between both simulations is displayed in Fig. 2.19 that led to the conclusion that the biggest change is mostly underneath the front wing, where it appears to have a laminar separation bubble followed by reattachment leading to a reduction in pressure.

With these results, it was found the best option not to use the transition model as it increased computational cost without a significant change in the relevant variables - integrated forces and moments

[6] A roll bar located alongside or just behind the driver's torso to protect the driver during roll over.

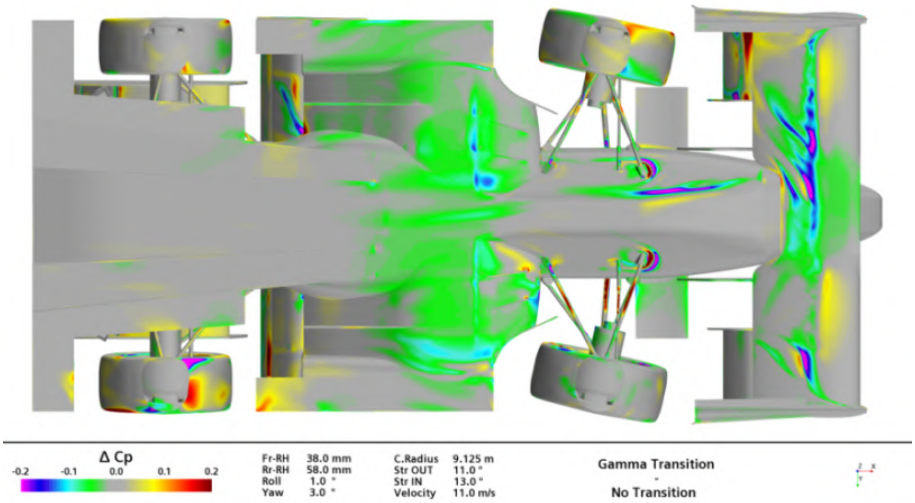

Figure 2.19: Delta pressure coefficient to study the effect of transition

over the vehicle.

Cooling

In this section, it will be explained how the radiators and fans were modelled. As radiators increase static pressure upstream and fans impose a pressure rise, these cooling parts were integrated into the model, as they influence external aerodynamics. These components are positioned at the rear of the car, as shown in Fig. 1.2.

To simulate the radiators, it was used the feature of Porous Region in *Star-CCM+®*. By setting a porous viscous and inertial resistance, a radiator can be modelled by restricting the air into a specific direction and imposing a pressure drop depending on the incoming airflow. By imposing these constants, it allows to replicate the influence of a radiator without using a complex shape including all the fins, reducing massively the cell count. To estimate these porous parameters, the fin geometry was simulated at different velocities and by fitting a parabolic regression to the pressure drop versus velocity (work done in FST) it is possible to obtain the constants [23]:

- Porous inertial resistance: $57.0\ kg/m^4$
- Porous viscous resistance: $592.0\ kg/m^3s$

The fan positioned downstream of the radiator is modelled as a fan interface which imposes a pressure rise depending on the local flow rate. This data is commonly displayed in the fan product datasheet, and the data points from P-Q curve (Fig. 2.20) were introduced to simulate the respective pressure rise for incoming air flow rate. During geometry repairing, it is also added a coordinate system in the middle point of the fan to use as a centre of rotation for swirl.

Boundary conditions

The boundary and initial conditions used to model a steady-state cornering car were the following:

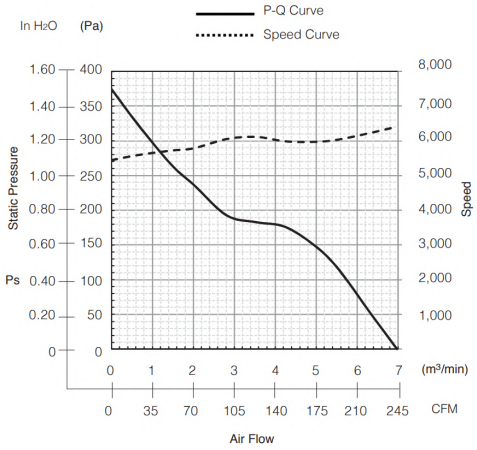

Figure 2.20: Fan curve (taken from NMB 12038 VA datasheet)

- **Whole Domain:** the entire region is set in motion with a rotating reference frame to simulate steady-state cornering has explained previously;
- **Inlet:** A velocity inlet boundary condition is used to define free-stream condition. In this case it is specified as $V = 0\ m/s$ with respect to the inertial frame so that the inlet has a constant angular velocity visible in Fig. 2.21;
- **Car:** All surfaces of the car are no-slip walls in order to induce $V_{wall} = 0\ m/s$ to take into account the real viscous flow behaviour, leading to a development of boundary layer;
- **Wheels:** The wheels have a wall rotation boundary condition. Each wheel has its own coordinate system based on the wheel centre position to set the correct axis of rotation. The angular velocity of each wheel is based on the wheel centre height, distance to the turning centre and steering angle;
- **Ground:** The lower surface representing the ground is also a no-slip wall but this time is has a velocity associated to simulate the moving ground. This velocity is the same as the inlet having a constant angular velocity;
- **Outlet:** A pressure outlet boundary was used with a constant relative pressure of $0\ Pa$ to represent the outflow condition. The value chosen is zero because it is relative to the atmospheric pressure;
- **Walls:** The remaining walls of the computational domain ceiling, inner and outer wall in which the last 2 are hidden in Fig. 2.21 are modelled as slip walls. This results in the shear stress being zero on these walls, to not develop unrealistic boundary layers;

2.3 Adaptive Mesh Refinement

In an attempt to reduce simulation time by allocating better the mesh refinements, it was used an Adaptive Mesh Refinement (AMR) strategy instead of the boxes displayed in Section 2.2.1. Adaptive Mesh Refinement is a method to adjust mesh size (refine or coarsen) based on a chosen criterion from the solution. This means the refinement occurs during the simulation, updating the mesh depending on the current solution. The criterion depends on the type of simulation and the flow characteristics that are

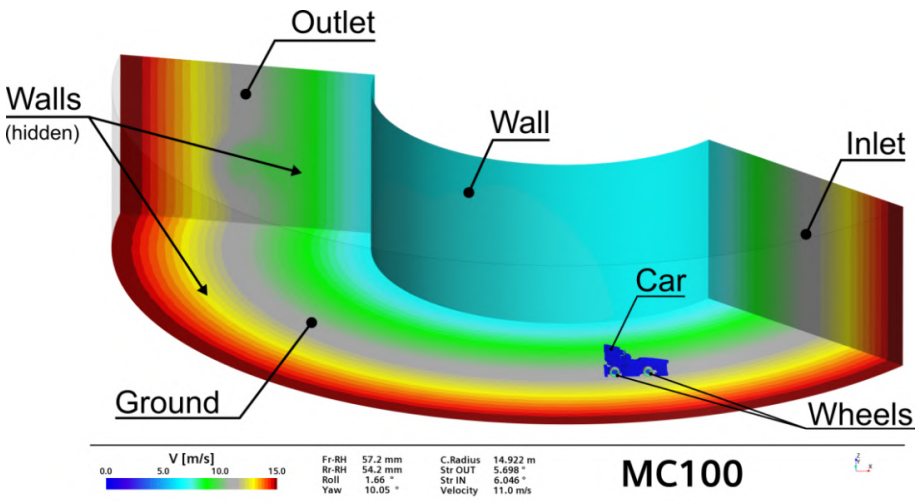

Figure 2.21: Boundary conditions - corner condition

meant to be better captured in the solution. In this case, the chosen mesh refinement criterion for each volume cell is

$$S(r,\theta,z) = \mid \nabla \cdot \nabla \underbrace{\left(\frac{p_t - p_{ref}}{\frac{1}{2}\rho(\omega r)^2} \right)}_{C_{p_T}} \mid \times (AdaptionCellSize)^2, \tag{2.6}$$

where p_t is total pressure, p_{ref} is reference pressure, ω is the angular velocity of simulation, r is the cell centroid radius (distance to rotation axis), C_{p_T} is total pressure coefficient and $AdaptionCellSize$ is the cell size in volume mesh that is two times the maximum distance between cell centroid and any of the cell vertices [24].

In this study, the objective was to focus cell allocation to high values of the Laplacian of total pressure coefficient. It was opted to use the divergence of a gradient instead of a gradient alone to prevent cells to be allocated in areas with constant/high gradient values that can be easily modelled with a fewer number of cells, especially with polyhedral type cells. This Laplacian value is then multiplied by the cell size by recommendation of the software user-guide [24] to get an influence on the current size, to focus on the bigger cells than needed instead of infinitely refining small cells. The power of two related to this cell size was tweaked to find a good ratio between the Laplacian value and cell size.

The total pressure coefficient is calculated with a different dynamic pressure because the freestream velocity is not constant throughout the domain. The better way found to fix this problem was to express linear velocity as a function of angular velocity and corresponding radius with: $V = \omega r$. Using this, it was possible to achieve a total pressure coefficient of one in all free-stream. This dynamic pressure adjustment was also used for post-processing plots.

After some experiments, the values found to better suit the case to refine the mesh are

$$\text{Adaptive behavior} \begin{cases} \text{refine} & \text{if } S > 1.5 \\ \text{keep} & \text{if } 0.025 \leq S \leq 1.5 \\ \text{coarsen} & \text{if } S < 0.025 \end{cases} \cdot \tag{2.7}$$

Moreover, it was specified a minimum adaption cell size of five millimetres, not to be applicable to prism layers and an iteration frequency of one hundred - every one hundred iterations the solver runs, an update is made to the mesh based on the criterion mentioned above.

A maximum refinement level of two was also set to limit the number of subdivisions of a cell. In a polyhedral cell, subdivision can go up to 12-15 cells due to the high number of vertices as visible in Fig. 2.22.

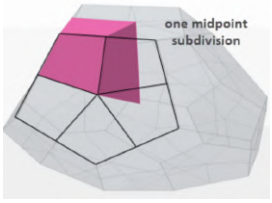

Figure 2.22: Polyhedral cell subdivision [24]

After this setup, it was compared a simulation corresponding to a high-speed corner attitude with AMR and the traditional refinement boxes where the results are shown in Tab. 2.2. The differences between the two results are not drastic, being the pitch moment C_{M_y} the most significant change. It was also possible to note that although the final mesh ended with a fewer number of cells, the total computational time was increased due to the additional calculations and mesh division during this time. As the time to generate the initial mesh was smaller, it took roughly the same total time.

Table 2.2: Adaptive Mesh Results

	Setup		Results					
			Forces			Moments		
	Comp. time [h]	Cells [Million]	$C_D.A$	$C_Y.A$	$C_L.A$	$C_{M_x}.A.b$	$C_{M_y}.A.b$	$C_{M_z}.A.b$
Standard mesh	15.2	14.0	1.624	0.083	-3.364	0.085	-0.196	-0.179
Adaptive mesh	15.4	12.1	1.566	0.089	-3.397	0.060	-0.097	-0.149
Δ	0.2	-1.9	-0.058	0.006	-0.033	-0.025	-0.099	0.03

In Fig. 2.23 it is presented a plane section view at a coordinate $X = 475mm$ (intersecting the front wing), displaying the total pressure coefficient and respective mesh. It is visible that the AMR approach (Fig. 2.23(b)) refines cells to better capture the vortices structures, while in Fig. 2.23(a) the whole area around the front wing is refined but only slightly, meaning that there a possibility some areas may not be so well represented.

This same approach was then tried in a low-speed corner attitude, but it was not successful. Mesh size increased drastically and fully converged simulation could not be achieved even when tweaking the constants. As this criterion seemed too sensitive to the corner radius, it was found the best option to

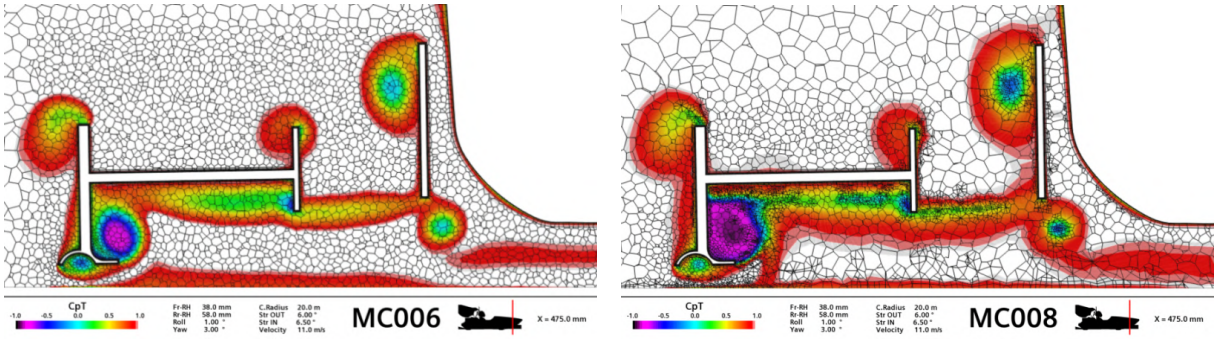

(a) Refinement boxes

(b) Adaptive mesh

Figure 2.23: Comparison of the effect of mesh refinement in the total pressure coefficient at x = 475 mm

discard AMR and continue with the traditional refinement approach for the remaining simulations.

2.4 Numerical Error

In this section, numerical error derived from the models used to solve this problem will be broken down into four distinct parts that will be estimated, to draw more founded conclusions when analysing the results [25]: round-off error, discretization error, statistical sampling error and iterative error.

As these equations do not have an analytical solution, there is no possibility to estimate numerical error by

$$\epsilon_\phi = \phi_i - \phi_0 \,, \tag{2.8}$$

where ϵ_ϕ is the error of a variable, ϕ_i is the approximate solution and ϕ_0 the exact solution.

2.4.1 Round-Off Error

As computers have a finite precision, there is a possibility that the round-off error is significant but to determine it exactly, infinite precision would be needed. To reduce this error, it was used a double precision version of the software, i.e. 8 bytes of memory and has 14 digits of precision. Having this number of digits, this source of error can be negligible when compared to the others.

2.4.2 Statistical Sampling Error

Statistical error is usually linked to unsteady simulations. Even though this work is based in a steady state assumption, oscillations of the results occur if there is a physical unsteadiness. In this case, vortex shedding phenomenon is responsible for an oscillation in forces and moments. As expected, this physical instability occurs most predominantly at the rear of the car, where vortices are being released from the rear wing and diffuser. It was noticeable that, after a number of iterations, the results would oscillate around a steady value periodically.

Standard deviation for the last 500 iterations of mesh convergence analysis is presented in Fig. 2.24 to exhibit the oscillation of around four Newtons in downforce caused by vortex shedding in the whole car. Contrastingly, the standard error (or standard deviation of the mean) is negligible, that is hardly visible in black. Simply averaging everything for a number of iterations allowed to reduce substantially statistical sampling error.

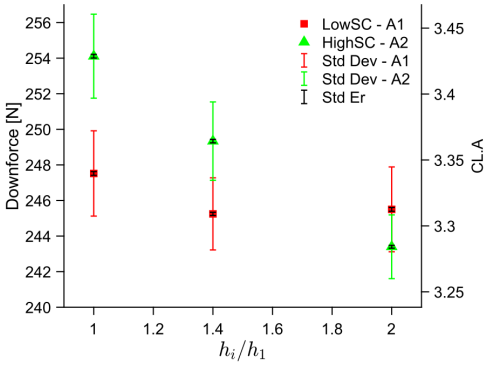

Figure 2.24: Downforce standard deviation and error for the last 500 iterations

Initially, during mesh convergence study, 1700 iterations were ran and results averaged for the last 500. It was found that 1700 iterations were excessive, because the convergence was achieved much sooner and then just oscillated around a steady value. For the remaining simulations, a total of 1000 iterations were ran, averaging all results for the last 250 iterations.

In addition to calculating the mean forces and moments, the same approach was used for field functions, responsible for post-processing images. By comparing images from different simulations, results could be misleading if comparing images in different phases of a vortex shedding cycle. A direct side by side comparison is displayed in Fig. 2.25 with coloured total pressure coefficient and field lines based on velocity vector using line integral convolution (LIC) [7]. While in the last iteration image some vortices are visible downstream of the rear wing, they are no longer visible to the right presenting a smoother field result of the averaging process.

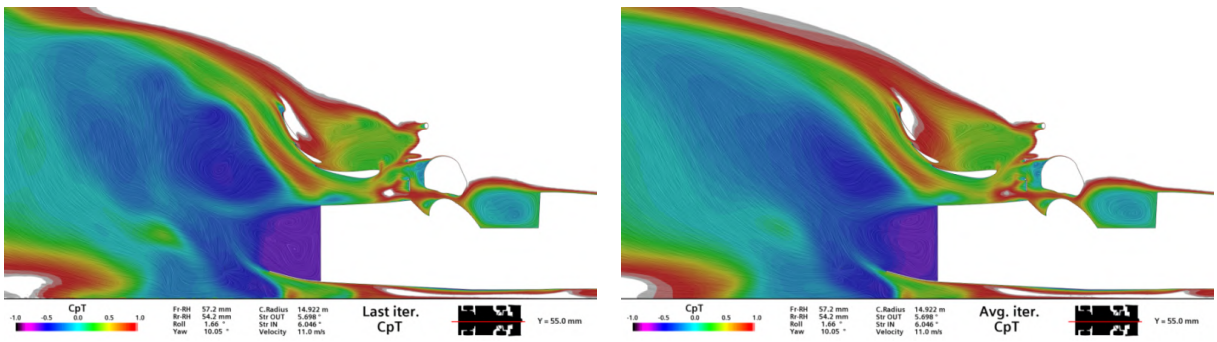

(a) Last iteration value

(b) Averaged 250 iteration

Figure 2.25: Comparison of the effect of averaging in the total pressure coefficient

[7] LIC is a technique used to image vector fields [26]

2.4.3 Iterative Error

An iterative method has to be used to resolve non-linear equations, inducing an error between the exact and the approximate solution. Segregated solvers may increase this error as they solve equations consecutively, but in this case a high number of iterations was ran in an attempt to minimize this contribution. Using a coupled solver was not an option due to excessive RAM needed to resolve the equations simultaneously. To monitor this error, it was also given attention to the residuals and variables of interest convergence [27].

2.4.4 Discretization Error

The discretization error is typically the greatest source of error and it derives from the fact that continuous functions are split into a finite number of volume elements to solve a set of governing partial differential equations. Assuming this type of error to have a predominant effect over the others (which is usually the case [27]), the numerical error can be estimated and assumed to be the same as discretization error. A special attention was given to get a tangible value for the discretization error and get a clear picture of what can be concluded. The remaining sources of error were seeked to be as small as possible as will be shown next in this Section.

The discretization error can be estimated based on a mesh convergence study where results are obtained for different values of mesh spacing parameter, h. This study was performed in a low speed corner attitude (A1 - Attitude 1 / Skidpad) and then repeated for an attitude where only 1 parameter was changed, visible in Tab. 2.3. In this case, the steering angle was changed and consequently cornering radius, to represent a high-speed corner (A2 - Attitude 2) . This change allows to understand the trends when varying a parameter in study.

Table 2.3: Simulation attitudes

	Fr-RH [mm]	Rr-RH [mm]	Yaw [º]	Roll [º]	Steer in [º]	Steer out [º]	Turn Radii [m]	Velocity [m/s]
Low-speed corner - A1	38.0	58.0	3.0	1.0	13.0	11.0	9.125	11.0
High-speed corner - A2	38.0	58.0	3.0	1.0	6.5	6.0	20.0	11.0

The approach used to estimate the error was based on a power series expansion (following the procedure in [28]). Using a typical cell size h_i, convergence order p and constant α, the discretization error ϵ_ϕ can be estimated as

$$\epsilon_\phi = \alpha {h_i}^p \,. \tag{2.9}$$

To obtain grid convergence, it is important that the grids are geometrically similar, meaning the refinement should be approximately constant in all domain. To accomplish this in the best possible way, a parameter was included in all relevant mesh controls (for example surface, volume sizes and prism layers) to be easily changed and get the most similar refinement possible while using unstructured type meshes.

Typical mesh size was varied in three distant intervals for each of the attitudes, obtaining the results present in Tab. 2.4.

Table 2.4: Mesh refinement results

	Setup		Results					
	Comp. time [h]	Cells [Million]	Forces			Moments		
			$C_D.A$	$C_Y.A$	$C_L.A$	$C_{Mx}.A.b$	$C_{My}.A.b$	$C_{Mz}.A.b$
Low-speed corner								
$h = 1.0$	44.5	31.4	1.578	-0.043	-3.340	0.039	-0.121	-0.335
$h = 1.4$	14.6	14.2	1.575	-0.050	-3.309	0.033	-0.138	-0.344
$h = 2.0$	6.9	6.7	1.587	-0.061	-3.313	0.045	-0.162	-0.363
High-speed corner								
$h = 1.0$	37.9	31.6	1.629	0.084	-3.429	0.053	-0.212	-0.171
$h = 1.4$	15.2	14.0	1.626	0.083	-3.364	0.085	-0.196	-0.179
$h = 2.0$	6.9	6.7	1.588	0.078	-3.284	0.092	-0.183	-0.176

Besides presenting the results, it was found fit to also display the number of volume elements and how long it took the solver to complete the simulation as they play an important role to make a decision on which cell size fits best for this work. After obtaining these results, it was possible to estimate the error and uncertainty. It turned out that the multiple variables convergence were non-monotonic, leading to a calculation of two constants: α_1 and α_2. Estimated uncertainty was proven to have a considerable value, also due to the safety factor being three. These results can be seen in Fig. 2.26 for three variables of interest downforce, drag and pitch moment.

For a clearer analysis, it is now presented Tab. 2.5, with respect to the lift coefficient to understand the error and uncertainty orders of magnitude and the constants obtained in this process, where

ϕ_0 or ϵ_ϕ - Guess of exact solution or error for null cell size;

U_ϕ - Uncertainty;

α_1 - First order error constant;

α_2 - Second order error constant.

Table 2.5: Numerical error and uncertainty estimation results for $C_L.A$

	Error		Uncertainty		
	ϕ_0	ϵ_ϕ	U_ϕ	α_1	α_2
Low-speed corner - A1	3.5317			-0.27435	0.082373
$h = 1.0$	-	0.19198	0.57593	-	-
$h = 1.4$	-	0.22264	0.66791	-	-
$h = 2.0$	-	0.21921	0.65762	-	-
High-speed corner - A2	3.6282			-0.22700	0.027487
$h = 1.0$	-	0.19951	0.59854	-	-
$h = 1.4$	-	0.26393	0.79178	-	-
$h = 2.0$	-	0.34405	1.0322	-	-

Having all this information, it is possible now to make a founded conclusion regarding the mesh size to choose for further analysis. It was considered that results obtained using $h = 1.0$ did not justify the

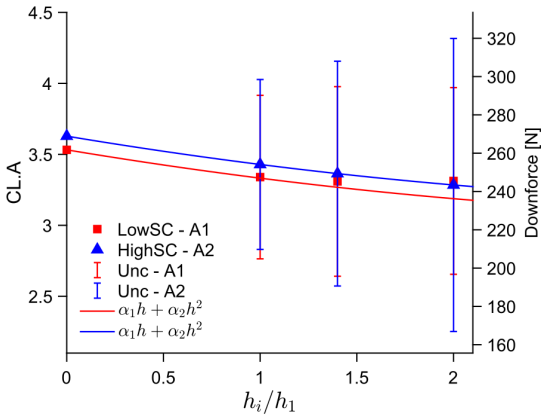

(a) Downforce

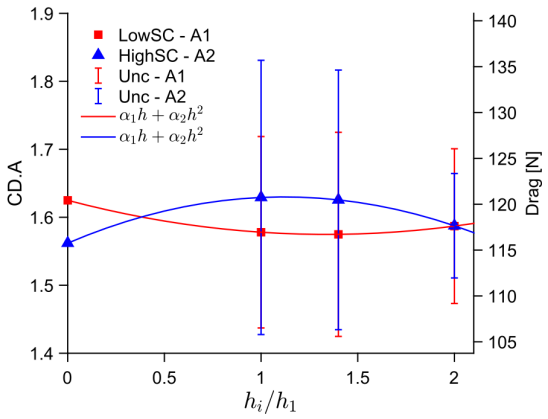

(b) Drag

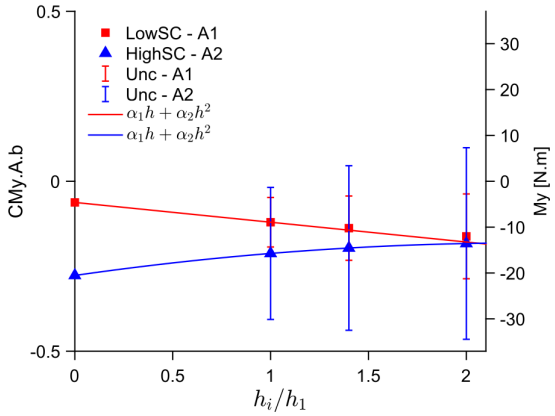

(c) Pitch Moment @CoG

Figure 2.26: Numerical uncertainty and error estimate for low and high-speed corner attitudes

extra computational cost when compared to $h = 1.4$. As this work is based on trends, practically the same conclusions can be drawn while using $h = 1.4$ and saving half of the simulation time. Because a high number of simulations is expected to be performed, it was found the best option for this work to use $h = 1.4$ from this point onwards.

Chapter 3

Simulation Setup

In this Chapter, the remaining simulation conditions will be described, followed by the post-processing data and finally a description of the macro created to automate the process.

3.1 Straight Line Simulation Setup

Previously, in Chapter 2, cornering type simulation was analysed but more types of simulations were performed in this work, namely straight line symmetrical and side wind simulations. These simulations were particularly helpful for parametric studies where each parameter of study was isolated.

3.1.1 Lateral Symmetric Conditions Using Half Vehicle

There is a case where symmetric condition can be assumed. When the turning radius (R), roll angle (ϕ), yaw angle (ψ) and steering angles (δ_i and δ_o) are null, it is expected that the solution is approximately symmetric from one side of the vehicle to the other. Taking advantage of this condition, the domain of study can be cut in half, reducing computational time by only studying half of the car and then ”mirroring” the results to the opposite side.

To conduct symmetrical simulations, some adjustments were made with respect to boundary conditions and domain of study in comparison to the corner type simulation, addressed in Sec. 2.2. The domain is now shaped like a parallelepiped with the dimensions previously represented in Fig. 2.12 with exception of the width, that is now only six meters wide. In this type of simulation, there are no additional source terms to the NS equations, and reference frames were not used since it is a straight line condition. Only the right side of the car was simulated, as illustrated in Fig. 3.1.

The changes in boundary and initial conditions were:

- **Whole Domain:** An initial condition of constant velocity (equal to the inlet velocity) was applied to the entire domain to speed up convergence;
- **Inlet:** A velocity inlet boundary condition was also used but, this time, set to $V = 11\ m/s$ in x-axis direction, the air velocity in study;

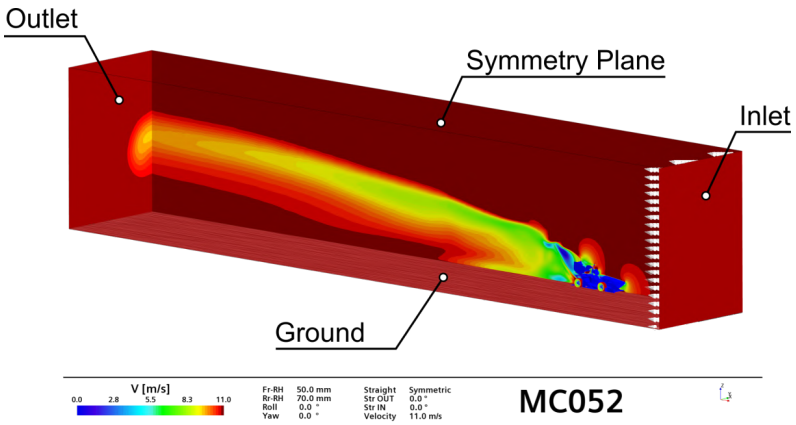

Figure 3.1: Symmetrical simulation boundary conditions

- **Wheels:** The same approach was used to impose a wall rotation boundary condition but, this time, it is only dependant on wheel centre height since there is no steering angle and the wheel speed is constant;
- **Ground:** The lower surface representing the ground is also a no-slip wall, having a velocity associated to simulate the moving ground. This velocity is the same as the inlet;
- **Symmetry Plane:** To model an imaginary symmetry plane, a symmetry plane boundary was chosen. This type of boundary imposes a null value for normal gradients and variables of interest, working the same way as a slip wall.

3.1.2 General Conditions Using Complete Vehicle

There are other attitudes corresponding to a straight line case ($R = 0$) that are not symmetric. These conditions will be addressed in this Section.

In a straight line scenario, if either roll or yaw angles are different from zero, then a full car simulation must be done. Although roll angle is not usually associated with straight line cases, it was useful to include it here for parametric studies as will be discussed in Sec. 4.2. The yaw angle in a straight line case is related to a presence of side wind, meaning that the air and ground velocities are different.

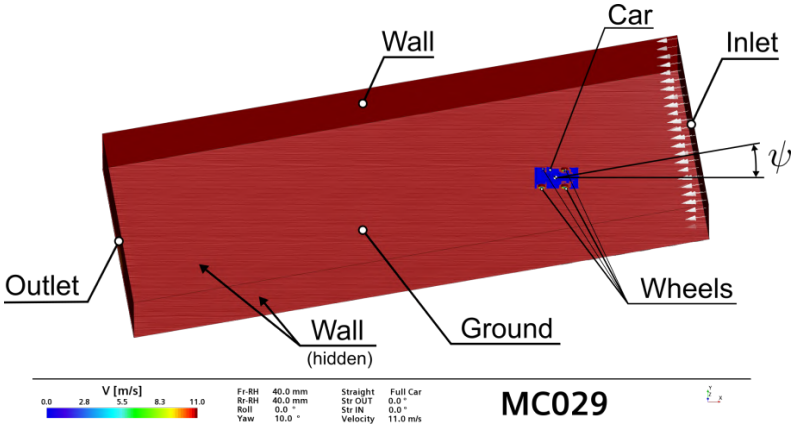

Figure 3.2: Boundary conditions of a full car simulation in a straight line

The setup of this condition is very similar to the symmetrical one. The boundary conditions that differ are:

- **Whole Domain:** The domain is rotated around the CG so that freestream air orientation matches the yaw angle in study ψ ;
- **Inlet:** The same procedure is applied here with $V = 11\ m/s$, normal to the boundary surface to keep the same Reynolds Number;
- **Ground:** Ground velocity is always applied in the vehicle's x-axis direction, meaning that in the side wind cases, the ground travels in different direction than the air, as shown in Fig. 3.2.

3.2 Process Automation

The remaining and last step of a CFD simulation workflow post-processing will be detailed, as itemizing the images and results exported of each simulation and respective details. Lastly, a brief overview of the macro created to automate CFD process will be given.

3.2.1 Post-Processing

The output files of each simulation will be detailed, namely: pre-checks, monitors, static and total pressure coefficients. This last step is important to obtain the final results and to provide tools to analyse and understand the mechanisms and changes that are causing those results.

Before heading into the specific data, a brief introduction about the views is now presented. In car surface plots, different orientations were chosen for the purpose of acquiring all the information around the vehicle. A total of fourteen views were created (all sides and corners), as shown in Fig. 3.3, and they were used consistently throughout the entire work. In symmetrical cases, the results are mirrored to the other side but, to not have repeated data, only nine images are produced (excluded Figs. 3.3(b), 3.3(d), 3.3(g), 3.3(k) and 3.3(m)).

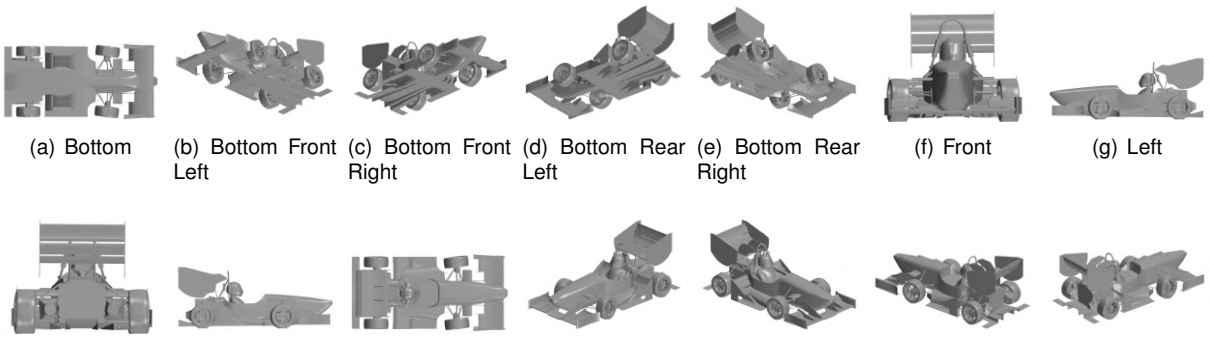

(a) Bottom (b) Bottom Front Left (c) Bottom Front Right (d) Bottom Rear Left (e) Bottom Rear Right (f) Front (g) Left

(h) Rear (i) Right (j) Top (k) Top Front Left (l) Top Front Right (m) Top Rear Left (n) Top Rear Right

Figure 3.3: Views orientation of the surface plots around the vehicle

Pre-Checks

During the pre-processing phase, some images are produced for check-up. These pre-checks allow to confirm/verify that the setup is correct and, if an error is identified, the simulation can be stopped before the time-consuming process of solving the solution.

It starts with the geometry that, after being imported, it is plotted to check if every part was correctly imported. An example of these images is shown in Fig. 3.3. Next, the coordinate systems are created based on the surfaces imported (radiators, fans, wheels, CG) and different views are exported to verify the auxiliary coordinate systems position, having one example shown in Fig. 3.4(a). After domain and refinement boxes are created, the same procedure is followed, making images similar to Fig. 2.14. For the latter stage of pre-processing, the surface mesh is verified to ensure that there are no parts intersecting the ground or any errors during mesh generation (Fig. 3.4(b)). The last step of this verification process is to check the boundary conditions on the first iteration, shown in Fig. 3.4(c).

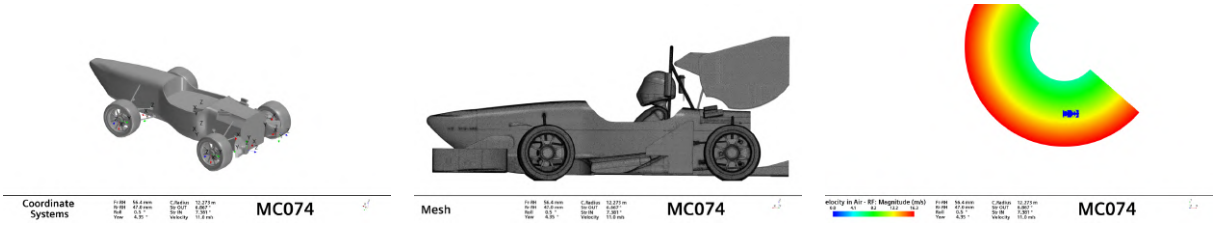

(a) Isometric view of coordinate systems (b) Left view of surface mesh (c) Top view of boundary condition

Figure 3.4: Examples of images created for verification of pre-processing

Monitors

During the solver process, it is important to track the convergence behaviour over the iterations using several monitors. Residuals are one of the most important aspects to take into consideration to assess convergence of a solution. It is a way to represent the imbalance resulted from the discretized equations for all cells. Residuals were not scaled or normalized and the equations monitored were continuity, momentum in each direction, energy, turbulent kinetic energy and specific dissipation rate. An example of the residuals for a typical corner simulation is shown in Fig. 3.5 where they decrease some order of magnitude and stagnate in around two hundred iterations exhibiting an oscillatory behaviour for the solution.

Although residuals are fundamental to judge convergence, they are not sufficient. Other quantities of interest must be also analysed such as forces and moments that were previously mentioned in Sec. 2.4.2. The quantities monitored during the solver convergence process were:

- Centre of Loads: This monitor was included to get an approximate value of the vehicle's centre of pressure. Centre of loads reports the position where the moment is minimal and it is a good way to get a first idea of centre of pressure;
- Cooling: Pressure drop and rise in each radiator and fan respectively were monitored and also mass flow rate across the cooling assembly to ensure the interfaces are working as desired;

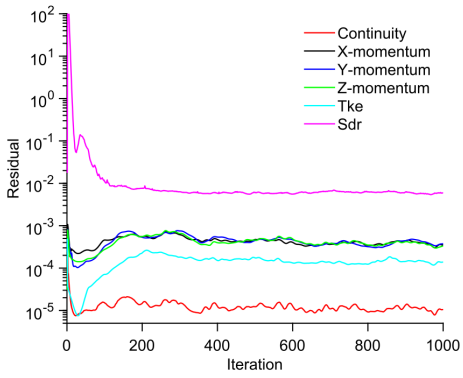

Figure 3.5: Residuals monitor

- Forces: Forces in all three directions were monitored, including overall values and also breakdown on each aerodynamic component. For the sake of easier visualization, two examples of force monitors are displayed in Fig. 3.6, that only include the overall downforce and drag (excluding force breakdown components);
- Moments: Overall moments were measured, in both CG position and origin;
- Solver Time: The last monitor was the solver time spent in each iteration. This helped in getting an estimate time to complete the simulation and assessing if over usage of the computational power was imminent.

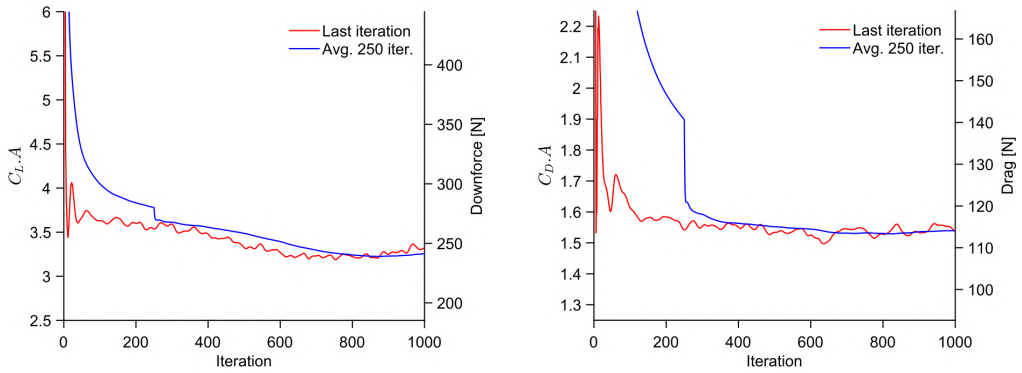

(a) Total downforce

(b) Total drag

Figure 3.6: Example of total vehicle force monitors

Pressure Coefficient

The first post-processing images were related to surface (static) pressure coefficient C_p around the vehicle

$$C_p = \frac{p - p_\infty}{q}\,, \tag{3.1}$$

where p is the static pressure and q represents the dynamic pressure that makes the coefficient adimensional.

This allows to analyse the pressure field that ultimately gives rise to the resulting forces and moments, better understanding the cause of the obtained results.

The dynamic pressure q defines the freestream conditions, or the undisturbed flow far upstream the vehicle. There are two different ways to calculate this dynamic pressure depending on whether it is a straight line using car velocity V, or a corner simulation where it depends on the local radius r,

$$q = \begin{cases} \frac{1}{2}\rho V^2, & \text{if } R = 0 \\ \frac{1}{2}\rho(\omega r)^2, & \text{if } R \neq 0 \end{cases} . \tag{3.2}$$

An introduction is now given to explain the legend structure created that is common to all images. The image was divided to separate the image content at the top from the additional information about the simulation at the bottom, as exemplified in Fig. 3.7.

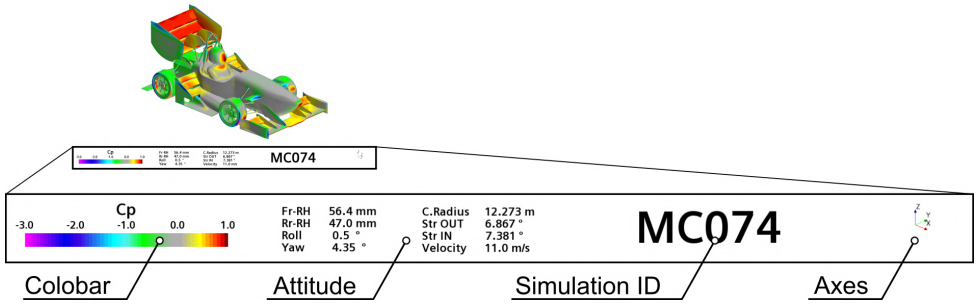

Figure 3.7: Legend structure of exported images

As displayed in Fig. 3.7, the legend has four different regions of information:

- **Colourbar:** At the bottom left corner, it is shown the colour scale and bar used. Custom colourbars were created for a better and faster analysis of the post-processing data. In the case of C_p, a neutral colour (grey) is attributed to $C_p = 0$, to highlight areas where there is relevant change of pressure. The pressure side is positioned to the right, and it is coloured by warm colour tones with yellow and red. The upper limit has a value of one that is related to the stagnation areas and is represented by a different colour (darker red/brown) to be directly identified. Low pressure side has an increased range since the magnitude is higher, and is linked to cold colour tones. Since green and blue were not enough to capture low pressure areas, pink was additionally introduced to represent very low pressure areas;
- **Attitude:** Information about the simulation setup is displayed in two columns. The first column includes front and rear ride heights, roll and yaw angles and the second column has the inner and outer steering wheel angles, velocity magnitude and corner radius (or type of straight line simulation). With this information displayed in every image, it is easier to understand the correspondent attitude of each image when comparing side by side;
- **Simulation ID:** Each simulation had a unique run identification number. In the case of Fig. 3.7, *"MC"* designate the initials of the author (Miguel Carreira) followed by *"074"* that is the run number of this work. Assigning an ID number to each simulation helps to organize and find the desired data when needed;

- **Axes:** The last component of the legend is the display of axes to allow a better understanding of the current orientation view.

An example of this image from the underside is now given in Fig. 3.8. Note the low pressure areas in front wing in green and blue and even lower pressure in lateral diffuser in pink. It is also noticeable the stagnation area in the front wing leading edge, monocoque's nose and front wheels, represented in dark red.

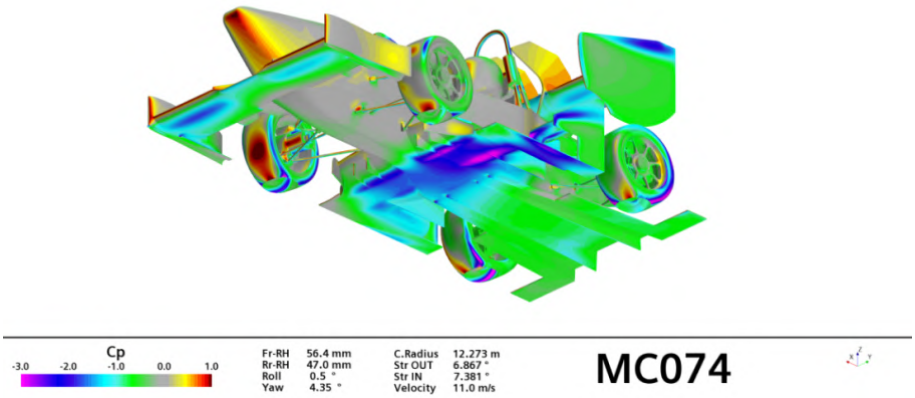

Figure 3.8: Example of static pressure coefficient C_p in bottom front left view

Total Pressure Coefficient

The second type of post-processing images is focused on displaying airflow information throughout the vehicle rather than checking vehicle's surface as previously. Cross sections are created for these "slices" using constant coordinate planes and it is possible to see the flow structures by colouring total pressure coefficient, related to the flow energy. It is possible to understand not only how vortices are behaving during its formation or even bursting, but also separation zones and wake.

At first glance, these cross sections views might not be easy to locate so, some additional information was attached to the legend. An example of a legend is shown in Fig. 3.9, where it is possible to see two additional things that replace the axes information from C_p plots: plane and coordinate. In this case, a side view of the vehicle is displayed in black, and with a red vertical line, the cross section plane is represented. This red line updates depending on the plane coordinate that is shown to the right as in the example "$X = -1565.0\ mm$" .

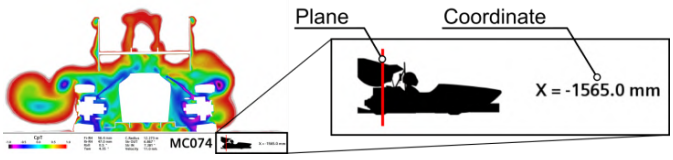

Figure 3.9: Legend change for total pressure coefficient plot

In Fig. 3.9, it is shown a section view legend in x-axis direction but the same method was applied for the other two directions. The legend suffered minor changes for other cases: in y-axis, it is represented a top view of the vehicle as in Fig. 3.10(a); regarding z direction sweep, the plane is now an horizontal red line (shown in Fig. 3.10(b)).

(a) y-axis (b) z-axis

Figure 3.10: Additional plane section views for different axis

Along the x-axis, an image is exported every fifteen millimetres, making a total of two hundred a nineteen images for this sweep. Along y and z directions, the images are spaced by nine and ten millimetres, respectively. With this information across the solution, it is possible to capture all the flow features. An example of the information contained in each image is shown in Fig. 3.11.

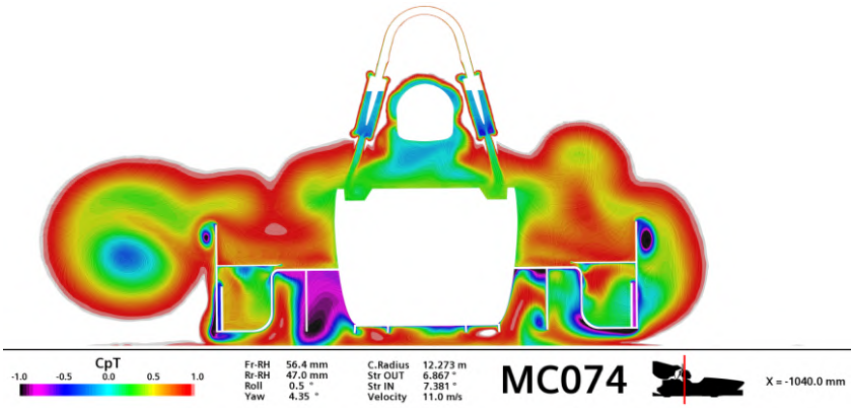

Figure 3.11: Total pressure coefficient example

As explained previously, the image is coloured by total pressure coefficient but there are also shown subtle velocity field lines (LIC) to represent flow direction. A different colourbar was created for this analysis to better adjust the flow characteristics. Undisturbed flow is represented in white and then transits from warmer to colder tones, finishing in pink and then black to characterize regions of very low energy / total pressure coefficient. This image is positioned between the wheels, sectioning the expansion zone of the lateral diffuser. It is visible that on the left side of the figure the diffuser has stalled, having a massive region with pink and black while on the right side airflow remains attached. It is also noticeable the endplate vortices generated at the terminal plate of side elements, positioned on both lateral ends, having the vortex core represented by black.

3.2.2 Macro

As a high number of simulations is expected to be made, it was found fit to automate the CFD simulation to avoid a large amount of repetitive tasks, that are prompt to user error and consume time

that can be used more efficiently somewhere else. So, to better allocate time resources, it was invested some time to create a macro that executes the entire CFD simulation workflow.

Simulation

With respect to the CFD simulation, the workflow was scripted having the goal in mind of just pressing a play button to run the entire simulation and export the results for later analysis. The software used is *Simcenter Star-CCM+®* version 2020.3 R8 (that uses double precision as mentioned before) and the macros executed use the *Java* programming language. Several workstations were used to perform CFD simulations, with $64Gb$ of RAM and a 4 or 12 core processor.

The first step to create the macro files consisted in performing each step manually while taking advantage of the feature *"recording Macro"*, that adds a command to the macro file for each action made manually by the user. The files of each step were then compiled into several modules for each major subtask, that are called by a more general macro that play the entire process. These files were then adapted to integrate variables that are dependant on the input desired (the only interaction from the user is to change the input variable in the code shown in Fig. 3.12(b)). The macro was also modified to include all three types of simulation, based on the input by applying *if conditions* that are represented in Fig. 3.12(a) and *for cycles* were useful mainly to export post-processing data. The macro workflow is represented with a flowchart in Fig. 3.12(a), starting with the intent of creating a new simulation up to exporting the results in a CSV format file and post-processing data.

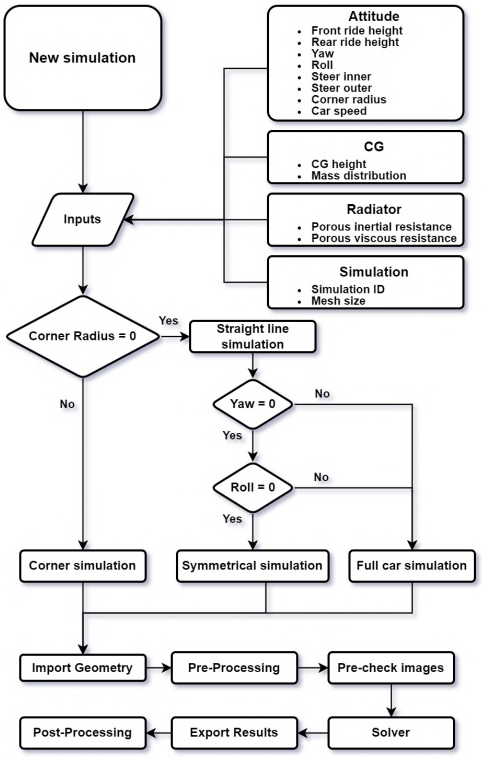

(a) Macro workflow flowchart

```
//{ // INPUT VARIABLES
double Fr_Rh = 40.0;
double Rr_Rh = 40.0;
double Yaw = 0.0;
double Roll = 0.00;
double Steer_IN = 2.571;
double Steer_OUT = 2.505;
double Corner_Radius = 34.68;
double Car_velocity = 11;

double CoGZ = 0.302;
double Mass_Dist_Front_Total = 0.474;

double Porous_Inertial_Resistance = 57;
double Porous_Viscous_Resistance = 592.0;

double Ri = 2.74;

int SIM_ID = 32;
//}
```

(b) Input variables code

Figure 3.12: CFD simulation macro

Reports

As there is a substantial amount of data from all the simulations, an Excel sheet was made to gather it all in one organized place for easy access when needed. To accomplish this, a small macro was produced in Excel that reads the exported CSV type file and copies the data into the correct cell depending on the simulation. This macro was written in *Visual Basic* programming language and it was assigned to the "Import Data" button positioned on the top left corner of the datasheet, as shown in Fig. 3.13.

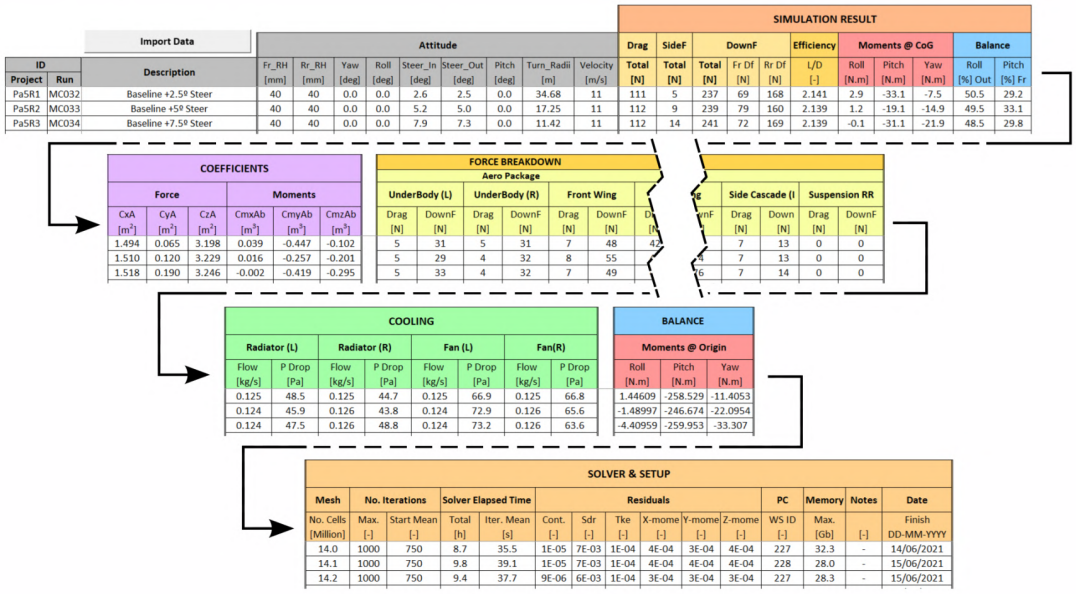

Figure 3.13: Datasheet with simulation results

A section of the Excel sheet is shown in Fig. 3.13 that includes three example simulations to show its structure. It starts with the simulation setup coloured in grey that includes the ID (project name and a run number), a brief description of the simulation purpose, followed by the attitude in which the car was set to. The simulation results are shown right after, with the forces, moments, efficiency and balance. Following the overall results, there is a force breakdown in yellow containing both downforce and drag of each component (some are omitted for brevity). In green, there is the cooling section, that has mass flow and pressure drops and coloured in orange there is information regarding the solver and workstation, such as computational time, number of cells, residuals, computer used and date of simulation.

Lastly, the moments at the origin, required to calculate the balance are shown. Two types of balance are represented that consist in two moment balances about the wheel contact patch. Pitch moment balance around front wheels (origin), M_{y_0}, gives rise to the front wheels ratio of downforce,

$$Balance\ Front\ [\%] = 100 + \frac{M_{y_0}}{WheelBase \times Downforce} \times 100\,, \tag{3.3}$$

and a roll moment balance around the car centre, M_{x_0}, quantifies the proportion of load in the outer wheels when compared to the total downforce,

$$Balance\ Outer\ [\%] = \frac{M_{x_0}}{(Track \times Downforce) + 0.5} \times 100\,. \tag{3.4}$$

Chapter 4

Parametric Analysis

Now that the setup and automation is set, all the tools necessary for study analysis are complete.

A parametric analysis is performed to evaluate the influence of each parameter of interest on the results. It is also called sensitivity analysis, in which only one parameter is changed at a time. This study includes all parameters of interest shown in Sec. 2.1.3: ride heights, roll, steering and yaw angles. A baseline setup was chosen as a starting point for comparison as detailed in Tab. 4.1. Ride heights were set at forty millimetres (front and rear), that is somewhere in between the ground clearance limits, using a zero degree pitch angle as a default angle of attack. The remaining angles (yaw, roll and steer) were also set to zero so that each variable can be isolated to minimize the influence on other parameters. This attitude also allowed for the baseline to be in a symmetrical condition to decrease computational time spent.

Table 4.1: Baseline settings for parametric study

	Fr-RH $[mm]$	Rr-RH $[mm]$	Yaw $[^\circ]$	Roll $[^\circ]$	Steer In $[^\circ]$	Steer Out $[^\circ]$	Turn Radii $[m]$	Velocity $[m/s]$
Baseline attitude	40.0	40.0	0.0	0.0	0.0	0.0	0.0	11.0

4.1 Ride Height

The first parameter in study is the ride height. As already mentioned, the front and rear ride heights are connected to each other and can not be disassociated from one another. For instance, if we keep the rear ride height constant and change the front one, the change in pitch angle leads to a different expansion angle of the diffuser. For this reason, the front and rear ride heights will be analysed together.

The range of ride heights was set based on the travel suspension and usual ride heights configurations, up to any part scraping the floor resulting in a range of $[20\ mm, 60\ mm]$ for the front ride height (FRH) and $[20\ mm, 80\ mm]$ for the rear (RRH). As the rear suspension contains softer springs, the interval of possible values is larger. A sample selection was needed to cover this entire envelope of ride height values and a spacing of ten millimetres was chosen to evenly distribute the samples, totalling in

thirty-five simulations. All points correspond to symmetrical studies, speeding up this process.

The results obtained from these simulations are shown in Fig. 4.1, that display $C_L.A$, $C_D.A$ and pitch moment balance since the other forces and moments are zero, in these symmetric conditions. The baseline (FRH40-RRH40) is coloured in white and then increase/decrease are represented in red or green depending on the variable.

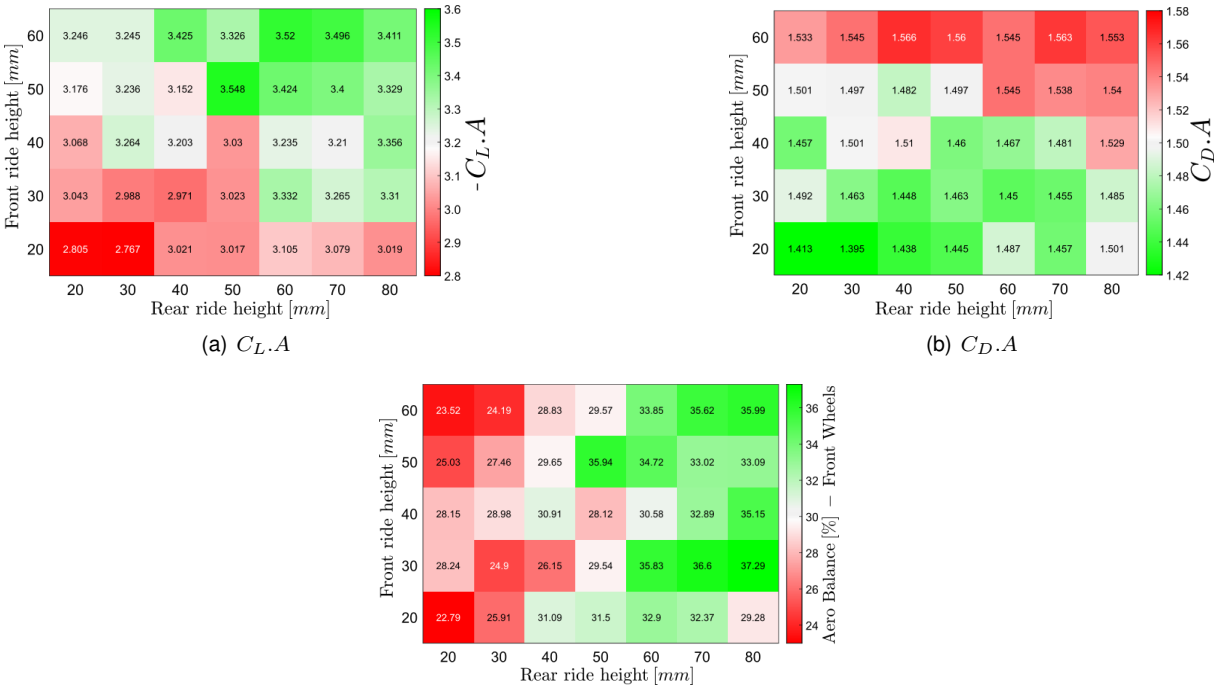

(a) $C_L.A$

(b) $C_D.A$

(c) $Aero\ Balance\ \%\ -\ Front\ Wheels$

Figure 4.1: Results for ride height parametric analysis

Starting from the Fig. 4.1(a), an increment in $C_L.A$ is generally better so is coloured in green, while red means a loss in downforce. There are two distinct areas, one around the bottom left corner in red and at the top right corner in green. Lower values of front and rear ground clearance are associated with lower downforce numbers. In an attempt to identify the cause of this behaviour, it was checked the C_p plot for three configurations coinciding with the bottom left corner, image centre and top right corner shown in Fig. 4.2 in the same order. It is visible that the low pressure areas at the front wing and lateral diffuser are smaller in size and magnitude with lower ride heights. It was also noticed that the footplate vortex [29] did not form when closer to the ground, leading to a loss in downforce in the front wing. The low pressure associated with the vortex core is barely visible in Fig. 4.2(c) increasing low pressure area under the front wing. With respect to the diffuser, it also reduces in efficiency when closer to the ground. It might be ”saturated” and reached the point where downforce starts to decrease with lower distances to the ground [30]. The less mass flow of air entering the diffusers may be also a reason for this behaviour.

The same overall trend can be found in the C_D between bottom left and top right corners while looking at Fig. 4.1(b), but this time it is displayed in opposite colours because lower drag is beneficial. The induced drag is the reason these two variables are linked reaching the same conclusion.

However, the aero balance response was different. On the left side region in Fig. 4.1(c) the balance shifts backwards, while on the right side has more downforce on the front wheels. It seems this balance

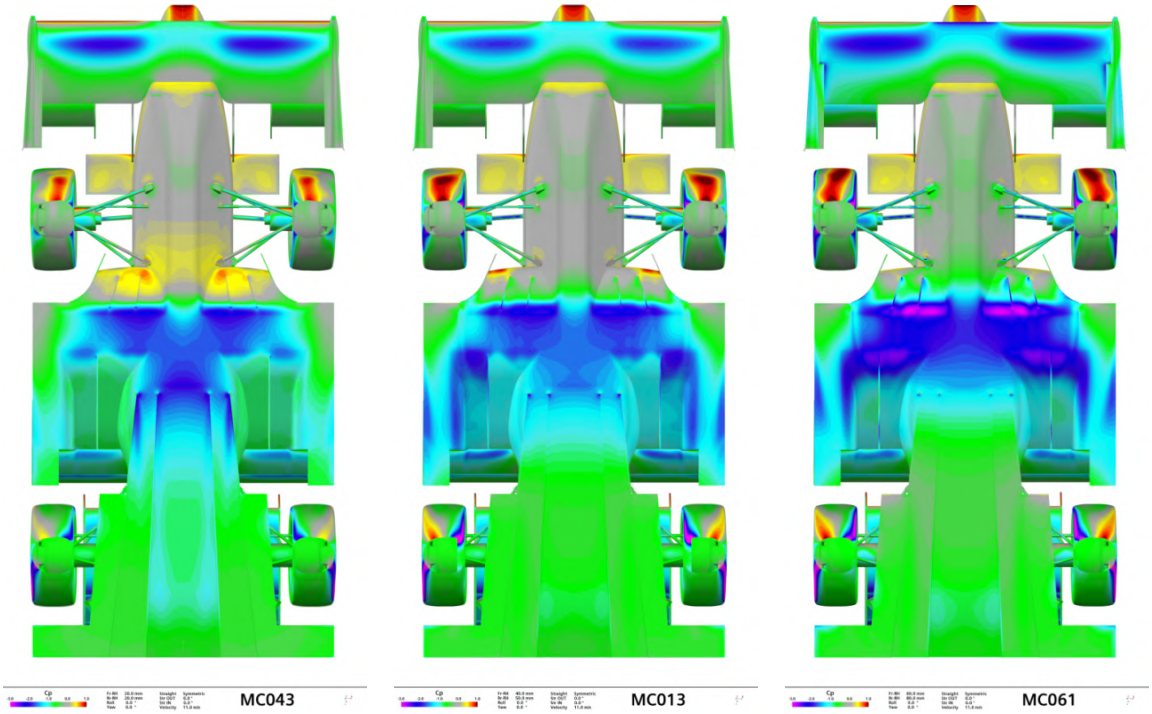

(a) FRH20-RRH20: $C_L.A = 2.805$ (b) FRH40-RRH50: $C_L.A = 3.03$ (c) FRH60-RRH80: $C_L.A = 3.411$

Figure 4.2: C_p from bottom view for comparison between different values of ride heights

is more related to the vehicle's pitch angle than the ground clearance itself.

4.2 Roll Angle

The following parameter of interest is the roll angle ϕ, being the maximum value for this angle set to two degrees. This value is not very high due to the high roll stiffness of this type of cars and together with low ground clearance of diffusers and front wing. To cover this interval of $[0°, 2°]$, a step of half a degree was chosen, keeping the remaining attitude settings at the baseline, giving rise to the results in Tab. 4.2. For an easier understanding of the results trend, they are also represented graphically in Fig. 4.3.

Table 4.2: Roll angle parametric study

Roll angle	Forces			Moments		
$\phi[°]$	$C_D.A$	$C_Y.A$	$C_L.A$	$C_{Mx}.A.b$	$C_{My}.A.b$	$C_{Mz}.A.b$
0.0	1.510	0.000	-3.203	0.000	-0.358	0.000
0.5	1.499	0.003	-3.173	0.002	-0.383	0.023
1.0	1.501	0.018	-3.028	-0.006	-0.526	0.015
1.5	1.474	0.038	-3.007	-0.013	-0.509	0.020
2.0	1.454	0.051	-2.915	-0.014	-0.478	0.032

It is possible to conclude that $C_D.A$ and $C_L.A$ have a downward trend with increasing roll angle. As the outer side of the front wing gets closer to the ground, a similar behaviour to low ride heights is observed, bursting the footplate vortex on the right side of the vehicle. This phenomenon is captured

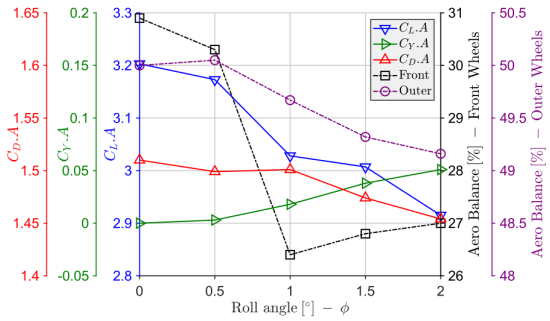

Figure 4.3: Roll angle parameter study

in Fig. 4.4 where it is noticeable the burst vortex in Fig. 4.4(b), corresponding to $\phi = 1.0°$, where the wing is closer to the ground, but when $\phi = 0.0°$ in Fig. 4.4(a) the vortex is well generated. This bursting reduces the low pressure region under the wing causing a significant drop in the front downforce when reaching one degree (almost four percentage points), shown in black.

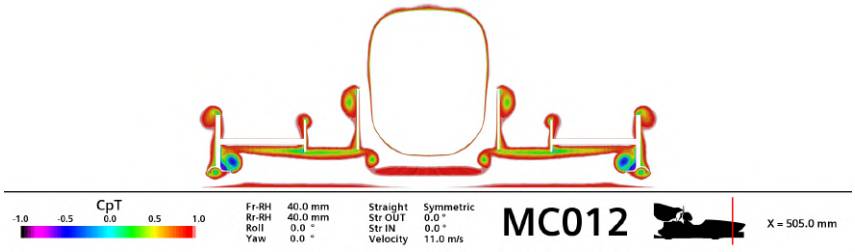

(a) $\phi = 0.0°$

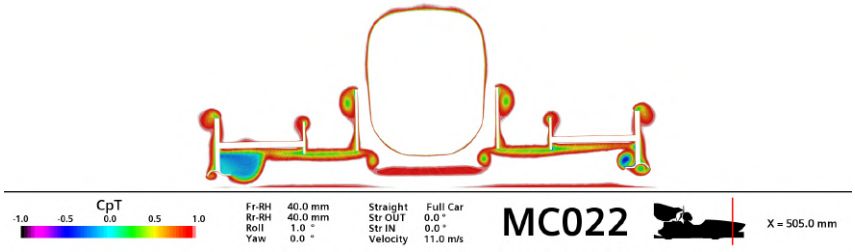

(b) $\phi = 1.0°$

Figure 4.4: C_{pT} section visualization for comparison between different roll angles

The balance starts slowly shifting backwards with increasing roll angle, being the only variable that does not resemble a monotonic function. The reason for this change is that the right lateral diffuser starts producing less downforce when closer to the ground. Mainly the flat outer portion of the diffuser exhibits a smaller low pressure region, visible in Fig. 4.5. As this loss of downforce is located towards the backside of the vehicle, it leads to an increase of the front wheel percentage load.

Since the left side is working ”better” than the right side, a side force $C_Y.A$ is also produced in the positive y-axis direction, as displayed with a green line. This increasing side force generates a negative rolling moment (C_{Mx}), transferring some load from the outer to the inner wheels, as seen in purple colour.

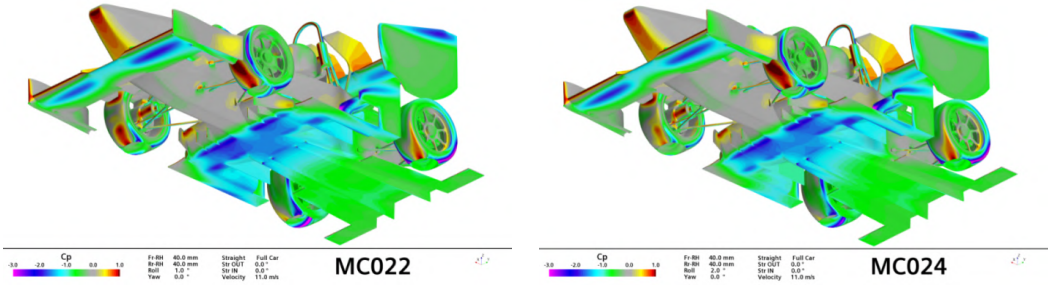

(a) $\phi = 1.0°$ (b) $\phi = 2.0°$

Figure 4.5: C_p visualization from bottom front right view for different roll angles

4.3 Steering Angle

The steering angle δ and consequent turning radius are the next variables targeted, with the averaged steering angle varying within the range $[0°, 12.5°]$. The upper limit value for this variable does not reach the angle correspondent to the maximum steering wheel motion because of self intersecting domain walls with low turning radius. With the full extent of the domain in a tight corner, the outlet wall would intersect the inlet, making it impossible to simulate. Having this in mind, the highest value turned out to be a bit less than seven meters of cornering radius. The sample points to simulate were spaced by two and a half degrees of averaged steering angle between both wheels, since steering angles and corner radius varied quite a lot. The outcome of these simulations are presented in Tab. 4.3 and then in graphic mode in Fig. 4.6. Note the increasing difference between inner and outer wheel steering angle as it increases due to Ackerman effect.

Table 4.3: Steering angle parameter study

Steer avg. $\delta_{avg.}[°]$	Steer in $\delta_i[°]$	Steer out $\delta_o[°]$	Turn Radii $[m]$	Forces $C_D.A$	$C_Y.A$	$C_L.A$	Moments $C_{Mx}.A.b$	$C_{My}.A.b$	$C_{Mz}.A.b$
0.0	0.00	0.00	∞	1.510	0.000	-3.203	0.000	-0.358	0.000
2.54	2.57	2.51	34.68	1.494	0.065	-3.198	0.039	-0.447	-0.102
5.0	5.21	4.95	17.25	1.510	0.120	-3.229	0.016	-0.257	-0.201
7.5	7.94	7.35	11.42	1.518	0.190	-3.246	-0.002	-0.419	-0.295
10.0	10.76	9.70	8.49	1.519	0.275	-3.231	0.001	-0.420	-0.404
12.5	13.69	12.01	6.72	1.508	0.334	-3.174	-0.026	-0.384	-0.487

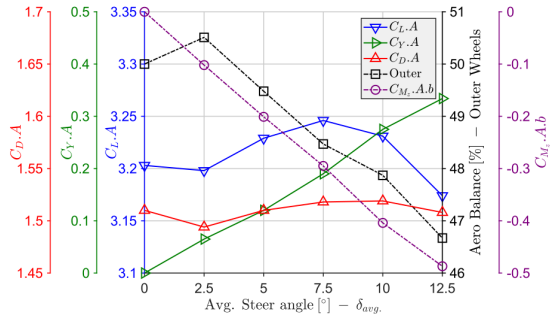

Figure 4.6: Steering angle parameter study

The drag and lift coefficient seem to remain fairly constant throughout the whole range of steering. There is a small increasing and then decreasing trend of the lift coefficient while drag is mostly

unchanged. The side force seems to increase linearly with the steer angle, in a substantial rise in magnitude, starting from zero ramping up to three tenths. These changes in forces are due to differences in low pressure regions located mainly at the front wing and lateral diffusers. The different sideslip angles induced by the flow curvature across the vehicle alter the vortices behaviour and front wheel wake change also interferes with the lateral diffuser performance.

The rolling moment $C_{Mx}.A.b$, expressed as aero balance of outer wheels (coloured in black) starts to slightly increase at $\delta_{avg.} = 2.5°$ but then follows a declining trend, shifting the load to the inner wheels. The yaw moment C_{Mz} shows a linear decreasing trend throughout the entire steering range. This moment always increases in magnitude (with a negative sign) and, as z-axis points upwards, it induces an understeer behaviour to the car. The flow curvature is the cause for this yawing moment, as the different sideslip angles create a moment around the centre of gravity.

To illustrate the impact of the flow curvature onto the flow structures, Fig. 4.7 displays the evolution of the iso-surface $C_{p_T} = 0$ across the steer angle interval, representing the wake throughout the vehicle . The most visible differences are present in the rear wing endplate vortices and front wheel wake (in this image right wheel is more visible). From 4.7(a) to 4.7(c), the rear wing right endplate vortex (left side of image) starts to weaken and, in contrast, the left side vortex has strengthened together with a change in trajectory, following the flow curvature. It is also possible to see that the right front wheel wake changes in position and shape when steering, heading outwards. In the front wing right support plate [1] contains an ever increasing in size vortex due to the side slip angle induced by the turning flow.

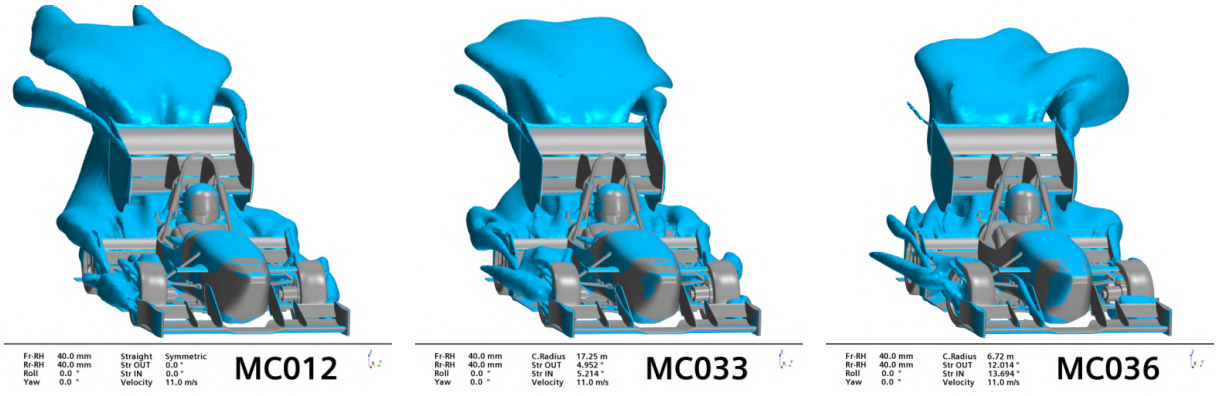

(a) $\delta_{avg.} = 0.0°$ (b) $\delta_{avg.} = 5.0°$ (c) $\delta_{avg.} = 12.5°$

Figure 4.7: Iso surface of $C_{p_T} = 0$ evolution for different steering angles

4.4 Yaw Angle

The last variable of study is the yaw angle ψ. The interval is $[0°, 15.0°]$ and the points simulated were separated by two and a half degrees of yaw angle, while maintaining the remainder settings of the baseline attitude. Since considerable wind can occur during competitions, the limit chosen for this variable was relatively high. The results are shown in Tab. 4.4, being displayed graphically in Fig. 4.8.

[1] Support plate is the plate that serves as a mount from the front wing to the monocoque

Table 4.4: Yaw angle parametric study

Yaw angle	Forces			Moments		
$\psi[°]$	$C_D.A$	$C_Y.A$	$C_L.A$	$C_{Mx}.A.b$	$C_{My}.A.b$	$C_{Mz}.A.b$
0.0	1.510	0.000	-3.203	0.000	-0.358	0.000
2.5	1.497	-0.192	-3.119	0.057	-0.427	-0.007
5.0	1.498	-0.416	-3.060	0.052	-0.434	0.0004
7.5	1.447	-0.518	-2.930	0.084	-0.417	-0.041
10.0	1.384	-0.651	-2.828	0.086	-0.335	-0.067
12.5	1.347	-0.788	-2.693	0.130	-0.296	-0.093
15.0	1.317	-0.894	-2.674	0.125	-0.282	-0.132

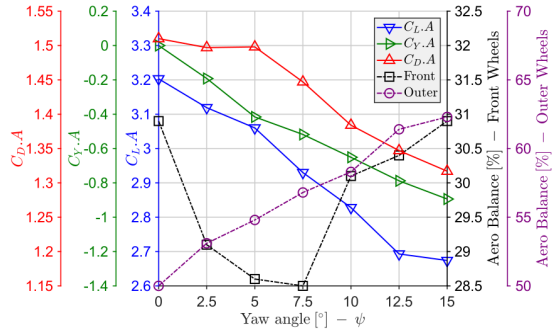

Figure 4.8: Yaw angle parametric study

This parameter of interest revealed to be one of the most sensitive ones, having a wide range of results across the yaw angle interval. All force components feature a downward trend: the downforce coefficient decreases in a somewhat linear way, having this time a much steeper reduction (almost nineteen percentage points from the baseline), and the drag coefficient has the same behaviour, related to less induced drag generated by less downforce. As expected, sideslip angle increases side force substantially, reaching almost a nine-tenth increment of $C_Y.A$ from the baseline. In the car's reference frame, the incoming air is coming from the left, so it makes sense that the side force has a negative y-axis component. The front wheel load is the only parameter behaving in a non-monotonic way, starting to drop down but, after $\psi = 7.5°$, it raises up. The aero balance shifts forward due to a sudden descent in drag force on the rear wing. As the rear wing is positioned above and behind the CG, both the drag and downforce contribute to a negative pitching moment, loading the rear wheels. As the drag decreased significantly starting from $\psi = 7.5°$, it led to an increasing front wheel balance.

In Fig. 4.9, it is possible to understand the consequences of the yaw angle change into the pressure side of the whole car. The driver head stagnation region gives an idea of the incoming airflow angle and the rear wing high pressure reduced greatly at high yaw angles. It is also noticeable in Fig. 4.9(b) some flat plates where the pressure is building up due to sideslip angle as: right side element endplate, midplates [2] and support plates of front wing. The right side support plate even has a low pressure region induced by separation.

Finally, the outer wheel load shows an ever increasing tendency, surpassing sixty percentage points, shifting the centre of pressure outwards. Once again, as the incoming airflow comes from the left side, the front left tyre wake enters into the diffuser, affecting its performance, while the front right tyre wake is directed outward, meaning that the diffuser gets more energetic air comparing to the left side.

[2]Midplate is positioned at approximately quarter span, to support the front wing flap and also reduce wing tip vortices

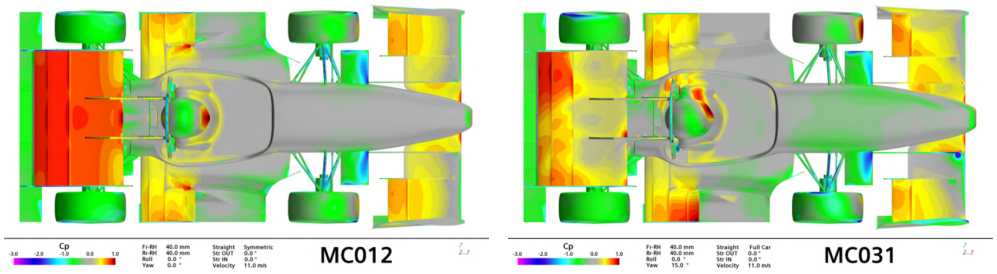

(a) $\psi = 0.0°$ (b) $\psi = 15.0°$

Figure 4.9: C_p visualization from top view from two different values of yaw angle

4.5 Results Summary

Overall, all the parameters studied presented a meaningful sensitivity either to some force component or car balance, that is shown in Tab. 4.5 with percentage changes.

Table 4.5: Parametric study results summary

		Value	Value / $\Delta[\%]$				
			Ride height		Roll angle	Steer angle	Yaw angle
		Baseline	Extreme 1	Extreme 2	$\phi = 2.0°$	$\delta_{avg.} = 12.5°$	$\psi = 15.0°$
Forces	$C_D.A$	1.510	1.395/-7.6	1.545/+2.3	1.454/-3.7	1.508/-0.1	1.317/-12.8
	$C_Y.A$	0.000	-	-	+0.051/-	+0.334/-	-0.894/-
	$-C_L.A$	3.203	2.767/-13.6	3.424/+6.9	2.915/-9.0	3.174/-0.9	2.674/-16.5
Moments	$Bal\,[\%]\,Out$	50.0	-	-	49.2/-1.6	46.7/-6.6	62.3/+24.6
	$Bal\,[\%]\,Front$	30.9	25.9/-16.2	34.7/+12.3	27.0/-12.6	30.2/-2.3	30.9/-0.1
	$C_{Mz}.A.b$	0.000	-	-	+0.032/-	-0.487/-	-0.132/-

Even though the ride height only features three coefficient values different from zero (out of six), they varied substantially throughout the entire working envelope. For example, $C_L.A$ varied within the range $[2.767, 3.548]$ reaching a delta value of 13 percentage points indicating a significant sensitivity to this parameter. Drag and aero balance did not showed such great variation but they were also relevant, changing eleven and fourteen percentage points, respectively.

The roll angle study has proved not to be so sensitive in magnitude compared to the ride height, but was helpful to identify some monotonic trends regarding forces, outer wheel load and a peculiar behaviour with respect to the front aero balance. The maximum magnitude change was the $C_L.A$ with a nine percentage point decrease.

The third variable was the steering angle and a bit unexpectedly, it revealed minor changes in $C_L.A$ and $C_D.A$. Nonetheless, there were some other different important phenomena captured: substantial increase in side force, aero balance shifting outwards by almost four percentage points and the major change was the rise in yaw moment C_{Mz}.

Finally, the yaw angle exhibited a large interval of results, having the most impact of all variables in drag and side force coefficient. $C_L.A$ consistently decreased within the interval $[-3.203, -2.674]$ presenting the largest delta of sixteen percentage points, and reached the maximum value for outside load.

Given all this data, all five variables were found relevant, so this work will continue to include them all.

Chapter 5

Surrogate Model

This work aims to evaluate the aerodynamic performance of a prototype as a function of five variables. As the response of the design variables is found over time-consuming CFD simulations it was opted to build an approximate model, also called surrogate model that attempts to reproduce the behaviour of the simulation model. This will enable a better understanding of the response over the gaps left from the finite number of simulations in a more rapid and effective manner.

Constructing an approximate model requires several steps: design of experiments, construction of the model itself and its validation. These will be approached in this Chapter, complemented by the results obtained using this process.

5.1 Design of Experiments

Surrogate models are usually divided into two different applications: design optimization and design space approximation [31]. Surrogate model based optimization seeks to find an optimum value of interest within the design space D, using an iterative search/update process, where additional simulations/samples are ran around the predicted best value from the model to converge. This work, however, focus on the other type of surrogate, design space approximation, in which the interest is only in the overall behaviour of the system throughout the design space.

A surrogate model $\widehat{f}$ attempts to mimic the response of the "exact" model f, focusing on understanding the input-output behaviour, dismissing the proceedings needed to obtain the output (as a black box). The symbol $\hat{}$ will be used whenever the variable in question is respective to the surrogate model. The function $f(\mathbf{x})$ depends on the design variables and the only way to collect data for it is through discrete observations or samples. To cover the entire design space with discrete points, it requires choosing a sampling plan $\left\{\mathbf{x}^{(1)}, \mathbf{x}^{(2)}, \ldots, \mathbf{x}^{(n)}\right\}$ that establishes an efficient spatial arrangement between samples for evaluation through CFD simulations. This first stage is also called design of experiments (DOE) and it focus on finding the input variables at each point in the input space [32]. In this case, $\mathbf{x}$ consists in five design variables - front and rear ride heights, yaw, roll and steer angles. Each data point results in the output variables $\mathbf{y}$ comprising of six different coefficients of interest for this work (Eq. 5.1).

$$\mathbf{x} = \begin{bmatrix} \mathbf{x_1} \\ \mathbf{x_2} \\ \mathbf{x_3} \\ \mathbf{x_4} \\ \mathbf{x_5} \end{bmatrix} = \begin{bmatrix} FRH \\ RRH \\ \boldsymbol{\psi} \\ \boldsymbol{\phi} \\ \boldsymbol{\delta} \end{bmatrix} \longrightarrow \mathbf{y} = \begin{bmatrix} C_D.A \\ C_Y.A \\ -C_L.A \\ Bal\,[\%] - Out \\ Bal\,[\%] - Front \\ C_{Mz}.A.b \end{bmatrix} \tag{5.1}$$

The main interest in choosing the points coordinates is to minimize the bias error. As the data is acquired through a determinist CFD simulation, there is a numerical error associated with it. Besides the bias error, the empirical error also includes a variance component that can be defined as [32] :

- *Bias:* quantifies the extent to which the surrogate model outputs $\hat{f}(x)$ differ from the true values $f(x)$ calculated as an average over all possible data sets D;
- *Variance:* measures the extent to which the surrogate model $\hat{f}(x)$ is sensitive to particular data set D. Each data set D corresponds to a random sample of the function of interest.

Assuming that the data set includes some type of noise or random element for an average error with a quadratic loss function, the expected error for bias and variance can be expressed as

$$E_{\text{bias}^2}(\mathbf{x}) = \left\{ E_{\text{ADS}}[\hat{f}(\mathbf{x})] - f(\mathbf{x}) \right\}^2 , \tag{5.2}$$

$$E_{\text{var}}(\mathbf{x}) = E_{\text{ADS}} \left[\hat{f}(\mathbf{x}) - E_{\text{ADS}}[\hat{f}(\mathbf{x})] \right]^2 , \tag{5.3}$$

where E_{ADS} is the expected value considering all possible data sets.

These two quantities are linked to each other and there is a compromise between them. If a certain model has low bias error, then the variance is usually high. It is possible to decrease both error components by increasing the number of points in the data set but that adds computational cost. The bias error can also be reduced by distributing the design points uniformly through the design space D [33].

Two methods that implement these strategies are Orthogonal Arrays (OA) [34] and Latin Hypercube sampling (LHS) [35]. Although orthogonal arrays are able to have an uniform distribution, it has some drawbacks: the OA may not exist under certain conditions and there is a possibility of including replicate points, that would greatly increase bias error (bias error is usually more significant when dealing with deterministic problems [33], as in this work). For these reasons, it was discarded and implemented a Latin Hypercube sampling strategy that is also most frequent and can be easily implemented using *Matlab®* function *lhsdesign*.

Latin Hypercube sampling is a stratified sampling approach with the restriction of each input variable ($\mathbf{x_k}$) having all portions of its distribution represented by input values [32]. Sampling is done by dividing the range of each design variable $\mathbf{x_k}$ into N_s (sample size) strata of equal marginal probability $1/N_s$, and sample once from each stratum [35]. Denoting the sample by $x_k^{(j)}$ with $j = 1, \ldots, N_s$ and in this case $k = 1, \ldots, 5$, the sample is then constructed with components of the various x_k 's matched at

random. This random element may prompt different levels of uniformity, that can be evaluated in distinct ways: maximizing the minimum distance or minimizing the correlation between points for example. In this case, it was found appropriate to use the correlation criterion that minimizes the sum of between-column squared correlations. This way it is possible to focus on decreasing the dependence among the variable inputs to get more information about the whole data spectre.

A total of fifty samples were distributed using LHS, adding to the existing simulations already made for parametric studies, totalling in around one hundred observation points to construct the surrogate model. This number of additional simulations was found to be a good compromise between simulation time and dataset for the surrogate model. All sample points used are present in Appendix A.1, from which starting on $ID\ 62$ up to $ID\ 111$ are the observations allocated using LHS.

5.2 Construction of Model

There are two distinct types of surrogate models: parametric approach, that assumes there exists a global functional form of connection between input and output that it is known; and the non-parametric approach that utilizes different types of models according to the region, building up a global model (e.g. Radial Basis Functions [36]).

This work adopted a parametric strategy, since the overall aspect is the main concern. The option was to construct the surrogate based on a Polynomial Regression Model (PRG) due to its simplicity to implement [37] . There are also other methods that would fit into this work such as Kriging Modeling (KRG) [38] but it was decided not to enter in too much complexity at this stage, however it may be target of a future and more intricate development in this area.

PRG is a technique that implements a regression analysis (hence its name) to obtain an estimated value for the function of interest f , based on N_{PRG} number of basis functions z_j , with their respective coefficients β. This approximation of the function f is essentially a Taylor series expansion. Intuitively, this expansion is expected to have a better accuracy with increasing order of the polynomial m, therefore different values for m were tested. For example, considering $m = 1$, this method expresses the linear equation for each sample i and basis function j [32]

$$f_i(\mathbf{z}) = \sum_{j=1}^{N_{\mathrm{PRG}}} \beta_j z_j^{(i)} + \varepsilon_i\,, \quad E\left(\varepsilon_i\right) = 0\,, \quad V\left(\varepsilon_i\right) = \sigma^2\,, \tag{5.4}$$

where the error ε_i is assumed to be independent of the sample number with the expected value to be null and variance being σ^2. Representing the first part in matricial form we obtain

$$\boldsymbol{f} = \boldsymbol{X}\boldsymbol{\beta} + \varepsilon\,, \tag{5.5}$$

with X being a matrix containing all the basis functions for every observation point with a size of $N_s \times N_{PRG}$,

$$\boldsymbol{X} = \begin{bmatrix} 1 & z_2^{(1)} & z_3^{(1)} & \cdots & z_{N_{\mathrm{PRG}}}^{(1)} \\ 1 & z_2^{(2)} & z_3^{(2)} & \cdots & z_{N_{\mathrm{PRG}}}^{(2)} \\ \vdots & \vdots & \vdots & \ddots & \vdots \\ 1 & z_2^{(N_s)} & z_3^{(N_s)} & \cdots & z_{N_{\mathrm{PRG}}}^{(N_s)} \end{bmatrix}, \tag{5.6}$$

where the basis functions $z_1^{(i)}$ are simplified with a number 1 as the first basis function is respective to the constant term.

The basis functions z_j include all combinations possible between the design variables coefficients up to a determined maximum order m. For instance, a problem considering two design variables (x_1 and x_2) fitting with polynomial up to order 2 gives result to the following basis functions: $z^{(i)} \in \{1, x_1, x_2, x_1x_2, x_1^2, x_2^2\}$, meaning that there are $N_{PRG} = 6$ coefficients to estimate.

The vector $\hat{\boldsymbol{\beta}}$ containing the unknown parameters can be estimated by

$$\hat{\boldsymbol{\beta}} = \left(\boldsymbol{X}^{\boldsymbol{T}}\boldsymbol{X}\right)^{-1}\boldsymbol{X}^{\boldsymbol{T}}\boldsymbol{f}\,. \tag{5.7}$$

In the end, after estimating the $\hat{\boldsymbol{\beta}}$ vector, the surrogate model approximated output can be found simply by resolving

$$\hat{\boldsymbol{f}} = \boldsymbol{X}\hat{\boldsymbol{\beta}}\,. \tag{5.8}$$

5.3 Validation of Model

The third step of making a surrogate model is validation, necessary to assess the approximate model quality. This evaluation is possible by estimating generalization error, providing information to make a decision about the best model choice.

There are several approaches possible to estimate the generalization error such as: Split Sample (SS) and Cross-Validation (CV) [32]. The SS method is the simplest and, as the name indicates, the data is split into a training and testing set. The training set is used to construct the surrogate model and the testing set is only applied to compute the generalization error from the model. This approach does not use all the computed data to build the model and the generalization error is highly dependant on the dataset division. For these reasons, it was discarded and CV validation was chosen instead. There are more complex ways to validate the model such as bootstrapping but it were not taken into account as CV was found adequate for the time being.

Cross validation takes advantage of the same methodology of splitting the data, but enables the use of the majority of the data (or even the whole data) as training set. The data is split into k-subsets meaning that a surrogate is built k times, each excluding one of the subsets from the training data and using it as testing, to validate the model. The surrogate generalization error is then estimated based on the error from each of the subsets surrogate models.

The strategy chosen to select the data subsets was the leave-one out cross validation method, where

k is equal to the number of samples N_s, exemplified in Fig. 5.1. A surrogate is built $N_s + 1$ times, N_s times to get all subsets into testing once, and one additional surrogate that uses all the data as training.

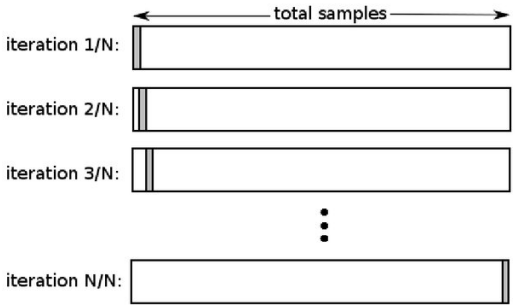

Figure 5.1: Leave one out cross validation [39]

Each subset is taken into account as training data in N_s surrogate models and once as validation data, being this one of the major advantages of the CV over the SS method. The main disadvantage of this approach is that a high number of surrogate models has to be built to validate all the spectrum, but since it is a computationally cheap problem to solve, it is resolved in a short period of time. In this case $N_s = 104 \rightarrow (104 + 1) \times 6 = 630$ surrogate models are built for each polynomial order.

To estimate the generalization error using a mean square error (GMSE) we obtain

$$\text{GMSE } = \frac{1}{k} \sum_{i=1}^{k} \left(f_i - \hat{f}_i^{(-i)} \right)^2 , \tag{5.9}$$

that represents the variation between the function of interest at the test point f_i and the estimated value from the surrogate model that does not include i as training data $\hat{f}_i^{(-i)}$. This generalization error was calculated for each function of interest and for all orders of the polynomials to provide information to make a founded conclusion on which order suits the problem best.

5.4 Results

The process of creating a surrogate model described previously was then executed for multiple polynomial orders m. It was decided to perform the PRG for $m \in \mathbb{N}$, $m \in [1, 12]$ and computing the GMSE by cross validation for each order to assess which order results in a smaller error. This value was chosen based on *Forrester et al.* [40] saying that usually $m \leq 15$, and a maximum value of 12 was found to be plausible.

The results obtained from the regression analysis were consistent throughout all functions of interest having the polynomial of order two the smallest GMSE in all cases as shown in Tab. 5.1. The error reduces from order 1 to 2 and then it starts to increase almost exponentially up to the maximum order chosen. Although the model is more ”flexible” with increasing order, it also enables the possibility of over adjusting to the data noise and not capture the global solution. After a certain value for m (usually four), matrix ranking started to be deficient and so, the estimated values for $\hat{\beta}$ may not be the best. Together with higher order terms, it may escalate the values, increasing substantially the error.

It should be noted that, for higher order polynomials, a considerably data set is required. which was not available, and they might have led to poorly adjust models.

Table 5.1: Generalization mean square error for different orders of PRG

Max. order PRG	N_{PRG}	GMSE					
m	$\hat{\boldsymbol{\beta}}$	$-C_L.A$	$C_D.A$	$C_Y.A$	$[\%]\,Out$	$[\%]\,Front$	$C_{Mz}.A.b$
1	6	0.0200	0.0013	0.0014	0.7194	7.3009	1.81e-04
2	21	0.0131	0.0006	0.0011	0.6979	6.0992	1.10e-04
3	56	0.0913	0.0021	0.0124	3.8691	30.1952	0.0012
4	126	10.696	0.1333	14.304	1.49e+03	1.86e+03	0.2220
5	252	16.117	1.0141	10.425	1.95e+03	1.87e+04	1.6458
⋮	⋮	⋮	⋮	⋮	⋮	⋮	⋮
12	6188	7.11e+09	1.70e+09	2.78e+06	2.39e+12	7.27e+11	5.11e+06

All results achieved are displayed in a matricial form in Appendix A.2 for all variables of interest. An example of the obtained expression for $-C_L.A$ is represented in full extent by

$$
\begin{aligned}
-\hat{CL}.A = {} & 2.0797 \\
& + 0.031531 \times FRH + 0.0085836 \times RRH + 0.026217 \times \psi + 0.1034 \times \phi + 0.048496 \times \delta \\
& - 8.1955 \times 10^{-5} \times FRH \times RRH - 0.00093097 \times FRH \times \psi + 0.0019702 \times FRH \times \phi \\
& - 0.00026495 \times FRH \times \delta - 2.3425 \times 10^{-5} \times RRH \times \psi - 0.0029023 \times RRH \times \phi \\
& + 0.00020373 \times RRH \times \delta - 0.0025126 \times \psi \times \phi - 0.00084686 \times \psi \times \delta + 0.0069771 \times \phi \times \delta \\
& - 0.00022188 \times FRH^2 - 3.9984 \times 10^{-6} \times RRH^2 - 0.0018687 \times \psi^2 \\
& - 0.089235 \times \phi^2 - 0.0037686 \times \delta^2 \,, \qquad (5.10)
\end{aligned}
$$

where the input units for ride heights is millimetres and angles is degrees. It is possible to see all the parameters and respective basis functions with respect to the five design variables.

To understand how the surrogate fits into the sample data, the observations used for the yaw angle parametric analysis were plotted against the estimation from the surrogate model. This example region is represented in Fig. 5.2(a), where the points display the CFD output and the lines are the estimated values from the surrogate model. It is possible to notice that the polynomial captures the meaningful trends present in the sample data for this area of study. The results for the steering angle are shown in Fig. 5.2(b)and it possible to see some variables do not fit so well, especially $C_L.A$. The remaining parametric results from the surrogate model are shown in App. A.3.

As a small portion of the whole design space is represented in the previous case, only displaying a $1D$ behaviour with constant ride height/roll/steer whereas the entire map is $5D$. In an attempt to better understand the global response throughout the domain, another type of plot was created. To accomplish this, it was taken advantage of a chart tile plot (also called nested plot) where it is possible to include the entire scope of four design variables. One of the design variables must be set as constant, in this case

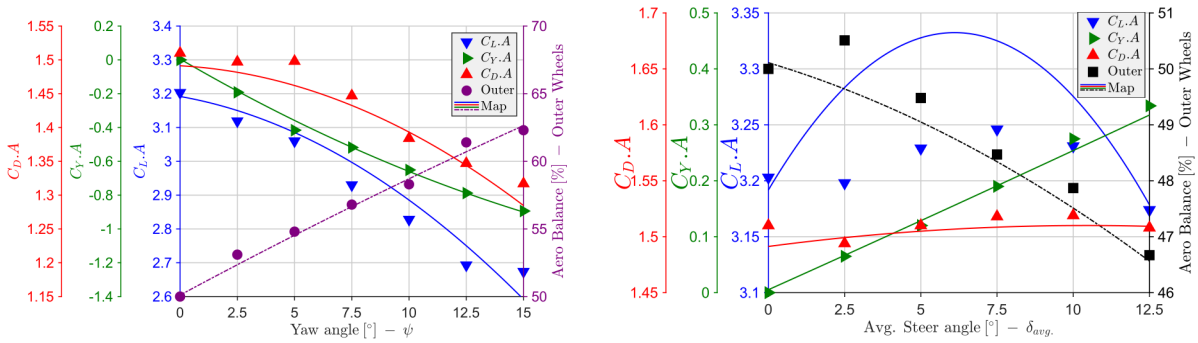

(a) Yaw angle ψ

(b) Steering angle δ

Figure 5.2: Comparison between results from surrogate and parametric studies

it was chosen to keep the yaw angle constant: $\psi = 0.0°$ for Fig. 5.3(a) and $\psi = 15.0°$ for Fig. 5.3(b) to see both ends of the yaw interval. The only function of interest displayed is $-C_L.A$ as a demonstrative example.

This plot is essentially composed by matrices of contour plots (tiles) in which each tile plot two variables against each other. In this case, the row and column of a tile correspond to the front and rear ride heights respectively (global vertical and horizontal axes). On each tile, the roll angle ϕ varies along the horizontal axis and steering angle δ along the vertical axis that are represented on the bottom left corner tile in Fig. 5.3(a) ($FRH = 20, RRH = 20$). Each of these two images include 117,000 points calculated from the resulting polynomial expression Eq. (5.10).

In Fig. 5.3(a), it is possible to see some overall resemblance to Fig. 4.1(a), where warmer colours (higher values) are positioned at the top right corner and cold (lower values) at the bottom left, meaning the global ride height response seems to be similar. Regarding the other two variables, it is possible to check the different behaviour of the roll and steer based on the ride height in study, both in magnitude and shape. The bottom left peak has an almost circular shape while the top right, the peak moves to the left and resembles more like an ellipse.

Looking at Fig. 5.3(b), it is noticeable that the response to ride height looks completely different than before (note that the colourbar magnitude has changed). The model predicts higher values of downforce at the bottom right area for a high value of yaw angle.

The $C_L.A$ evolution is displayed in more detail with more yaw angle intervals in App. A.4.

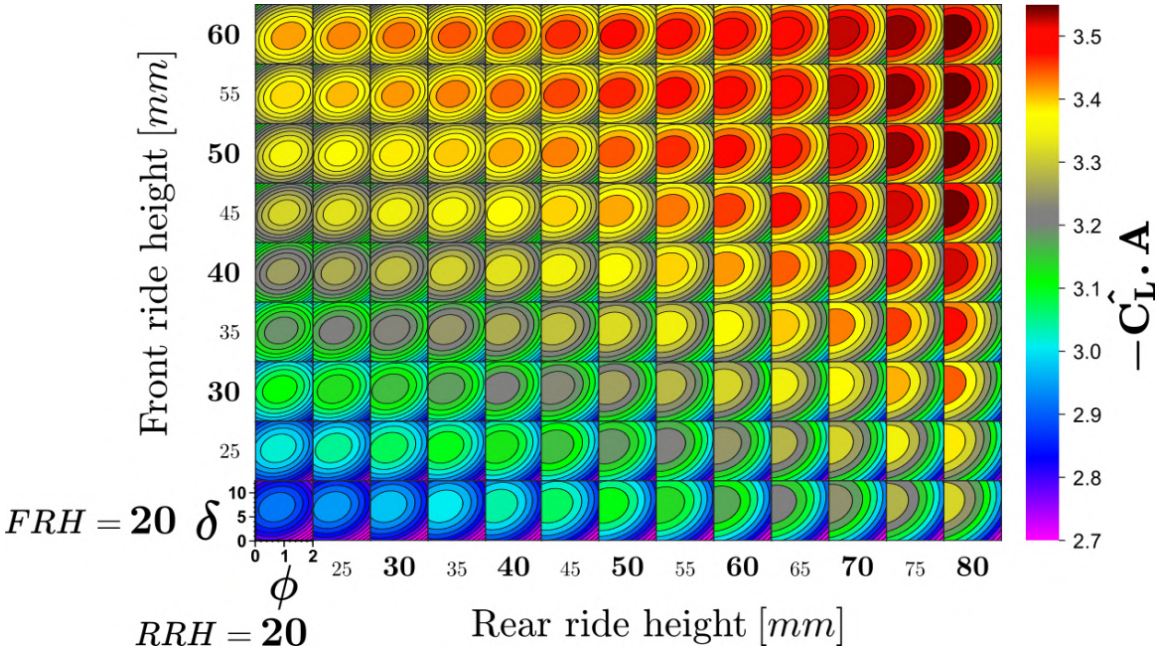

(a) $\psi = 0.0°$

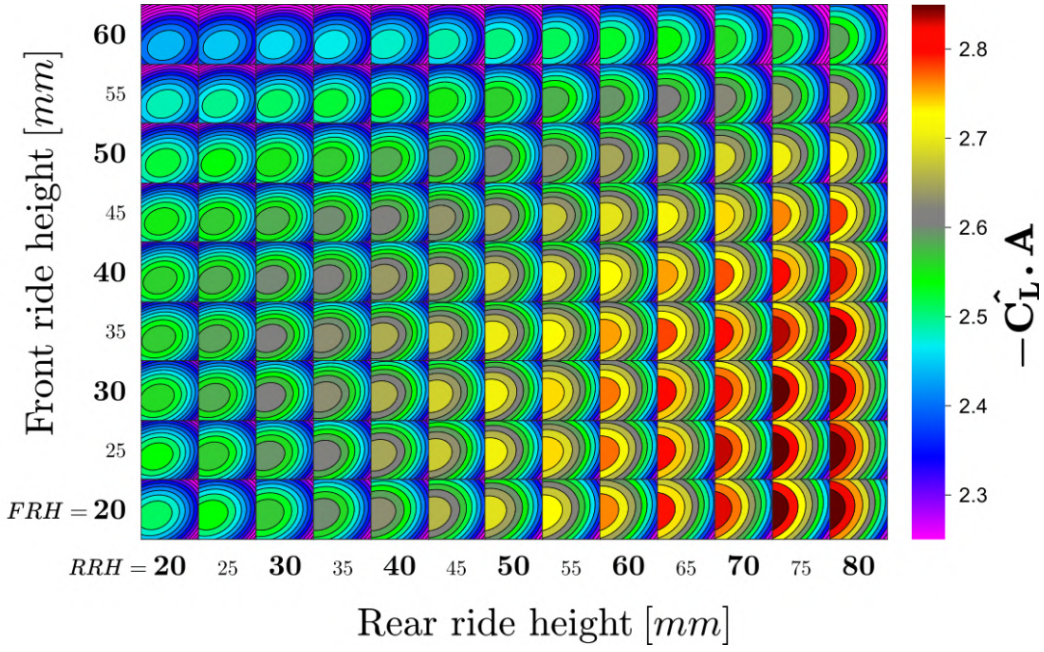

(b) $\psi = 15.0°$

Figure 5.3: Estimated $-C_L.A$ for different values of yaw angle

Chapter 6

On-track Validation

Aerodynamic validation is a rather unexplored field in FST Lisboa team in the past, and this part of the work is aimed to start that process and try to find some correlation between on-track testing and CFD results. My colleague *Jaime Pacheco* is currently correlating CFD to wind tunnel [41] and together with this on-track testing, it promotes aerodynamic validation in both worlds for the future. As these tests are unprecedented within the team and with the limited tools and conditions available, the focus will be on trends rather than absolute values to estimate the relative difference between both worlds.

Throughout this Chapter, the on-track tests will be addressed, starting with the description of each test, followed by the post-processing of the data gathered and finalized with the results obtained.

6.1 Testing Setup

To estimate the car's aerodynamic performance on track, two distinct tests were set: a constant speed test executed to obtain the downforce and a coast down test to estimate the drag force.

The tests took place at Military and Technical Training Center of the Air Force, ("*Centro de Formação Militar e Técnica da Força Aérea, CFMTFA*"), previously known as Ota Air Base [42]. Ota's Air Base which contains two runways (numbered in Fig. 6.1), where runway number 1 was the one used for these aerodynamic validation tests. The runway with more than two kilometres long provides enough space to drive the car steadily and perform the coast down from a high speed.

Figure 6.1: Military and technical training center of the air force, *Google Maps*

6.1.1 Constant Speed

The first test consists of running at a constant speed and estimating the downforce produced by measuring the suspension deflection. There are several ways to measure the forces on the wheels, including wheel force transducers and load cells in the suspension rods, but, with the material available, it was decided to use the existing linear potentiometers located at each spring on FST10e to measure the spring displacement due to the downforce generated. A steady-state is a necessary condition for this test as any lateral or longitudinal acceleration also impact suspension travel ence the constant speed. Knowing the springs stiffnesses and the corresponding displacement, it is possible to determine the vertical load on each wheel by applying Hooke's law. The current speed should also be measured to be able to calculate $C_L.A$.

Summarizing the constant speed test, the essential quantities to complete this test are total downforce produced, air speed to calculate $C_L.A$ by applying $Downforce/q$ and dynamic ride height to get information about the car's attitude. The instrumentation used will be described in Sec. 6.1.3.

6.1.2 Coast Down

The most common way to estimate the drag force is by conducting a coast down test, which consists in accelerating the car up to a certain speed and then coasting (stopping without using any power or brakes) allowing the car to slow down rolling to a stop. The resistant force responsible for decelerating the car is then determined from Newton's second law where it is possible to isolate the part corresponding to the aerodynamic drag.

Intending to express the vehicle motion in a simple equation, some simplifications must be assumed. It is considered that the change in the loaded radius of the tyres is negligible and therefore the radius r_d is assumed to be constant throughout the coast down as there are no moments applied by the motor or braking. The estimation of the parameter r_w will be further described in Sec. 6.1.2.

$$-a = d = \left(R_r + R_g + R_a + R_f\right)/m_{ap}\,, \tag{6.1}$$

where the force during coast down can be broken down into several resistance forces components. Variable d represents the deceleration or negative acceleration during coast down, R_r, R_g and R_a are the rolling, grade and the air resistance, respectively, and R_f is the resistance caused by the drivetrain friction. The full deduction to this and the following equations is explained in full extent in [43] and only some relevant and suitable steps are shown for brevity.

The mass m_{ap} is the apparent mass of the vehicle, since there is an additional component to the kinetic energy from the rotating parts of the wheels. Apparent mass can be expressed as

$$m_{ap} = m_t\left(1 + \frac{I_w}{{r_w}^2}\right)\,, \tag{6.2}$$

as the car experiences a larger mass than the mass in translation motion m_t, due to the extra component associated with rotation relating moment of inertia I_w of every rotating part of the wheel and the loaded

radius r_w.

Assuming a constant C_D independent on the Reynolds number, the air resistance force related to the drag coefficient, R_a by

$$R_a = \frac{1}{2}\rho C_D A(v+w)^2\,, \tag{6.3}$$

where, A represents the frontal area, v the car speed and w the wind speed. From Eq. (6.3), it is possible to confirm that the drag force depends on the air speed and not solely on the vehicle speed, so the wind should be taken into account for this study. With some manipulation and expanding the remaining resistance and friction forces, it is possible to get a parabolic equation as a function of air speed,

$$-a = C_0 + C_1 v + C_2 v^2\,, \tag{6.4}$$

where the constant terms are

$$\begin{aligned} C_0 &= \left[m_t g\,(f_0\cos\alpha + \sin\alpha) + \frac{1}{2}\rho C_D A w^2 + R_{f0}\right]/m_{ap}\,,\\ C_1 &= \left(m_t g f_1\cos\alpha + \frac{1}{2}\rho C_D A w + R_{f1}\right)/m_{ap}\,,\\ C_2 &= \left(\frac{1}{2}\rho C_D A\right)/m_{ap}\,, \end{aligned} \tag{6.5}$$

with g being the gravitational acceleration, f_0 and f_1 are two terms of a linear function between rolling resistance and speed, a constant and the linear term respectively, α is the longitudinal slope of the road, R_{f0} and R_{f1} are a constant and linear term but this time with respect to drivetrain friction losses, once again simplifying as a linear function [43].

As such, to estimate the drag coefficient of a car, it is necessary to understand the relation between acceleration and speed during coast down, obtain a quadratic function that better fits that behaviour and from the second order term C_2, it is possible to estimate C_D. An example of this regression of acceleration on velocity is shown in Fig. 6.2.

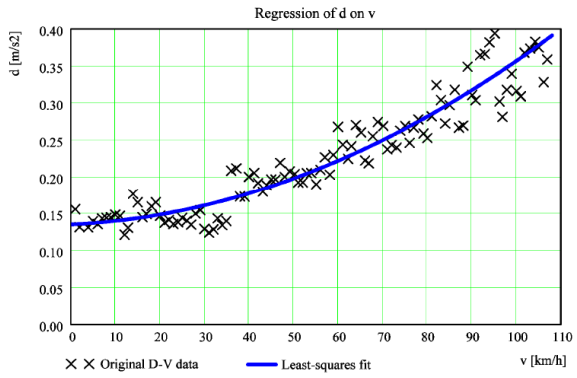

Figure 6.2: Least-squares approximation of experimental data (107 V-D points): $d(v) = 0.135 + 0.00104v + 0.00025v^2$ $(C_D = 0.342)$ [43]

Outlining the coast down test, the necessary measurements are air speed and car acceleration to

estimate drag coefficient from the parabolic regression term with $C_D.A = 2C_2 m_{ap}/\rho$. Additionally, car attitude during the test is once again required and will be addressed in Sec. 6.2.

6.1.3 Instrumentation

To measure all the required variables during the test, several sensors were used that will be briefly outlined next.

Acceleration

To record acceleration during test, it was used the Attitude and Heading Reference System(AHRS), whose purpose is to provide information about the three axes for multiple variables that include roll pitch and yaw angles. In the FST10e, the AHRS is positioned close to the CG to measure the most representative state of the car using the sensor *MTi 670-series* from *Xsens* [44]. This sensor, shown in Fig. 6.3, includes a gyroscope, accelerometer and magnetometer (all 3-axis) but, in this work, only the accelerometer was used to measure acceleration throughout the test. The standard full range of the accelerometer is *10g* that is more than enough for this application.

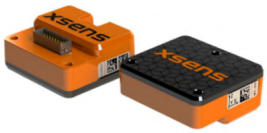

Figure 6.3: Xsens MTi 600-series [44]

Velocity

The AHRS box containing this XSens sensor also includes an antenna with GPS but, unfortunately, it was not operational at the time of testing to measure velocities at the same time. There was no opportunity either to install a pitot tube to measure air speed that would assist in better accuracy. The alternative used was to take advantage of the velocity estimator output from the control algorithm. There is a device located inside the left diffuser that is responsible for the live data processing, called ETAS ES910, shown in Fig. 6.4. With inputs from a variety of sensors placed all over the car, it is possible to estimate all sorts of unknown variables by using an Extended Kalman Filter used by FST team [45] that includes the longitudinal velocity of the car. Together with sensors, this estimated state is then used to implement torque vectoring, traction control and yaw rate controller for example, with all this being processed in ETAS. This estimated velocity was the one used to indicate the velocity of the car over the test.

Potentiometers

A linear potentiometer was used for measuring the suspension positioning. Each wheel suspension includes one of these sensors, positioned close to the spring and damper assembly, as shown in Fig.

Figure 6.4: ETAS ES910 [46]

6.5(b) for the rear suspension case. This sensor is part of the *ELPM Series* with 75 millimetre range from the brand *Variohm* [47] which has motorsports application and shown more clearly in Fig. 6.5(a).

By analysing data from previous tests, it was noticed that the sampling frequency of these sensors was around $10Hz$, resulting in variations up to 3-4 millimetres from two consecutive measurements. As these sensors are capable of a higher frequency of measurement, the sampling frequency was adjusted to $1000Hz$ for a more accurate measurements. Such high frequency might induce some noise to the data but it is easy to filter it afterwards if necessary.

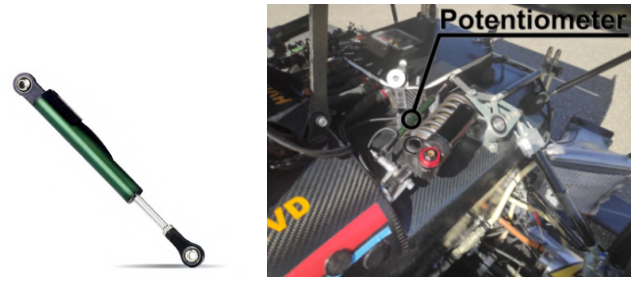

(a) ELPM linear position sensor [47]

(b) Installation in the rear left suspension

Figure 6.5: Linear potentiometer

Additional Instrumentation

Some additional sensors were used, not directly to quantify something but to verify if everything was working as expected. These sensors were located on the pedals and steering rack. Additional linear potentiometers on the brake and throttle pedal allowed for confirmation if there was no applied force to the pedals during coast down. The steering column contains a rotary sensor that gave information to check if the car was not steered during runs and to identify the turn around between runs.

6.1.4 Testing Procedure

To make better use of a testing day as they are expensive, limited and very exhausting, the FST team follows a procedure to provide orientation, organization and logistics of a testing plan.

Before testing, a plan was outlined for the testing day together with the responsible and additional tasks were added to make use of the remaining time at the track including flow vis and wool tuft validation for the aerodynamic department. It was also handled the logistics of the day by assigning a role to each of the 12 people that would go to the test and others responsible for vehicle preparation before and check it after the test.

During the day of testing, the vehicle and material for the day were already prepared but some measurements had to be made before leaving the university. The battery and wings were mounted and with the driver sitting in the car, the vehicle was put on top of four weight scales, one in each corner/wheel, to measure the corner weights. Camber angle was also measured of all 4 wheels using an inclinometer.

At the test site, all the material was unloaded and organized to be easily accessible, some tables and a tent were mounted to check if everything is working as intended by live telemetry. After some pre-test mechanical checks, cones were positioned along the runway to assist the driver by having some visual references on where to accelerate and to start the coast down in both directions, to make sure it is repeated at the same location. A few iterations were run to ensure there was enough distance to cover roughly 10 seconds of constant speed and coast down in both ways. Power was limited to maximize the battery usage as this test is not focused on accelerating rapidly and the motor speed was also limited to 17.000 RPM. This speed is high enough to cause a considerable suspension displacement from downforce but not excessive to run out of space during the steady time.

Right before runs were started, the ride heights were measured together with the tyre pressure on all wheels. The first configuration was a medium distance of ride heights as the car usually runs.

The first two configurations of ride height were done in the morning, using all of the State of Charge (SoC) of the battery. The last setup was then tested later in the afternoon, so the wind influence could have been different associated with the different times of the day.

6.2 Data Processing

Having collected all the raw data during the test runs, the next step is to process it to estimate the desired quantities.

6.2.1 Loaded Tyre Radius

Since there is no possibility to measure the ride height directly, an estimation route was taken to calculate the dynamic ride height. It is relatively easy to convert the suspension travel to wheel travel but the largest obstacle for ride height estimation is that the tyres deformation under vertical load can not be neglected.

The FST10e tyres are *Continental C19*, which is a Formula Student type tyre with approximately 19" diameter. The documentation of this tyre features the loaded radius behaviour as function of the vertical load applied for 3 tyre pressures (IP-Inflation Pressure) and 3 different camber angles (IA - Inclination angle), as shown in Fig. 6.6.

The tyre pressure during the test was $70kPa$ on all wheels which is not present in the documentation. To solve this problem, it was taken advantage of the software *WebPlotDigitizer* [49], in which data points were extracted from the Fig. 6.6 with approximately 70 data points for each of the 9 curves. From this data, it was then found the best adjusting polynomial regression (which revealed to be of second

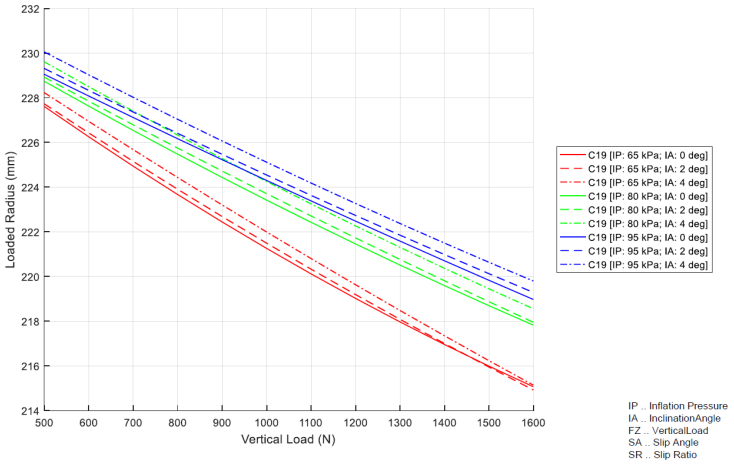

Figure 6.6: Tyre radius as function of vertical load [48]

degree) for each of the cases. Data was then interpolated to obtain the value corresponding to the intended $70kPa$ pressure. The obtained functions to the testing pressure are visible in Fig. 6.7(a). To estimate the loaded tyre radius during the test, two inputs are needed to the tyre model (Fig. 6.7(b)) that interpolates between the curves for the camber angle and vertical load. .

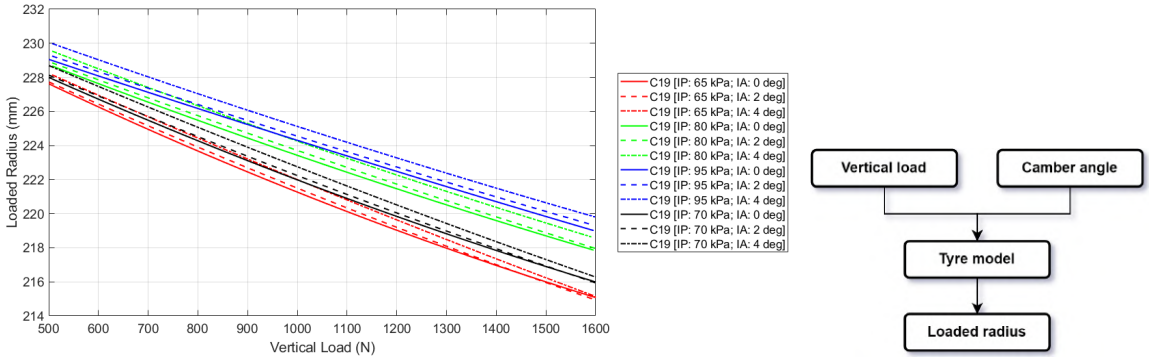

(a) Calculated loaded radius vs vertical load for $70kPa$ tyre pressure

(b) Tyre model diagram

Figure 6.7: Tyre data handling

6.2.2 Dynamic Ride Height

From the potentiometer measurements, many dependant variables can be estimated through various methods, as schematically shown in Fig. 6.8.

These are applied to each wheel individually and front and rear wheels are differentiated because the suspension geometry is distinct. The first step is to convert the digital signal of the potentiometers into its position between 0-75 millimetres. This allows to understand the suspension position at each reading. Using a suspension kinematics simulation, also provided by FST Lisboa (similar to steering one mentioned in Sec. 2.1.3) a wheel travel distance is imposed from -50 to +50 millimetres from the default static position with a step of 0.1 millimetres, in which the behaviour of all suspension geometry positioning is recorded. Although these results were integrated in the workflow with 1000 singular points and used by a lookup table and interpolation between data points, it is shown graphically in App. B.5 for

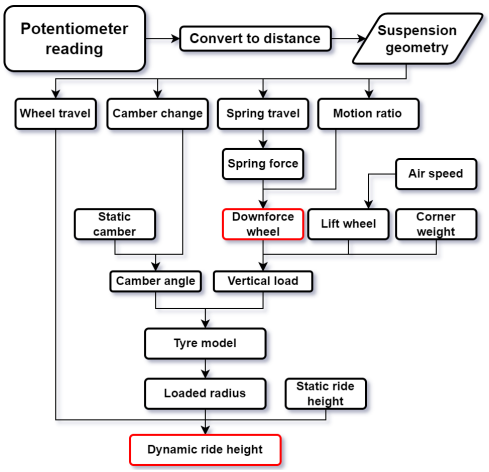

Figure 6.8: Workflow for potentiometer data-processing

brevity and overall understanding of how suspension characteristics change.

For the dependant variable potentiometer positioning, the independent variables include: wheel travel, spring travel, change in camber angle and current motion ratio. Having found this, it is possible to compute the current wheel camber by adding camber change to the static value read before. Spring force can be calculated by applying Hooke's Law with the corresponding spring stiffness k and spring displacement Δx_{spring},

$$F_{spring} = k_{spring} \times \Delta x_{spring}\,, \tag{6.6}$$

with $k_{front} = 68[N/mm]$; $k_{rear} = 55.5[N/mm]$. It is also defined a static condition that is determined when the car is stopped right before the test that will be further explained in Sec. 6.3.1. Afterwards, the delta values found are compared to the static ones.

The motion ratio MR quantifies the relation between the wheel and spring displacement,

$$MR = \frac{Wheel\ Displacement}{Spring\ Displacement}\,. \tag{6.7}$$

Although motion ratio does not usually vary much through the entire working range of the suspension, as this data was available it was also included and updated on each reading. As the displacements are different, so are the forces and to find the respective force at the wheel, F_{spring} is multiplied by the motion ratio.

To find the downforce, an additional component is also included due to lift generated by the wheel assembly. As the wheel generates lift (approximately constant on all 4 wheels $C_L.A_{wheel} \approx 0.02$) it has to be discounted on the overall measured force at the wheel expressed by

$$F_{wheel} = F_{spring}.MR - \underbrace{C_L.A_{wheel}\frac{1}{2}\rho {V_{air}}^2}_{\text{Wheel lift force}}\,. \tag{6.8}$$

To estimate the last input needed for the tyre model, the vertical load can be found by adding the

corresponding corner weight that represents a large part of the vertical load,

$$Vertical\ Load = F_{wheel} + \text{Corner Mass}.g\,. \tag{6.9}$$

Finally, all the information needed to estimate the dynamic ride height at each time is known and, taking as example the front ride height, FRH is determined by the mean between left and right ride height changes, since it is measured at the centre of the car,

$$FRH = FRH_{static} + \frac{(\Delta x_{FL} + \Delta r_{FL}) + (\Delta x_{FR} + \Delta r_{FR})}{2}\,, \tag{6.10}$$

where the subscripts FL and FR refer to the front left and front right wheel respectively, Δx is the wheel travel change and Δr is the loaded radius change.

6.2.3 Static Ride Height

To change the static ride height during testing, shims were added and removed to the suspension pushrod. The first configuration ran was the high ride height, followed by the low and then later in the afternoon a medium configuration was defined, as shown in Fig. 6.9.

(a) Low (b) Medium (c) High

Figure 6.9: Front ride height configurations with different shim size

The static ride height is measured with a jig that essentially unscrews until it hits both the car and ground at the same time. With this length set, it is then measured by a calliper to define the static ride height. However, in the rear axle case, the distance measured is from the floor up to the monocoque , meaning this is not directly the distance defined as RRH in Sec. 2.1.3. By applying trigonometry to the diffuser expansion "triangle" it is possible to obtain the effective rear ride height by

$$RRH_{static} = RRH_{measured} - \frac{\tan(\alpha) \times d}{\cos(\arctan(\frac{RRH_{measured} - FRH_{static}}{l}) - \arcsin(\frac{\tan(\alpha) \times d}{\sqrt{l^2 + (\tan(\alpha) \times d)^2}}))}\,, \tag{6.11}$$

where α is the expansion angle ($\alpha = 3°$, coincident with monocoque surface), l is the wheelbase ($l = 1540$) and d is the distance between the start of diffuser angle and rear axle ($d = 741$).

During the testing day, the measurement jig was lost and it was only possible to accurately measure the last configuration with it. The remaining conditions were measured roughly to compare with the estimated values to verify if they were plausible. Tab. 6.1 summarizes the different shim sizes used for each configuration to calculate the change in pushrod length and to estimate the remaining ride heights. The default suspension corresponds to $FRH = RRH = 50mm$, used in for the kinematic suspension studies. As the effective pushrod length changes with shims, this small change in the suspension geometry was also taken into account.

Table 6.1: Shims size

Configuration	Front $[mm]$	Rear $[mm]$
Default suspension	10	14
Low ride height	8	13
Medium ride height	12	20
High ride height	16	26

To convert the shims size into ride height, it is necessary to understand the pushrod behaviour of the suspension kinematics as previously only the spring to wheel travel was known. A simplified diagram with the pushrod, bellcrank representation and spring is shown in Fig. 6.10, with the distances and angles described in Tab. 6.2.

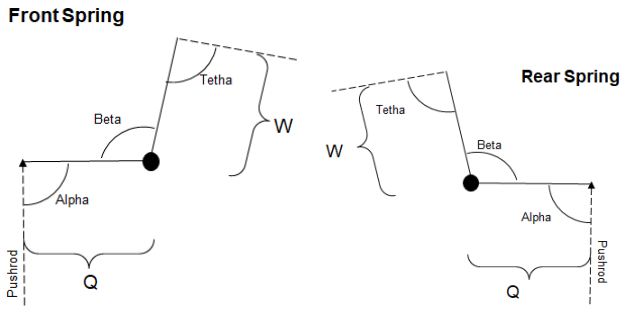

(a) Front suspension (b) Rear suspension

Figure 6.10: Suspension diagram by FST Lisboa vehicle dynamics department

Table 6.2: Pushrod change with shim

Suspension	α [°]	β [°]	θ [°]	Q $[mm]$	W $[mm]$
Front	90	103.9	98.2	55	69.7
Rear	90	105.4	90.0	55	67.0

With this information, it is possible to calculate the relation between spring and pushrod displacements (referred to as $MR_{spring-push}$),

$$MR_{spring-push} = \frac{W \times \sin(\theta)}{Q}, \tag{6.12}$$

The change in shim size is converted to a spring delta, which can be then translated into wheel travel and subsequently to the missing ride height. This approach revealed to be successful as the estimated

values matched the rough measurements on track for the first two conditions. The three static ride height configurations tested are displayed in Tab. 6.3.

Table 6.3: Static ride height configurations

Configuration	Front $[mm]$	Rear $[mm]$
Low ride height	40.1	31.6
Medium ride height	46.4	43.2
High ride height	52.7	53.3

6.2.4 Atmospheric Conditions

The test took place on a sunny but also a bit windy day. It is important to determine the atmospheric conditions because they influence the results obtained.

Air Density

Although there were no reading of the air density directly, it can be estimated by using ideal gas law $p = \rho RT$.

By looking at weather conditions around Lisbon it was possible to approximate the air temperature of the day to a value around $T = 24°C$. Using Standard Sea Level (SSL) pressure of $P = 101.325kPa$ and with gas constant of $R = 287.05J/kgK$ the air density for the test was found to be $\rho = 1.1945kg/m^3$.

Wind

The aerodynamic forces the car undergoes during the test do not depend on the car's velocity but rather on relative airspeed that is the sum of the two. As wind directly affects the airspeed, it is in the best interest to measure or at least have an estimate of it. Ideally, a Pitot tube should be used to read the air velocity but unfortunately, there was no possibility to include one. It was attempted to allocate the testing to a low wind day, but the weather forecast is not reliable for long periods of time necessary to plan everything and it revealed to be quite windy during testing day. We paid a visit to the weather centre at the Air Base but the data collected by them could not be shared with us but revealed the wind direction was relatively constant throughout the day, coming from the North meaning it was aligned with the testing runway. Figure 6.11 shows a picture taken during the test with the car standing still before one of the runs, where it is possible to see the wool tufts at the rear wing endplate all turned backwards due to the considerable wind. The wind component revealed to be a massive adversity for the test results and the greatest source of error for the on track testing.

The first approach to mitigate this problem was to average the runs both ways, as one had tailwind and the other had headwind, to cancel the wind influence. When looking at the data, it was immediately realized that the dynamic attitudes varied significantly from one way to another due to the increasing aerodynamic load and this idea was discarded.

Figure 6.11: Wool tufts during testing day

The last approach used to try and solve wind speed unknown was to assume the same $C_L.A$ between runs with similar attitude. Two configurations ended up with approximately the same dynamic ride height, each in one direction. It was then assumed that the $C_L.A$ would be the same for the two runs, finding the wind speed at which this would be verified. From this approach the wind speed is about $19[km/h]$ used for the upcoming results.

6.3 Experimental Results

Moving onto the data and results obtained from the on-track testing, firstly an overview of a run and the data selection is explained. In Fig. 6.12 it is displayed an example of a round-trip for the first setup, which contains 2 of the 6 runs performed for each configuration with the intervals used to obtain the desired coefficients for each test. The complete data for some example runs is shown in App. B for further analysis if desired.

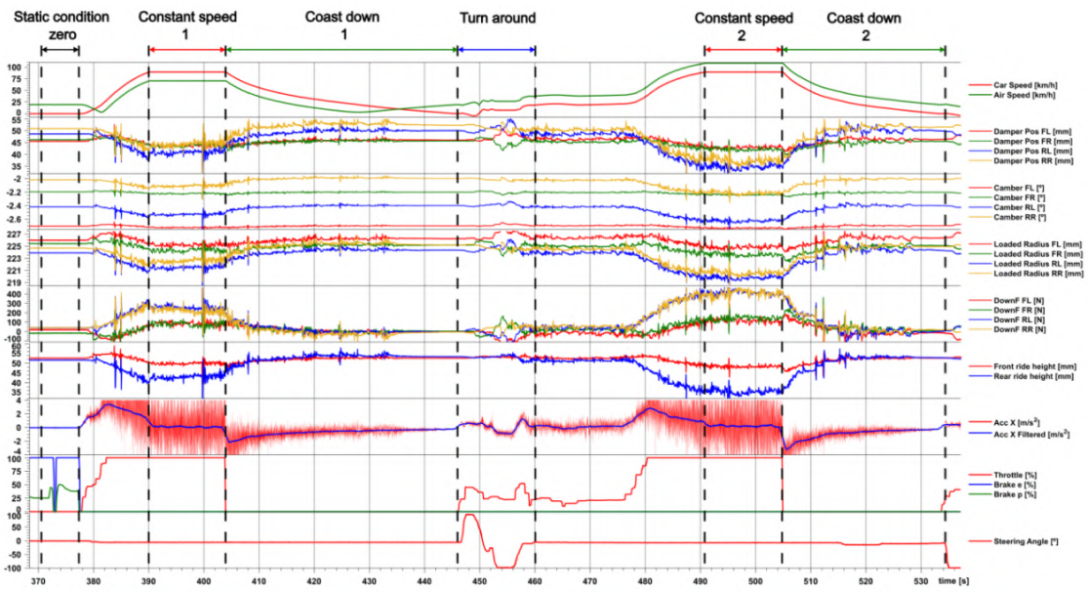

Figure 6.12: Overview of a testing run

On the left hand side, it is represented the reference static condition that establishes the car stopped, in which variables are calculated relative to this position. The car is then accelerated up to the intended speed and the first constant speed test run is executed for more than 10 seconds (confirmed on the x-axis) where the data is averaged over this interval. Right after, it is performed the coast down up until

car speed reaches zero. Acceleration then goes down to a negative value as the car is decelerating.

The following step is to turn around the car, which is visible in the steering input. After some time, the limit speed is reached again (17000 RPM from the motors) and the second run is executed, followed by the coast down once again returning back to the begging where this process is repeated two more times for each setup, totalling 6 runs.

The difference in downforce and car attitude between both consecutive runs is noticeable and significant and, for this reason, it was decided to isolate each direction and compare 6 different configurations (from 3 setups). Together with the car speed, it is also shown the estimated air speed that is the motivation for this variation. In the test represented by number 1 there is a tailwind component in effect, resulting in smaller airspeed than the car's speed while in run number 2, air speed surpasses car speed (that remains constant in both directions). One might find it strange that during coast down 1, air exceeds car speed at some point, but this derives from the fact air speed is shown an absolute value and in that instance tailwind is larger than the car's speed, meaning that in reality from the car's reference frame, the air is coming from behind.

6.3.1 Constant Speed

Having implemented the plan of action explained previously by processing all the data, the results from the track testing were found. The final experimental results of the constant speed tests are summarized in Tab. B.1 and some data over run examples are displayed in Sec. B.4 to depict the difference/variance when repeating tests and comparing between different attitudes.

Previously, it was mentioned that two different runs were assumed to have the same downforce coefficient to determine the wind speed. These runs are numbered as 3 and 4, in which the FRH has changed 3.3 mm and RRH only 0.3 mm. This approach was found to be the best case scenario in this work to obtain an estimative for the wind speed. It was assigned a number for each attitude, but the numeration does not match the test sequence. This order was chosen to separate the wind direction runs. From 1-3, the test has tailwind and 4-6 headwind. This mixing could mislead to wrong conclusions coming from the simplistic way that the wind problem was solved, besides the fact wind is gusty inducing even more error from this component.

The results are illustrated in Fig. 6.13(a) including uncertainty bars. As the wind speed inaccuracy exceeds greatly all other sources of error, the experimental uncertainty was estimated by the change in the downforce coefficient with and without a wind component, being approximately 1.0 change in $C_L.A$. There is a missing CFD data point in attitude 5 since the geometry intersected the ground. During this run, the rear diffuser was a bit scrapped underneath confirming this theory that the car was too low.

Overall, what stands out is the significant difference between experimental and numerical results across all attitudes. The gap is smaller in the first two attitudes but is still significant. The aim of this aerodynamic validation was to evaluate the trends across different conditions of the car and not focus on absolute values or differences between results. Having this in mind, the uncertainty magnitudes have proven to be massive, meaning that even if some trend seems to be captured it may be misleading

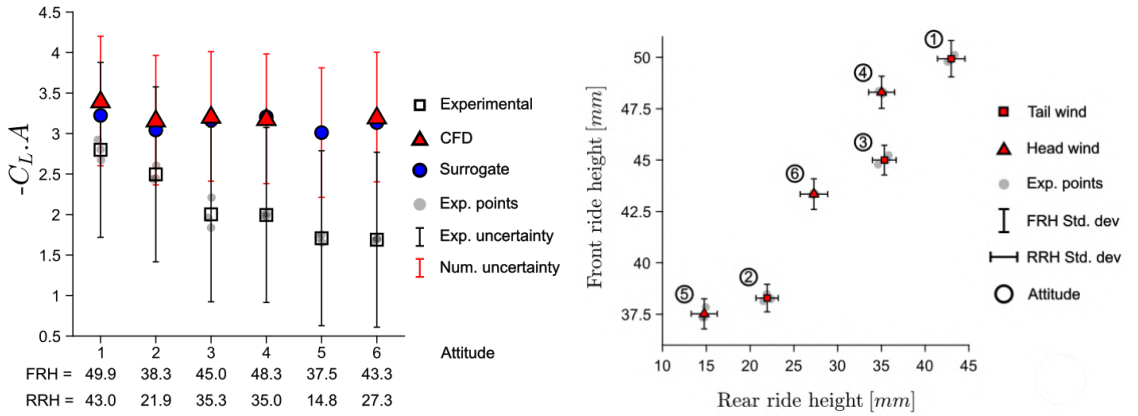

(a) $-C_L.A$ results

(b) Ride heights and respective standard deviation

Figure 6.13: Constant speed test results

because the trend may not be verified with other values within the standard deviation range. As all the data is averaged across the time interval with constant speed, there are some variations over this time, mainly related to the car attitude due to bumps or irregularities on the runway. To better showcase the attitude change over this interval, Fig. 6.13(b) displays the averaged standard deviation of ride height for each case. The red marker represents the averaged condition between the 3 runs (each one showcased below in grey). The wind direction is also separated by marker shape (square vs triangle) enabling the perception of the difference between consecutive runs with the same setup. From the figure, none of the ride heights presents a significant variation, although RRH features higher values with a maximum value of around 1.6 millimetres.

Analysing the first 3 attitudes (tailwind conditions), the decreasing trend and magnitude change between 1 and 2 looks similar in CFD and on-track results but it does not apply to attitude 3, diverging from one other. Looking at the headwind conditions, a similar behaviour occurs, with the decreasing tendency from 4 to 5 to resemble the track results (even though with a greater change) but then attitude 6 downforce remains constant, while CFD results points to an increased value. Attitudes 3 and 6 correspond to the runs executed at the end of the day after a few hours have passed since the other scenarios and may have been submitted to different conditions (air temperature, wind gusts for example). This may be the cause of the results deviation from the expected trend, unlike the remaining cases.

6.3.2 Coast Down

After processing all the data from the coast down it was possible to understand how the car behaved during this test. An example of a coast down is shown in Fig. 6.14, which includes speed, downforce, ride heights and longitudinal acceleration over the coast down time. From this figure, some perturbations are noticeable causing some oscillations in the attitude, the most intense being around 511 and 512 second time mark caused by some bumps on the track. Over this test, both ride heights vary substantially from the beginning to the end, due to the loss of aerodynamic load compressing the suspension.

Taking the acceleration and plotting it against the air speed it is possible to obtain the quadratic regression needed to find the drag coefficient. An example of this data is shown in Fig. 6.15, where the

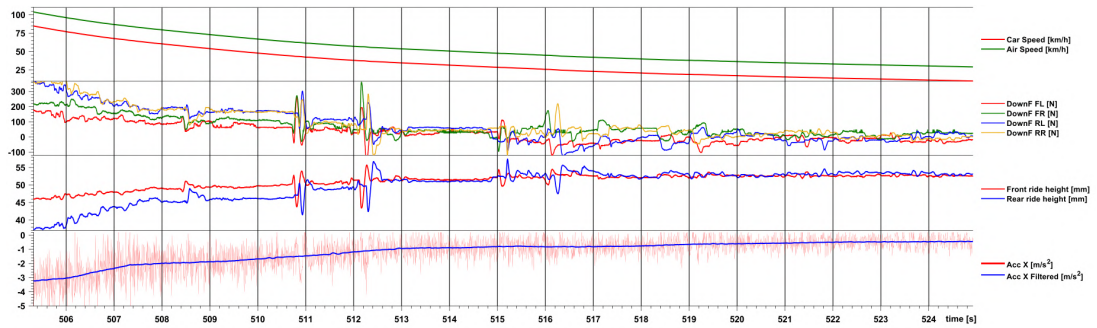

Figure 6.14: Overview of coast down test data

raw data is shown against the parabolic curve with the best fit. This raw data is already filtered due to the high level of noise coming from the accelerometer, visible in the last variable shown in Fig. 6.14.

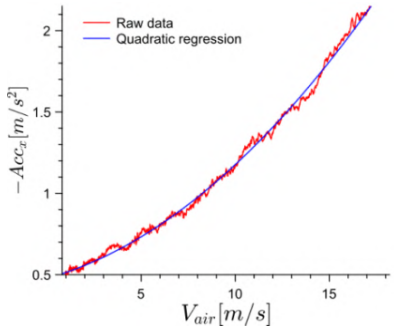

Figure 6.15: Acceleration vs velocity from coast down test

The data from the coast down was treated in multiple ways to extract the best potential from it. It was attempted to split the entire coast down range into 3 sections, and analyse each of them individually as the attitudes vary considerably. This approach did not work as intended as it resulted in a greater variation of the drag coefficient between sections, even reaching negative values of $C_D.A$ in some particular cases. The other approach was to trim the data to exclude the first few seconds and the last part of coast down. When the driver released the throttle, a transient state with the car pitching nose down occurs, so the processed data was trimmed out to eliminate this influence. During the latest section of deceleration, the linear and constant terms have a greater impact and, since the goal is to estimate the second order term, it was found pertinent to exclude this latter part as it would induce more errors in the drag coefficient (excluded values below 10 km/h) . This trim approach was found to be the best suited for this case and it was taken for the coast down data.

By applying the same methodology to the 18 runs executed, resulting in the data described in Tab. B.3 which indicates the averaged ride height in which the coast down was executed and the obtained drag coefficient putting into practice the procedure explained before. Some additional measurements and unknowns are shown in App. B.2, and a few example of the data throughout the run is displayed in App. B.4. The data presents a high level of variation between the same setup runs. The third run of configuration 6 was aborted due to electrical problems during coast down.

The experimental data is graphically presented in Fig. 6.16(a) including the results from the surrogate model in the same attitude, uncertainty and standard deviation. The experimental bars represent the

$C_D.A$ standard deviation from the 3 sample points ran. The numerical uncertainty represented is the one estimated in Sec. 2.4 regarding the mesh convergence. Interestingly, there is one experimental point that falls below the surrogate one (attitude 3) which goes against the remaining trend. Usually, it is expected to underestimate the drag due to all the simplifications made in the geometry and conditions of the simulations. Once again, a major source of error may come from the air speed estimation just like in the case of the constant speed test that greatly influences the outcome of these results. One should note that conclusions must not be drawn between attitudes 1-3 and 4-6 as they represent opposite wind directions. It is possible to see the high experimental standard deviation, due to the variation between repeating runs. This means that the repeatability is poor, maybe due to track or weather conditions, for example wind gust present in some runs. Other possible reason for this variation might be the fact that the runway has a sudden inclination, having a longitudinal slope that goes against the assumption made that the track is flat. It was also noticed through all the track data that the forces between right and left wheels always differed from one another a bit. This might be an indicator that the track may have some lateral slope as well, but no other cause was identified for this behaviour.

As stated previously, attitude changes over the course of coast down and Fig. 6.16(b) demonstrates that variation. As the rear springs are softer, one would expect the RRH to change the most and that is what happens. In the headwind cases, both ride heights variations are higher reaching a maximum value of 4 millimetres for the standard deviation.

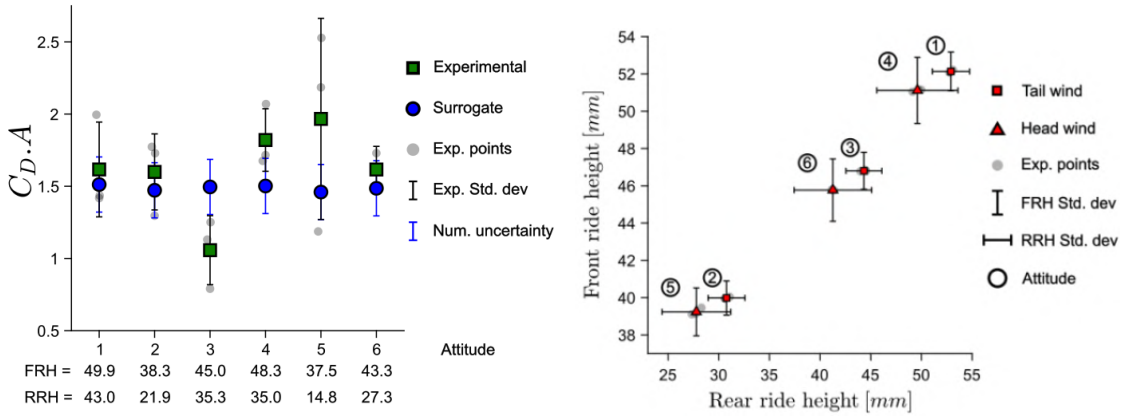

(a) $C_D.A$ results

(b) Ride heights and respective standard deviation

Figure 6.16: Coast down results

Again focusing on the trends instead of quantitative comparisons, it is found rather difficult to get some certain conclusion as there is not a lot of confidence in the values obtained for this test and within the uncertainty bars, trends could reveal to be the opposite as initially thought. It is possible to notice that the change in $C_D.A$ is far greater in experimental results than in numerical. It can be seen that surrogate values barely shift between attitudes. As the CFD results do not differ so much from the surrogate model, it was found pertinent to not run additional simulations to draw the same conclusions as with the surrogate model alone.

Chapter 7

Conclusions

The major objective of this work was to develop a deeper understanding of the aerodynamic behaviour of a race car, in particular for the FST10e prototype. A working envelope was defined and it was studied the response of forces and moments coefficients in all three directions with respect to individual and coupled operating parameters, representative of the car state. During this work, it was possible to notice a change in more than 35% in downforce that confirmed the car behaviour dependence on the attitude and condition proposition for this work.

Five parameters of interest were analysed that determine the car attitude. Roll angle revealed to have a monotonic and rather independent behaviour resulting in 9% change in downforce and a shift of 12% in pressure centre. Ride height individually presented a significant change in all response coefficients. It varied by 10% in $C_D.A$ and 20% in $C_L.A$ between peak values in symmetric conditions, and it was understood that contrary to what was expected, FST10e best working range corresponded to high ride heights. The steering angle together with flow curvature, affects the most the yawing moment of the car due to different incidence angles across the car. Finally, the yaw angle presented the highest sensitivity to side force coefficient and also a considerable change in drag and downforce with 12% and 16% change respectively. It was also noticed that the downforce coefficient was linked between yaw angle and ride height, meaning that the optimal ride height zone changed based on yaw.

7.1 Achievements

The major achievements of the present work were:

1. It was possible to perform **on-track aerodynamic validation** for the first time by executing constant speed and coast down tests. Even if not many absolute conclusions have been drawn it was a step forward in the essential component of aerodynamic validation.
2. a **further understanding** of FST10e was gained, identifying the weaknesses and strengths of its aerodynamic performance, helping in future design processes.
3. with an **aerodynamic map**, it was possible to quickly obtain results for any attitude by using a surrogate model instead of spending many hours for CFD results.

To achieve the findings presented throughout this work, some tools were created:

1. A **parametric CAD** of FST10e prototype sped up the process of changing the car attitude and provide a good surface quality for CFD simulations. In addition to the parameters of interest, adjustability features were also incorporated to change the configuration if needed in the future;
2. a total of 116 **CFD** simulations were performed, focused on corner condition but also included two straight line cases scenarios with a mesh convergence study to estimate numerical error;
3. Several **macros** were created to automate repetitive processes that are time consuming and prone to user input error. The CFD workflow was automated and an Excel tool was made to allocate CFD data into an organized document;
4. An algorithm to produce a polynomial regression **surrogate model**, that finds the best order based on a cross validation leave-one out method;
5. A **dynamic ride height estimator** was developed to determine the car ride height during testing, which also contains a tyre model to estimate its loaded radius.

7.2 Future Work

Among the multiple subjects covered in this work, all of them present a large scope for future development.

Numerical error and uncertainty from CFD results can be reduced to make more founded conclusions. This can be achieved by increasing cell count or even by further exploring the AMR methodology with other refinement criteria or even with other mesh type. This method was only briefly investigated and it has a lot of potential to adapt the mesh to the problem in study. As computational power was limited in this work and these simulations comprise of a complex geometry, they can be further refined while running on faster hardware to decrease its error. Research can also be made by investigating other turbulence models, for example resolving turbulent structures by the means of Detached Eddy Simulation (DES) or even Large Eddy Simulation (LES) that are transient techniques in opposed to averaged solutions present in this work. This approach can provide tools to study the time dependant structures that caused the oscillations seen before but it also requires a high mesh resolution to be resolved.

The working range for the 5 parameters of interest can also be extended to incorporate a wider envelope. This applies mainly to yaw angle ψ, where only positive values were taken into account. These are related to oversteer scenarios but understeer conditions with negative yaw angles should be considered in the future.

There are more complex approaches that can be used to construct the surrogate model and might find a better response, with some examples being KRG and Radial Basis Functions. The surrogate model can be integrated in future vehicle dynamics transient simulators within the team to update the aerodynamic coefficients at each time step.

On-track testing validation is an area of focus that can be greatly exploited. With the possibility to implement further instrumentation on the next prototype, correlation between CFD and reality can be obtained using a quantitative approach estimating the absolute error from CFD.

Bibliography

[1] W. F. Milliken and D. L. Milliken. *Race Car Vehicle Dynamics*. SAE International, 1995. ISBN:978-1560915263.

[2] J. Katz. *Race Car Aerodynamics: Designing for Speed*. Robert Bentley, 2^{nd} edition, 2006. ISBN:978-0837601427.

[3] Formula student, 2022. URL `https://www.imeche.org/events/formula-student`. Online; accessed on March 2022.

[4] Formula student germany disciplines, 2022. URL `https://www.formulastudent.de/about/disciplines/`. Online; accessed on March 2022.

[5] Formula student rules 2022, 2021. URL `https://www.formulastudent.de/fsg/rules/`. Online; accessed on 2021.

[6] What is an aero map?, 2021. URL `https://www.racecar-engineering.com/tech-explained/what-is-an-aero-map/`. Online; accessed on November 2021.

[7] X. Zhang, W. Toet, and J. Zerihan. Ground effect aerodynamics of race cars. *Applied Mechanics Reviews*, 59(1):33–49, 01 2006. doi: 10.1115/1.2110263.

[8] Aerodynamic mapping and analysis, 2021. URL `https://www.totalsimulation.co.uk/aerodynamic-mapping-and-analysis/`. Online; accessed on November 2021.

[9] I. O. for Standardization. *Road vehicles — Vehicle dynamics and road-holding ability — Vocabulary*. International Organization for Standardization, Switzerland, ISO 8855:2011(E) edition, 2011. URL `https://www.iso.org/standard/51180.html`.

[10] M. Guiggiani. *The Science of Vehicle Dynamics*. Springer, 2013. ISBN:978-94-017-8532-7.

[11] A. Newey. *How to build a car*. HarperCollins, 1^{st} edition, 2017. ISBN:9780008196806.

[12] V. de Brederode. *Aerodinâmica Incompressível: Fundamentos*. IST Press, 1^{st} edition, 2014. ISBN:978-989-8481-32-0.

[13] E. Croner, H. Bézard, C. Sicot, and G. Mothay. Aerodynamic characterization of the wake of an isolated rolling wheel. *International Journal of Heat and Fluid Flow*, 43:233–243, 2013. ISSN 0142-727X. doi: https://doi.org/10.1016/j.ijheatfluidflow.2013.04.008.

[14] S. D. I. Software. Simcenter STAR-CCM+ User Guide, version 2020.3. In *Polyhedral Mesher*. Siemens, 2021.

[15] F. Moukalled, L. Mangani, and M. Darwish. *The Finite Volume Method in Computational Fluid Dynamics: An Advanced Introduction with OpenFOAM® and Matlab®*, volume 113. 10 2015. ISBN 978-3-319-16873-9. doi: 10.1007/978-3-319-16874-6.

[16] F. R. Menter. Two-equation eddy-viscosity turbulence models for engineering applications. *AIAA Journal*, 32(8):1598–1605, 1994. doi: 10.2514/3.12149.

[17] V. Venkatakrishan. On the accuracy of limiters and convergence to steady state solutions. In 31^{st} *Aerospace Sciences Meeting*, 1993. doi: 10.2514/6.1993-880.

[18] G. Alfonsi. Reynolds-averaged Navier-Stokes equations for turbulence modeling. *Applied Mechanics Reviews*, 62, 07 2009. doi: 10.1115/1.3124648.

[19] MRF development, 2009. URL `https://openfoamwiki.net/index.php/See_the_MRF_development`. Online; accessed on December 2021.

[20] S. D. I. Software. Simcenter STAR-CCM+ User Guide, version 2020.3. In *Wall Treatment*. Siemens, 2021.

[21] F. Menter, P. Smirnov, T. Liu, and R. Avancha. A one-equation local correlation-based transition model. *Flow, Turbulence and Combustion*, 95:1–37, 07 2015. doi: 10.1007/s10494-015-9622-4.

[22] S. D. I. Software. Simcenter STAR-CCM+ User Guide, version 2020.3. In *Transition*. Siemens, 2021.

[23] B. Çetin, K. G. Güler, and M. H. Aksel. *Heat Exchangers - Design, Experiment and Simulation*. InTech, 2017. doi: http://dx.doi.org/10.5772/66281.

[24] S. D. I. Software. Simcenter STAR-CCM+ User Guide, version 2020.3. In *Adaptive Mesh Refinement*. Siemens, 2021.

[25] W. L. Oberkampf and C. J. Roy. *Verification and Validation in Scientific Computing*. Cambridge University Press, 2010. doi: 10.1017/CBO9780511760396.

[26] B. Cabral and L. C. Leedom. Imaging vector fields using line integral convolution. In *Proceedings of the 20th Annual Conference on Computer Graphics and Interactive Techniques*, SIGGRAPH '93, page 263–270, New York, NY, USA, 1993. Association for Computing Machinery. ISBN 0897916018. doi: 10.1145/166117.166151.

[27] L. Eça. *Aerodinâmica Incompressível: Exercícios*. IST Press, 1^{st} edition, 2015. ISBN:978-989-8481-33-7.

[28] L. Eça and M. Hoekstra. A procedure for the estimation of the numerical uncertainty of cfd calculations based on grid refinement studies. *Journal of Computational Physics*, 262:104–130, 2014. ISSN 0021-9991. doi: 10.1016/j.jcp.2014.01.006.

[29] J. M. Pegrum. Experimental study of the vortex system generated by a Formula 1 front wing. Imperial College London, November 2006. doi: 10.25560/12585.

[30] J. Zerihan and X. Zhang. Aerodynamics of a single element wing in ground effect. *Journal of Aircraft*, 37:1058–1064, 01 2000. doi: 10.2514/2.2711.

[31] A. C. Marta. *Aircraft Optimal Design*, chapter Surrogate Models and Multi-Fidelity. Instituto Superior Técnico, Universidade de Lisboa, 2022.

[32] N. V. Queipo, R. T. Haftka, W. Shyy, T. Goel, R. Vaidyanathan, and P. Kevin Tucker. Surrogate-based analysis and optimization. *Progress in Aerospace Sciences*, 41(1):1–28, 2005. ISSN 0376-0421. doi: 10.1016/j.paerosci.2005.02.001.

[33] B. Tang. Orthogonal array-based latin hypercubes. *Journal of the American Statistical Association*, 88(424):1392–1397, 1993. doi: 10.1080/01621459.1993.10476423.

[34] A. Hedayat, N. Sloane, and J. Stufken. Orthogonal arrays: Theory and applications. *Technometrics*, 42, 11 2000. doi: 10.2307/1270971.

[35] M. Mckay, R. Beckman, and W. Conover. A comparison of three methods for selecting vales of input variables in the analysis of output from a computer code. *Technometrics*, 21:239–245, 05 1979. doi: 10.1080/00401706.1979.10489755.

[36] D. B. McDonald, W. J. Grantham, W. L. Tabor, and M. J. Murphy. Global and local optimization using radial basis function response surface models. *Applied Mathematical Modelling*, 31(10): 2095–2110, 2007. ISSN 0307-904X. doi: 10.1016/j.apm.2006.08.008.

[37] N. Draper and H. Smith. *Applied Regression Analysis*. Wiley Series in Probability and Statistics. Wiley, 1998. ISBN 9780471170822.

[38] J. Sacks, W. J. Welch, T. J. Mitchell, and H. P. Wynn. Design and analysis of computer experiments. *Statistical Science*, 4(4):409–423, 1989. ISSN 08834237.

[39] N. Chlis. *Comparison of Statistical Methods for Genomic Signature Extraction*. PhD thesis, Technical University of Crete, 10 2013.

[40] A. Forrester, A. Sobester, and A. Keane. *Engineering Design Via Surrogate Modelling: A Practical Guide*. John Wiley & Sons Ltd, 07 2008. ISBN 978-0-470-06068-1. doi: 10.1002/9780470770801.

[41] J. R. M. Pacheco. Wind tunnel testing of a complete formula student vehicle. Master's thesis, Instituto Superior Técnico, Universidade de Lisboa, 2022.

[42] Centro de Formação Militar e Técnica da Força Aérea. URL `https://www.emfa.pt/unidade-52-centro-de-formacao-militar-e-tecnica-da-forca-aerea`. Online; accessed on February 2022.

[43] I. Preda, D. Covaciu, and G. Ciolan. Coast down test – theoretical and experimental approach. In *CONAT 2010 - International Automotive Congress*, 10 2010. doi: 10.13140/RG.2.1.4048.5925.

[44] *MTi 600-series Data Sheet*. Xsens Technologies B.V., Document MT1603P edition, 9 2019. Rev. B.

[45] N. A. de Almeida Salgueiro. Torque vectoring control of an electric vehicle with in-wheel motors. Master's thesis, Instituto Superior Técnico, Universidade de Lisboa, 2021.

[46] ES910 – Prototyping and Interface Module. URL `https://www.etas.com/en/products/es910_rapid_prototyping_module.php`. Online; accessed on March 2022.

[47] *Linear Position Sensor for Motorsports - ELPM Series*. Variohm Eurosensor, 2021.

[48] *Continental Formula Student Tire - Competition Tire 2019 (C19) Documentation*. Continental, 4 2019.

[49] A. Rohatgi. Webplotdigitizer: Version 4.5, 2021. URL `https://automeris.io/WebPlotDigitizer`.

Appendix A

Surrogate Model Data

A.1 Data Points

Table A.1: Data Surrogate

ID	$\mathbf{x}$					$\mathbf{y}$					
	$\mathbf{FRH}$ $[mm]$	$\mathbf{RRH}$ $[mm]$	ψ [°]	ϕ [°]	δ [°]	$\mathbf{C_D.A}$	$\mathbf{C_Y.A}$	$\mathbf{-C_L.A}$	**Out** [%]	**Front** [%]	$\mathbf{C_{Mz}.A.b}$
12	40.0	40.0	0.0	0.0	0.0	1.5097	0.000	3.2029	50.00	30.91	0.000
13	40.0	50.0	0.0	0.0	0.0	1.4604	0.000	3.0300	50.00	28.12	0.000
14	40.0	60.0	0.0	0.0	0.0	1.4670	0.000	3.2348	50.00	30.58	0.000
15	40.0	30.0	0.0	0.0	0.0	1.5013	0.000	3.2641	50.00	28.98	0.000
16	40.0	20.0	0.0	0.0	0.0	1.4571	0.000	3.0682	50.00	28.15	0.000
17	30.0	40.0	0.0	0.0	0.0	1.4478	0.000	2.9711	50.00	26.15	0.000
18	20.0	40.0	0.0	0.0	0.0	1.4377	0.000	3.0212	50.00	31.09	0.000
19	50.0	40.0	0.0	0.0	0.0	1.4825	0.000	3.1524	50.00	29.65	0.000
20	40.0	70.0	0.0	0.0	0.0	1.4807	0.000	3.2098	50.00	32.89	0.000
21	40.0	40.0	0.0	0.5	0.0	1.4988	0.003	3.1729	50.05	30.30	0.023
22	40.0	40.0	0.0	1.0	0.0	1.5011	0.018	3.0284	49.67	26.39	0.015
23	40.0	40.0	0.0	1.5	0.0	1.4735	0.038	3.0074	49.32	26.80	0.020
24	40.0	40.0	0.0	2.0	0.0	1.4536	0.051	2.9145	49.16	26.98	0.032
25	40.0	80.0	0.0	0.0	0.0	1.5290	0.000	3.3558	50.00	35.15	0.000
26	40.0	40.0	2.5	0.0	0.0	1.4974	-0.192	3.1190	53.06	29.10	-0.007
27	40.0	40.0	5.0	0.0	0.0	1.4978	-0.416	3.0598	54.85	28.58	0.000
28	40.0	40.0	7.5	0.0	0.0	1.4470	-0.518	2.9296	56.83	28.48	-0.041
29	40.0	40.0	10.0	0.0	0.0	1.3837	-0.651	2.8280	58.32	30.10	-0.067
30	40.0	40.0	12.5	0.0	0.0	1.3472	-0.788	2.6932	61.38	30.45	-0.093
31	40.0	40.0	15.0	0.0	0.0	1.3167	-0.894	2.6737	62.31	30.89	-0.132
32	40.0	40.0	0.0	0.0	2.538	1.4936	0.065	3.1978	50.51	29.16	-0.102
33	40.0	40.0	0.0	0.0	5.083	1.5097	0.120	3.2286	49.48	33.06	-0.201
34	40.0	40.0	0.0	0.0	7.6445	1.5175	0.190	3.2465	48.47	29.84	-0.295

Continued on next page

Table A.1 – *Continued from previous page*

ID	x					y					
	FRH $[mm]$	**RRH** $[mm]$	ψ [°]	ϕ [°]	δ [°]	$\mathbf{C_D.A}$	$\mathbf{C_Y.A}$	$\mathbf{-C_L.A}$	**Out** [%]	**Front** [%]	$\mathbf{C_{Mz}.A.b}$
35	40.0	40.0	0.0	0.0	10.232	1.5195	0.275	3.2311	47.87	29.73	-0.404
36	40.0	40.0	0.0	0.0	12.854	1.5081	0.334	3.1740	46.67	30.22	-0.487
37	30.0	30.0	0.0	0.0	0.0	1.4632	0.000	2.9878	50.00	24.90	0.000
38	50.0	50.0	0.0	0.0	0.0	1.4974	0.000	3.5480	50.00	35.94	0.000
39	60.0	60.0	0.0	0.0	0.0	1.5450	0.000	3.5195	50.00	33.85	0.000
40	20.0	70.0	0.0	0.0	0.0	1.4565	0.000	3.0786	50.00	32.37	0.000
41	50.0	20.0	0.0	0.0	0.0	1.5014	0.000	3.1765	50.00	25.03	0.000
42	30.0	20.0	0.0	0.0	0.0	1.4921	0.000	3.0432	50.00	28.24	0.000
43	20.0	20.0	0.0	0.0	0.0	1.4126	0.000	2.8047	50.00	22.79	0.000
44	20.0	30.0	0.0	0.0	0.0	1.3950	0.000	2.7666	50.00	25.91	0.000
45	20.0	50.0	0.0	0.0	0.0	1.4454	0.000	3.0169	50.00	31.50	0.000
46	20.0	60.0	0.0	0.0	0.0	1.4871	0.000	3.1048	50.00	32.90	0.000
47	30.0	50.0	0.0	0.0	0.0	1.4627	0.000	3.0235	50.00	29.54	0.000
48	30.0	60.0	0.0	0.0	0.0	1.4499	0.000	3.3319	50.00	35.83	0.000
49	30.0	70.0	0.0	0.0	0.0	1.4546	0.000	3.2647	50.00	36.60	0.000
50	50.0	30.0	0.0	0.0	0.0	1.4969	0.000	3.2363	50.00	27.46	0.000
51	50.0	60.0	0.0	0.0	0.0	1.5452	0.000	3.4237	50.00	34.72	0.000
52	50.0	70.0	0.0	0.0	0.0	1.5378	0.000	3.3999	50.00	33.02	0.000
53	60.0	20.0	0.0	0.0	0.0	1.5328	0.000	3.2457	50.00	23.52	0.000
54	60.0	30.0	0.0	0.0	0.0	1.5451	0.000	3.2451	50.00	24.19	0.000
55	60.0	40.0	0.0	0.0	0.0	1.5661	0.000	3.4254	50.00	28.83	0.000
56	60.0	50.0	0.0	0.0	0.0	1.5604	0.000	3.3264	50.00	29.57	0.000
57	60.0	70.0	0.0	0.0	0.0	1.5628	0.000	3.4957	50.00	35.62	0.000
58	20.0	80.0	0.0	0.0	0.0	1.5007	0.000	3.0193	50.00	29.28	0.000
59	30.0	80.0	0.0	0.0	0.0	1.4852	0.000	3.3101	50.00	37.29	0.000
60	50.0	80.0	0.0	0.0	0.0	1.5402	0.000	3.3291	50.00	33.09	0.000
61	60.0	80.0	0.0	0.0	0.0	1.5532	0.000	3.4112	50.00	35.99	0.000
62	46.8	37.4	3.75	0.9	9.626	1.4856	-0.010	3.2795	49.60	29.38	-0.355
63	54.0	59.0	12.15	0.1	5.372	1.3376	-0.670	2.7305	59.46	31.41	-0.260
64	30.0	71.0	7.35	1.5	10.6215	1.4588	-0.201	2.9615	51.47	27.79	-0.404
65	55.6	32.6	9.15	1.6	7.875	1.3698	-0.417	2.8119	56.60	20.74	-0.286
66	29.2	24.2	3.15	0.98	5.1965	1.4634	-0.070	2.9774	51.72	27.76	-0.194
67	24.4	50.6	10.65	1.34	12.127	1.3733	-0.406	2.6675	54.73	27.66	-0.487
68	36.4	72.2	6.15	0.82	11.1265	1.4788	-0.199	3.2163	53.73	38.55	-0.406
69	38.8	48.2	11.85	1.86	8.127	1.3641	-0.538	2.7802	57.69	30.51	-0.332
70	59.6	56.6	11.25	0.94	9.3715	1.3502	-0.505	2.7072	57.01	27.37	-0.376
71	51.6	23.0	11.55	0.38	8.626	1.2898	-0.552	2.9494	55.77	24.04	-0.355
72	32.4	74.6	8.25	1.46	1.8775	1.4119	-0.448	2.9408	55.73	31.65	-0.083
73	58.0	33.8	0.75	0.7	4.373	1.5295	0.041	3.2720	48.00	27.40	-0.149
74	56.4	47.0	4.35	0.5	7.124	1.5392	-0.133	3.2566	50.76	28.21	-0.283
75	38.0	61.4	14.25	0.74	2.8755	1.3399	-0.834	2.8217	62.19	38.31	-0.195
76	52.4	65.0	3.45	0.46	10.8745	1.5144	0.002	3.2568	49.98	33.25	-0.401
77	27.6	77.0	10.95	0.02	1.6255	1.4170	-0.643	3.1789	57.46	40.48	-0.152

Continued on next page

Table A.1 – *Continued from previous page*

ID	$\mathbf{x}$					$\mathbf{y}$					
	FRH $[mm]$	**RRH** $[mm]$	ψ [°]	ϕ [°]	δ [°]	$\mathbf{C_D.A}$	$\mathbf{C_Y.A}$	$\mathbf{-C_L.A}$	**Out** [%]	**Front** [%]	$\mathbf{C_{Mz}.A.b}$
78	34.8	57.8	8.85	1.78	2.3715	1.4156	-0.493	2.7627	56.71	29.79	-0.100
79	54.8	35.0	14.85	1.94	1.374	1.2491	-0.848	2.2898	64.13	23.02	-0.121
80	42.8	31.4	1.05	1.02	2.6235	1.5144	-0.023	3.4335	50.34	31.69	-0.088
81	53.2	30.2	7.05	0.18	6.1225	1.4059	-0.380	3.1443	53.44	26.69	-0.237
82	41.2	68.6	1.35	0.3	4.6225	1.5696	0.042	3.6285	51.53	38.18	-0.187
83	22.0	26.6	14.55	0.78	11.622	1.2384	-0.619	2.3787	58.35	25.47	-0.490
84	58.8	79.4	0.45	1.82	6.3765	1.5835	0.215	3.3616	49.45	36.07	-0.234
85	50.0	25.4	10.35	0.06	1.1225	1.3073	-0.672	2.7055	58.76	26.55	-0.096
86	46.0	67.4	12.75	0.26	11.374	1.3686	-0.560	2.8539	57.04	33.13	-0.482
87	44.4	38.6	13.95	0.54	12.379	1.2483	-0.623	2.6030	58.15	26.24	-0.509
88	40.4	36.2	1.95	1.42	6.621	1.5212	0.053	3.3126	49.54	31.72	-0.236
89	28.4	41.0	6.45	1.18	0.625	1.4217	-0.455	2.8452	54.98	29.54	-0.024
90	42.0	62.6	5.25	1.22	3.375	1.5181	-0.266	3.2016	55.56	33.55	-0.139
91	25.2	44.6	12.45	0.86	5.625	1.2948	-0.652	2.7111	58.78	33.42	-0.274
92	45.2	43.4	8.55	1.54	8.878	1.4147	-0.361	3.0094	55.65	28.36	-0.327
93	22.8	63.8	13.35	0.34	3.622	1.3525	-0.733	2.8513	58.49	35.76	-0.223
94	31.6	60.2	4.65	1.62	9.126	1.4801	-0.054	3.0770	49.73	29.72	-0.314
95	21.2	49.4	5.55	0.42	9.8715	1.4561	-0.164	3.1876	52.22	35.11	-0.373
96	26.8	78.2	2.85	0.6	2.125	1.5216	-0.114	3.2658	50.95	32.83	-0.080
97	43.6	39.8	1.65	0.22	0.875	1.5120	-0.114	3.2489	51.24	31.47	-0.030
98	48.4	66.2	13.65	1.26	4.1275	1.3208	-0.760	2.7176	61.87	35.76	-0.208
99	33.2	69.8	9.45	1.3	4.875	1.4213	-0.478	2.9218	55.95	33.53	-0.214
100	57.2	54.2	10.05	1.66	5.872	1.3997	-0.499	2.8250	57.98	28.54	-0.239
101	20.4	45.8	2.55	0.14	7.625	1.4674	0.023	3.1728	49.05	34.45	-0.307
102	30.8	29.0	13.05	1.7	0.375	1.2907	-0.753	2.6679	60.45	31.31	-0.072
103	23.6	21.8	9.75	1.3	3.8755	1.3510	-0.521	2.6766	58.88	27.08	-0.156
104	49.2	53.0	6.75	1.14	10.375	1.4371	-0.210	3.0319	53.18	29.48	-0.392
105	50.8	73.4	7.95	0.66	0.125	1.5081	-0.532	3.1240	59.04	35.14	-0.046
106	34.0	75.8	7.65	1.06	11.871	1.5115	-0.256	3.1179	53.60	34.16	-0.448
107	26.0	20.6	0.15	0.62	10.125	1.4720	0.248	2.9699	47.12	27.89	-0.350
108	35.6	55.4	4.95	1.1	7.375	1.5409	-0.157	3.3469	53.02	34.55	-0.267
109	37.2	51.8	2.25	1.38	8.375	1.5528	0.105	3.4450	49.97	35.90	-0.319
110	39.6	27.8	4.05	1.58	3.125	1.4734	-0.233	3.1720	52.38	30.28	-0.089
111	47.6	42.2	5.85	1.74	6.8755	1.4828	-0.199	3.1793	53.51	28.41	-0.254
112	38.3	22.0	1.0	0.39	0.0	1.4737	0.075	3.1661	49.53	27.32	-0.011
113	45.0	35.4	1.0	0.326	0.0	1.5086	0.070	3.2118	48.57	29.64	-0.005
114	49.9	43.0	1.0	0.46	0.0	1.5410	0.089	3.4017	49.68	31.80	-0.007
115	48.3	35.0	1.0	0.783	0.0	1.5194	-0.102	3.1828	50.62	28.10	-0.026
116	43.3	27.3	1.0	0.655	0.0	1.5055	-0.101	3.2036	50.47	27.61	-0.014

A.2 Results

$$
\underbrace{\begin{bmatrix} C_D.A \\ C_Y.A \\ -C_L.A \\ Bal\,[\%] - Out \\ Bal\,[\%] - Front \\ C_{Mz}.A.b \end{bmatrix}}_{\hat{\boldsymbol{f}}}
=
\underbrace{\begin{bmatrix}
1.3225 & 0.0092525 & 2.0797 & 50.3087 & 18.0373 & 0.019904 \\
0.0040983 & 0.00040121 & 0.031531 & 0.03227 & 0.25895 & -0.00068258 \\
0.0009701 & -0.00045281 & 0.0085836 & -0.036386 & 0.15816 & -0.00035564 \\
0.0034308 & -0.074534 & 0.026217 & 0.82502 & 0.29307 & -0.0039085 \\
0.018779 & -0.001836 & 0.1034 & -1.6456 & 1.6198 & 0.033951 \\
0.0066618 & 0.024799 & 0.048496 & -0.054187 & 0.926 & -0.038518 \\
-4.716 \times 10^{-6} & -4.5532 \times 10^{-7} & -8.1955 \times 10^{-5} & 0.0010873 & 0.0024456 & 1.6048 \times 10^{-6} \\
-0.00020473 & -9.4447 \times 10^{-5} & -0.00093097 & 0.0033418 & -0.01263 & 6.504 \times 10^{-5} \\
0.00063677 & 0.00023588 & 0.0019702 & 0.035123 & 0.060052 & -0.00056083 \\
-0.00015694 & 1.1562 \times 10^{-5} & -0.00026495 & -0.0046363 & -0.0091112 & 3.0529 \times 10^{-5} \\
7.2088 \times 10^{-5} & -1.3983 \times 10^{-5} & -2.3425 \times 10^{-5} & -0.001248 & 0.0020487 & -9.4857 \times 10^{-6} \\
-0.00036556 & 0.00054645 & -0.0029023 & -0.0032019 & -0.060223 & -1.9296 \times 10^{-5} \\
8.0103 \times 10^{-5} & -1.9935 \times 10^{-5} & 0.00020373 & 0.0018843 & 0.0076417 & -2.2927 \times 10^{-5} \\
-0.00074869 & -0.0004287 & -0.0025126 & 0.08357 & -0.035523 & 0.00062124 \\
-0.00059635 & -0.00042217 & -0.00084686 & -0.0063881 & -0.032995 & 0.00031132 \\
0.0021642 & 0.00051953 & 0.0069771 & -0.011353 & -0.011244 & -3.9408 \times 10^{-5} \\
-1.5815 \times 10^{-5} & -4.5226 \times 10^{-6} & -0.00022188 & -0.0010983 & -0.0045911 & 6.9853 \times 10^{-6} \\
-6.6173 \times 10^{-7} & 3.7769 \times 10^{-6} & -3.9984 \times 10^{-6} & -9.7591 \times 10^{-6} & -0.00087591 & 3.025 \times 10^{-6} \\
-0.00079359 & 0.0012339 & -0.0018687 & -0.0048986 & 0.018499 & -0.00043352 \\
-0.019863 & -0.0029673 & -0.089235 & -0.13373 & -1.5823 & 0.0024393 \\
-0.00017183 & 4.1506 \times 10^{-5} & -0.0037686 & -0.0095627 & -0.069302 & 4.0068 \times 10^{-5}
\end{bmatrix}}_{\hat{\boldsymbol{\beta}}}
\times
\underbrace{\begin{bmatrix}
1 \\
FRH \\
RRH \\
\psi \\
\phi \\
\delta \\
FRH \times RRH \\
FRH \times \psi \\
FRH \times \phi \\
FRH \times \delta \\
RRH \times \psi \\
RRH \times \phi \\
RRH \times \delta \\
\psi \times \phi \\
\psi \times \delta \\
\phi \times \delta \\
FRH^2 \\
RRH^2 \\
\psi^2 \\
\phi^2 \\
\delta^2
\end{bmatrix}}_{\boldsymbol{X}}^{\mathrm{T}}
\tag{A.1}
$$

A.3 Parametric Results

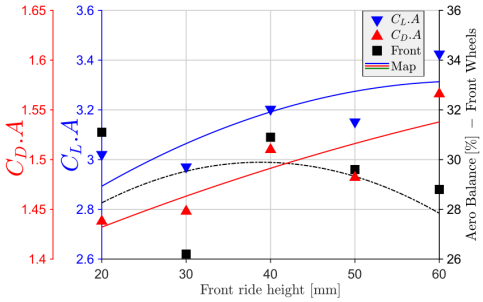

(a) Front ride height - $RRH = 40mm$

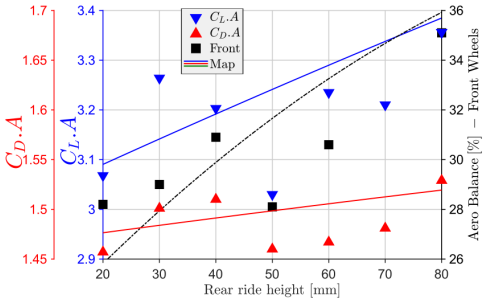

(b) Rear ride height - $FRH = 40mm$

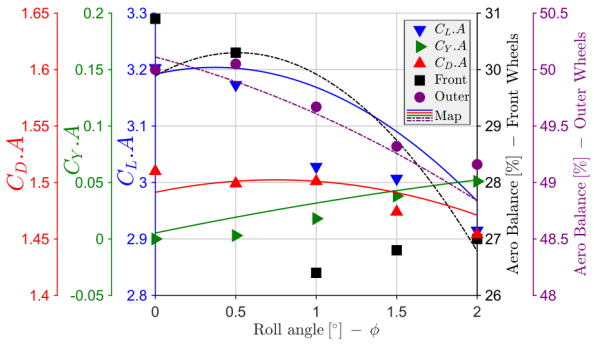

(c) Roll angle

Figure A.1: Comparison between results from surrogate and parametric studies

A.4 Yaw Angle Evolution of $-C_L.A$

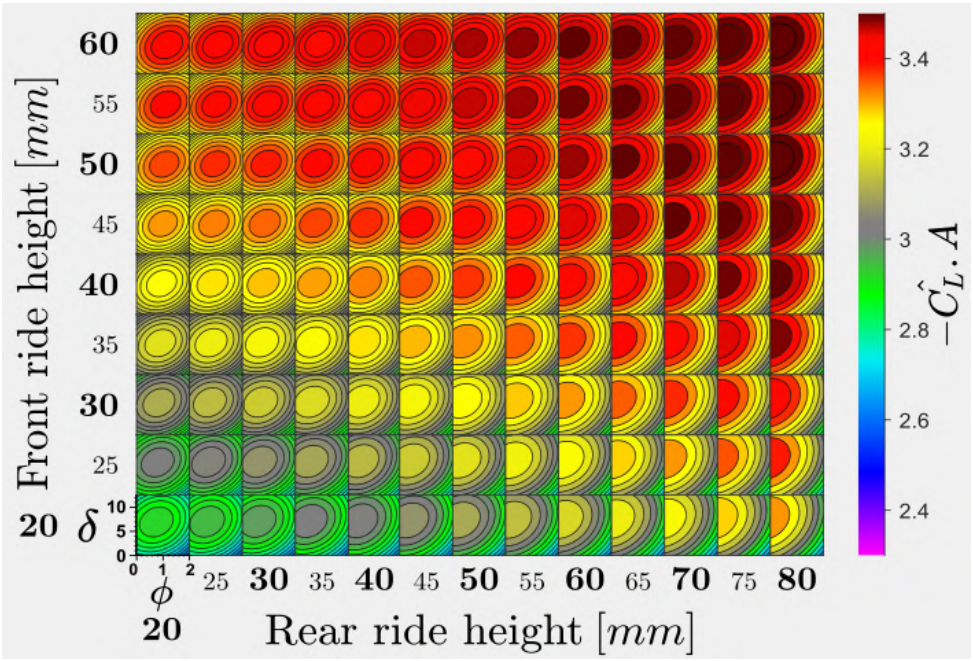

Figure A.2: Yaw angle $\psi = 0.0°$

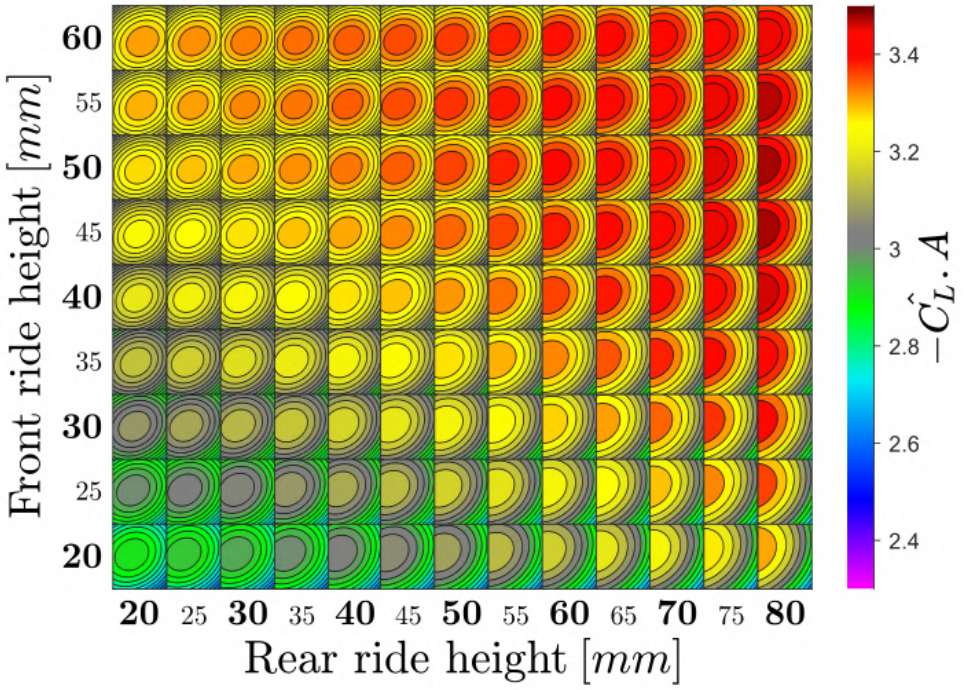

Figure A.3: Yaw angle $\psi = 2.5°$

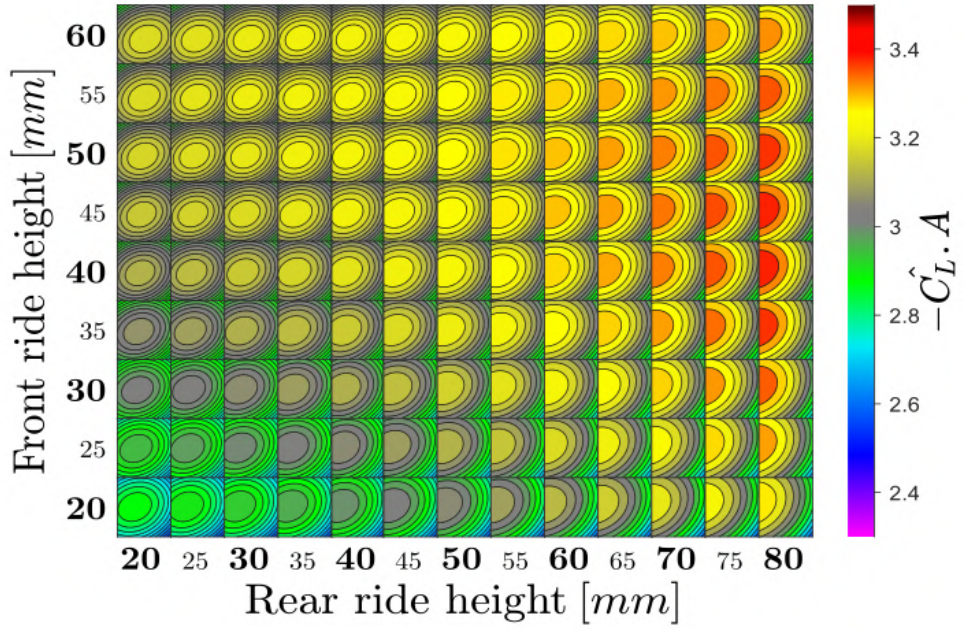

Figure A.4: Yaw angle $\psi = 5.0°$

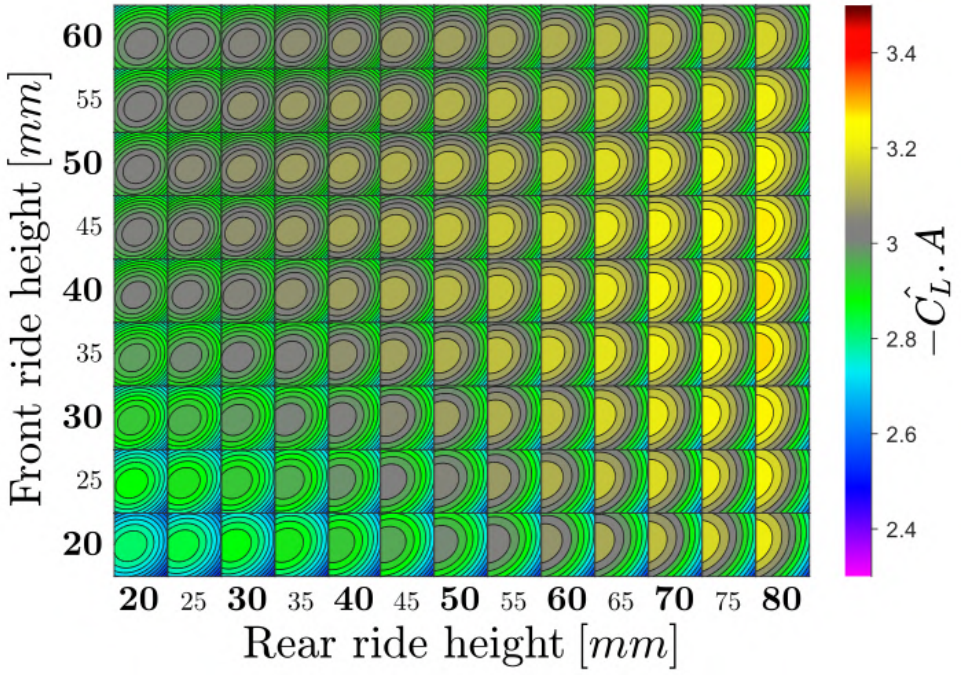

Figure A.5: Yaw angle $\psi = 7.5°$

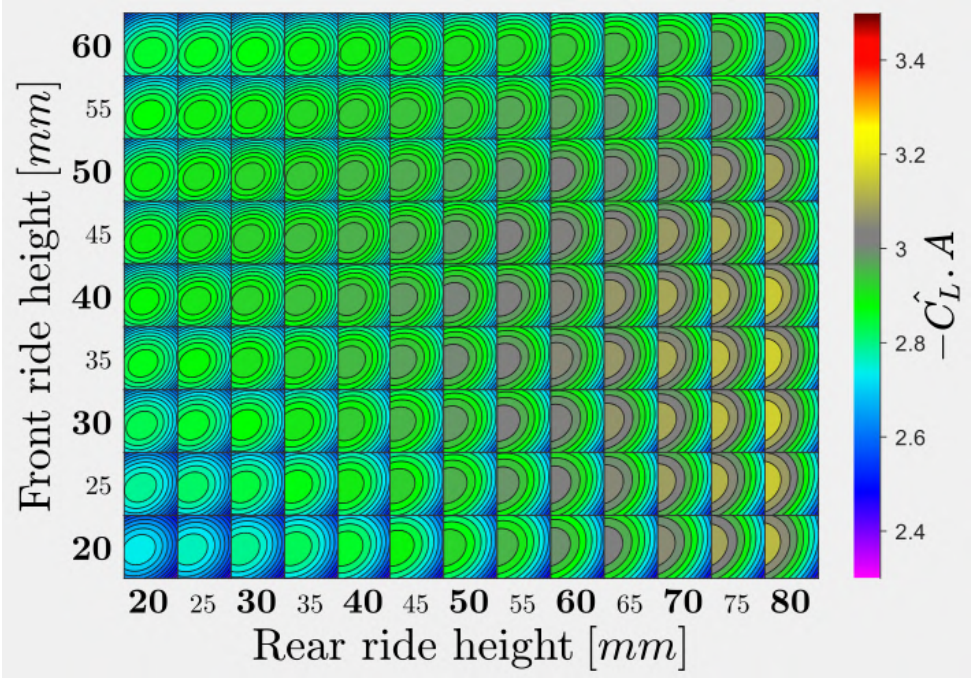

Figure A.6: Yaw angle $\psi = 10.0°$

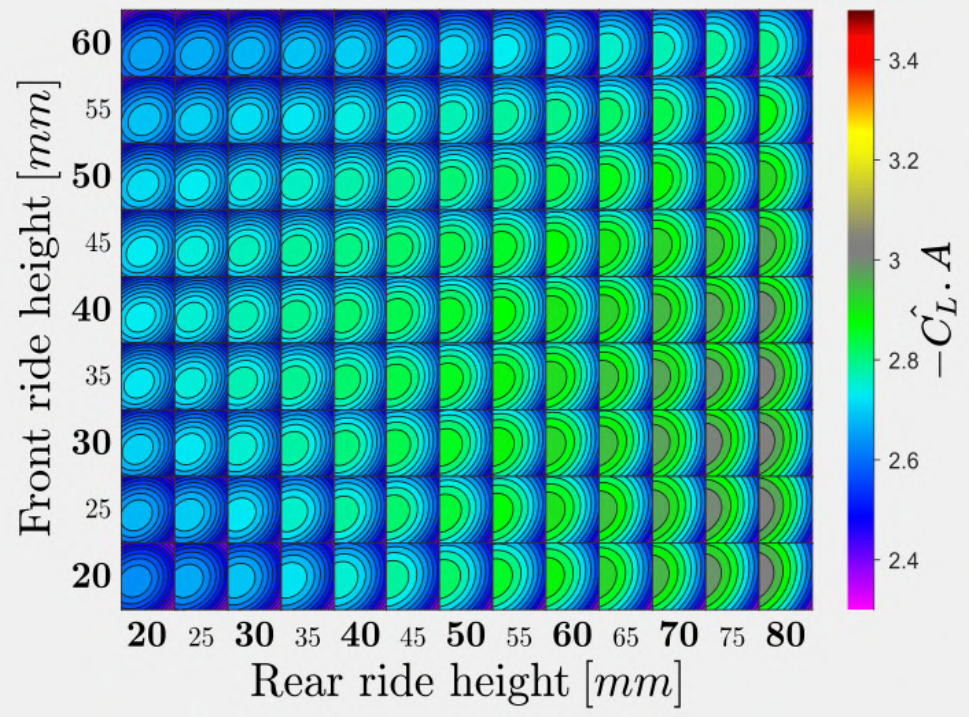

Figure A.7: Yaw angle $\psi = 12.5°$

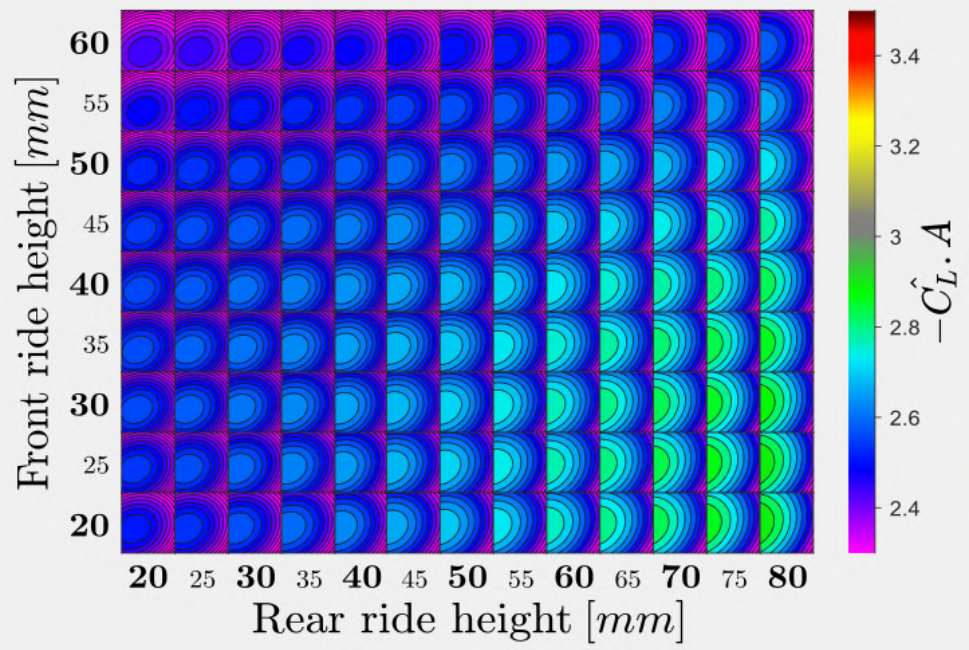

Figure A.8: Yaw angle $\psi = 15.0°$

Appendix B

Validation Results

B.1 Constant Speed Test Results

Table B.1: Constant speed results for every run

Att.	Run	Fr-RH $[mm]$	Rr-RH $[mm]$	Total-DF $[N]$	Fr-DF $[N]$	Rr-DF $[N]$	Bal. $[\%]$	$-C_L.A$	V_{air} $[km/h]$
1	1	49.89	43.01	643.36	163.78	479.58	25.46	2.803	70.57
	2	49.79	42.56	670.22	170.22	500.00	25.40	2.922	70.55
	3	50.11	43.35	613.67	150.13	463.56	24.46	2.673	70.58
	Avg.	49.93	42.97	642.42	161.38	481.05	25.11	2.799	70.57
2	1	38.24	22.40	540.12	106.12	434.00	19.65	2.447	69.21
	2	38.48	21.91	548.55	91.64	456.91	16.71	2.437	69.88
	3	38.14	21.51	588.27	112.73	475.54	19.16	2.604	70.02
	Avg.	38.29	21.94	558.98	103.50	455.48	18.51	2.496	69.70
3	1	45.23	35.82	412.91	69.64	343.27	16.87	1.838	69.82
	2	44.98	35.58	439.52	84.81	354.71	19.30	1.960	69.75
	3	44.79	34.60	497.48	97.39	400.09	19.58	2.210	69.90
	Avg.	45.00	35.34	449.97	83.95	366.02	18.58	2.003	69.82
4	1	48.31	35.22	1071.43	251.86	819.57	23.51	1.977	108.44
	2	48.22	35.13	1080.71	257.35	823.37	23.81	1.993	108.47
	3	48.36	34.73	1090.12	248.91	841.22	22.83	2.014	108.38
	Avg.	48.30	35.03	1080.75	252.71	828.05	23.38	1.995	108.43
5	1	37.35	14.54	935.27	153.02	782.25	16.36	1.751	107.66
	2	37.36	14.79	923.06	152.26	770.80	16.50	1.715	108.07
	3	37.84	14.94	887.15	122.70	764.46	13.83	1.656	107.82
	Avg.	37.52	14.76	915.16	142.66	772.50	15.56	1.707	107.85
6	1	43.29	27.14	908.94	180.18	728.77	19.82	1.693	107.92
	2	43.41	27.26	896.63	173.20	723.42	19.32	1.673	107.85
	3	43.33	27.46	892.93	178.16	714.77	19.95	1.702	106.71
	Avg.	43.35	27.29	899.5	177.18	722.32	19.70	1.689	107.49

B.2 Additional Information

Table B.2: Additional measurements

Corner	Mass $[kg]$	Static camber $[°]$
FL	68.40	-2.7
FR	75.80	-2.2
RL	83.85	-2.4
RR	76.15	-2.0

Moment of inertia of each wheel package $I_{wheel} = 148243101.7[g.mm^2]$ measured in CAD include tyre, rim, brake disk, centre lock, hub and transmission parts.

B.3 Coast Down Results

Table B.3: Coast down results for every run

Att.	Run	Fr-RH $[mm]$	Rr-RH $[mm]$	$C_D.A$	$\sigma[mm]$ Fr-RH	Rr-RH
1	1	52.11	52.87	1.418	1.00	1.85
	2	52.07	52.78	1.995	1.14	2.06
	3	52.22	53.10	1.436	0.97	1.61
	Avg.	52.13	52.91	1.616	1.04	1.84
2	1	40.04	31.08	1.296	0.93	1.69
	2	39.95	30.61	1.773	0.93	1.84
	3	39.95	30.60	1.729	0.89	1.93
	Avg.	39.98	30.76	1.599	0.92	1.82
3	1	46.78	44.52	0.790	0.99	1.69
	2	46.85	44.47	1.131	0.97	1.72
	3	46.77	43.98	1.251	1.01	1.91
	Avg.	46.80	44.32	1.057	0.99	1.77
4	1	51.15	49.98	1.716	1.98	4.30
	2	51.16	49.71	1.676	1.71	3.81
	3	51.04	49.12	2.069	1.64	3.91
	Avg.	51.12	49.60	1.820	1.78	4.01
5	1	39.14	27.73	2.185	1.33	3.56
	2	39.11	27.34	1.187	1.37	3.55
	3	39.46	28.29	2.528	1.15	3.07
	Avg.	39.24	27.78	1.967	1.29	3.39
6	1	45.78	41.14	1.729	1.59	3.68
	2	45.76	41.37	1.503	1.76	3.97
	3			Aborted		
	Avg.	45.77	41.26	1.616	1.67	3.82

B.4 Example Constant Speed and Coast Down Runs Data

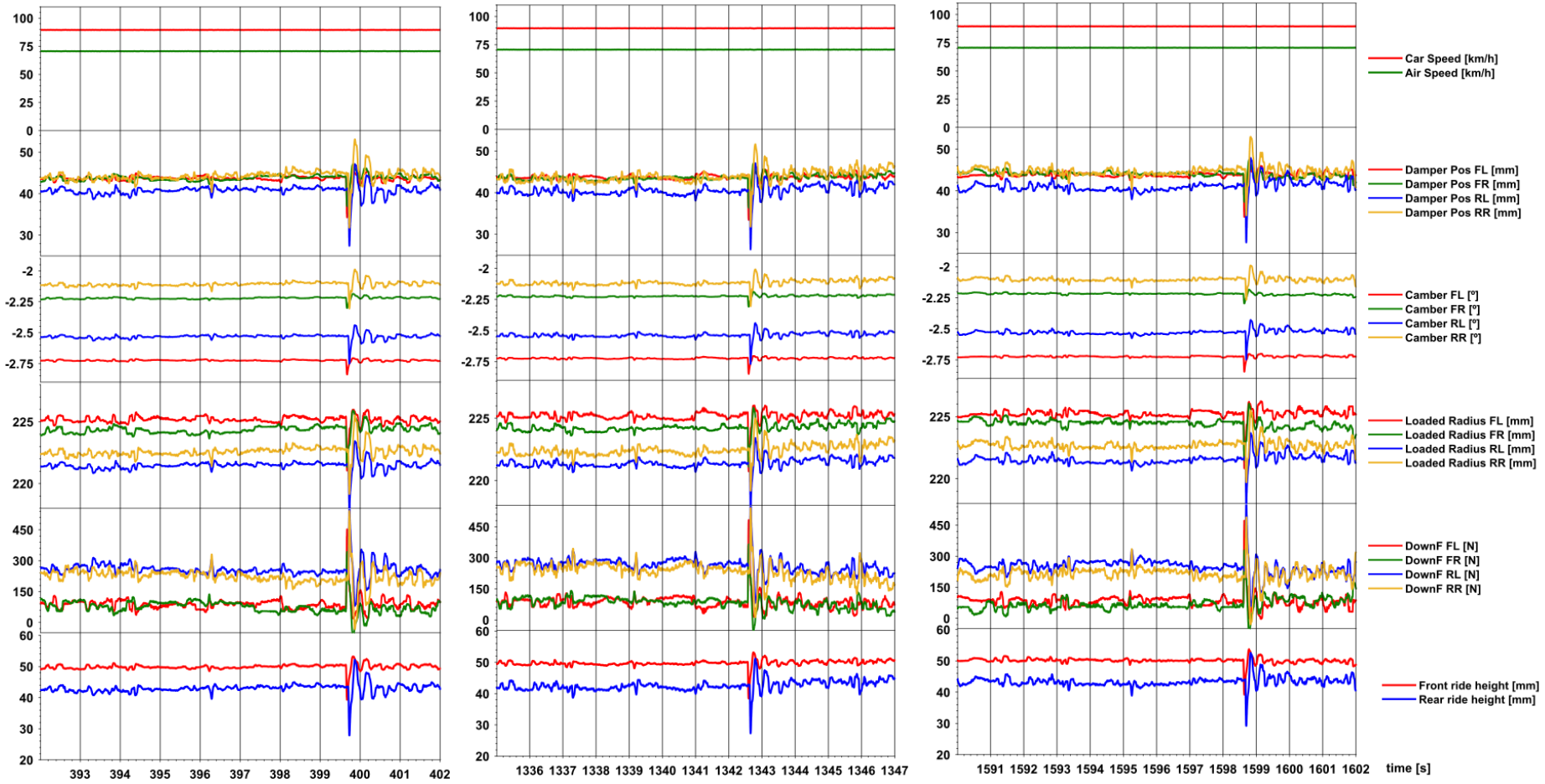

(a) Setup 1 Run 1 (b) Setup 1 Run 3 (c) Setup 1 Run 5

Figure B.1: Full runs for Setup 1 - Tailwind runs corresponding to attitude 1

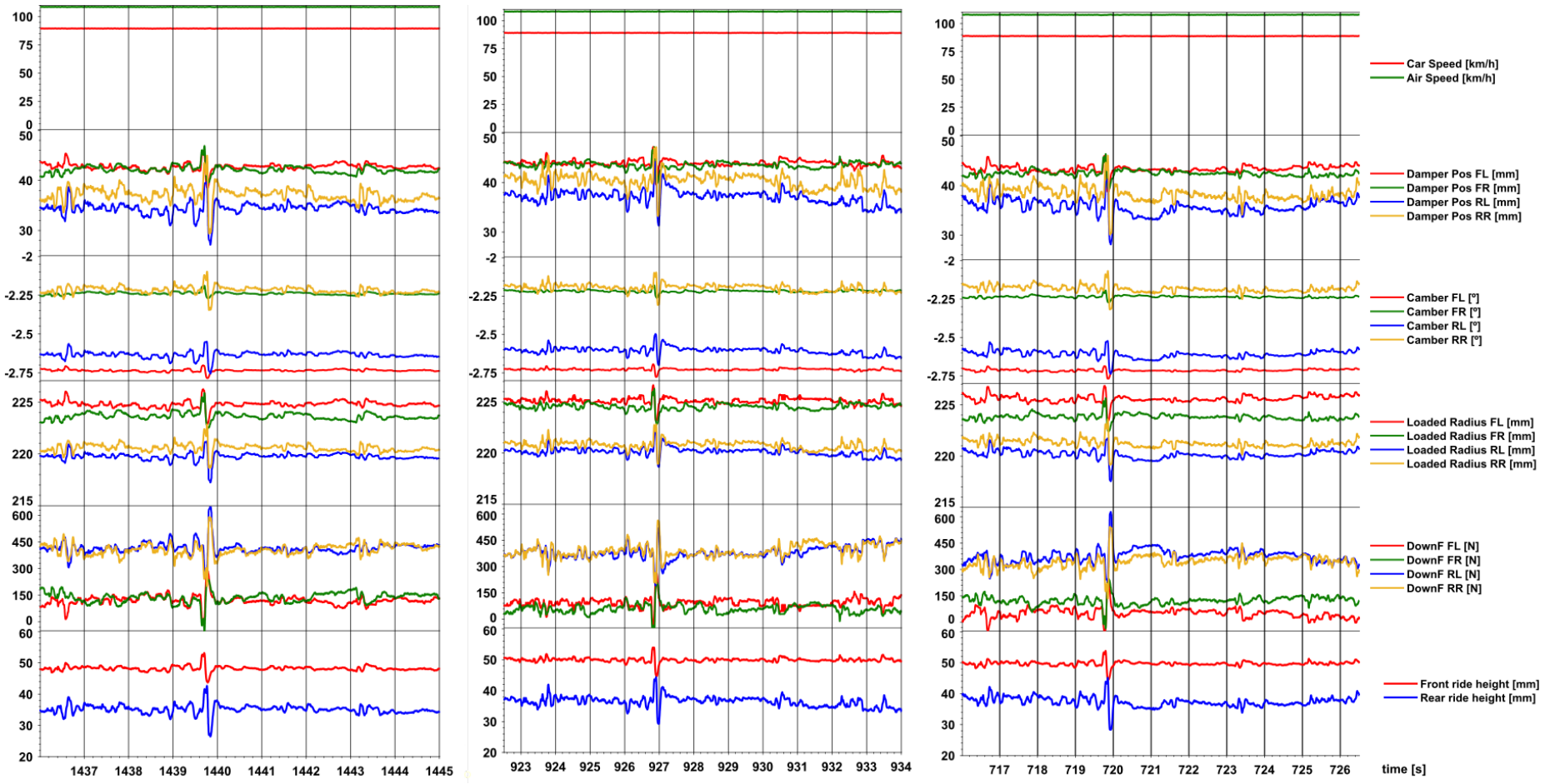

(a) Setup 1 Run 4

(b) Setup 2 Run 4

(c) Setup 3 Run 4

Figure B.2: Example Runs 4 corresponding to headwind condition

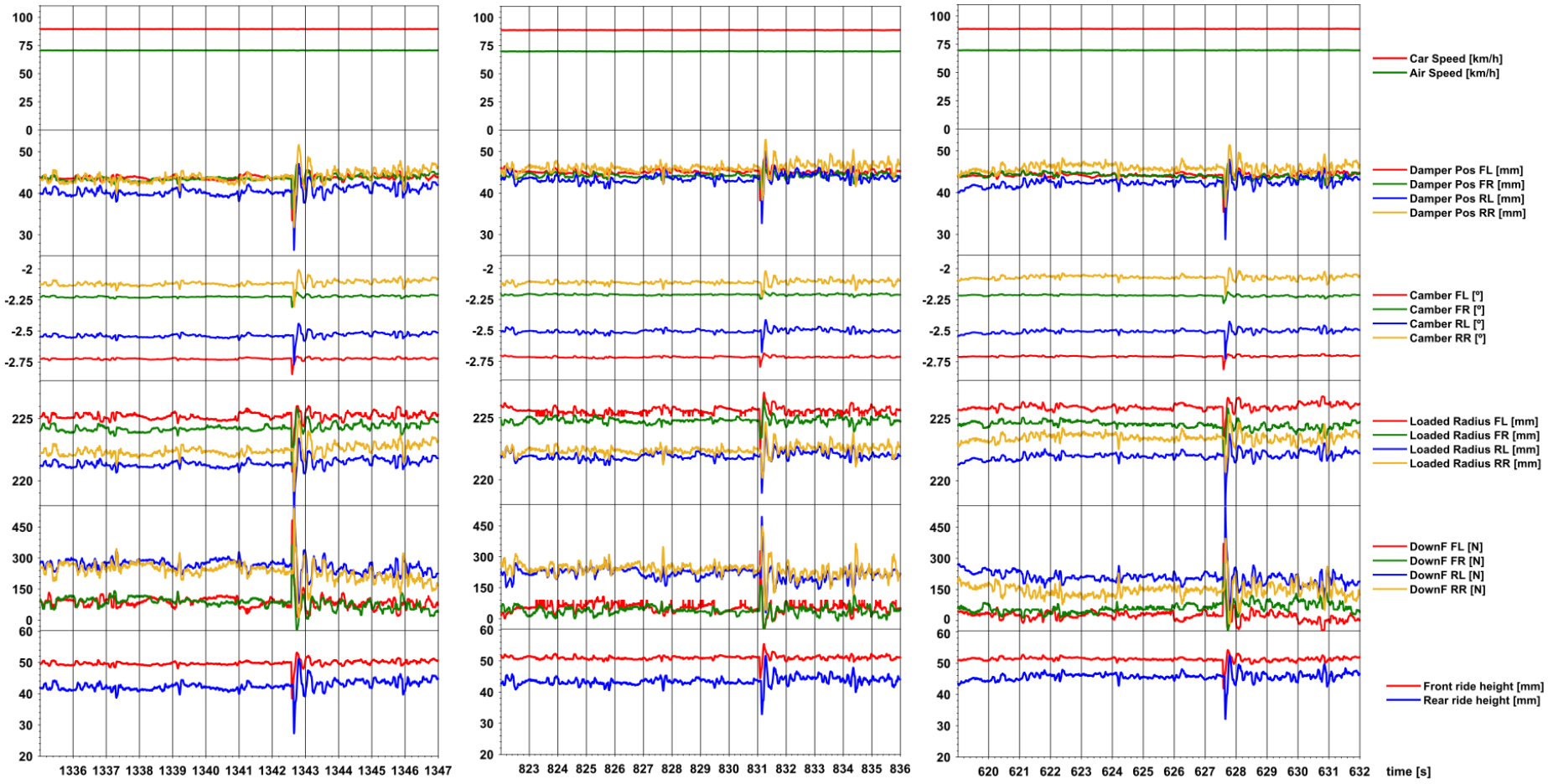

(a) Setup 1 Run 3 (b) Setup 2 Run 3 (c) Setup 3 Run 3

Figure B.3: Examples Runs 3 corresponding to tailwind condition

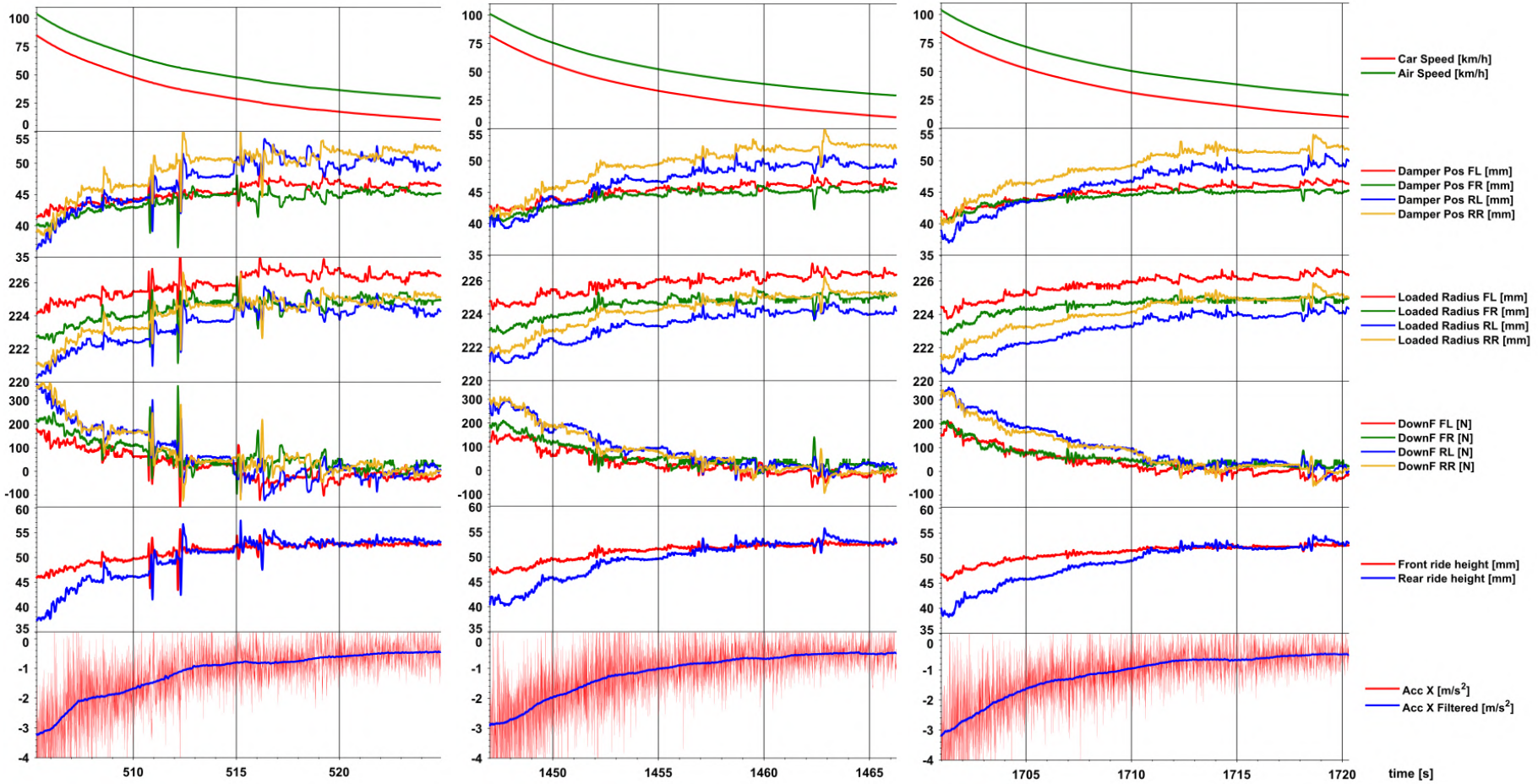

(a) Setup 1 Run 2 (b) Setup 1 Run 4 (c) Setup 1 Run 6

Figure B.4: Full runs for Setup 1 - Headwind runs corresponding to attitude 4

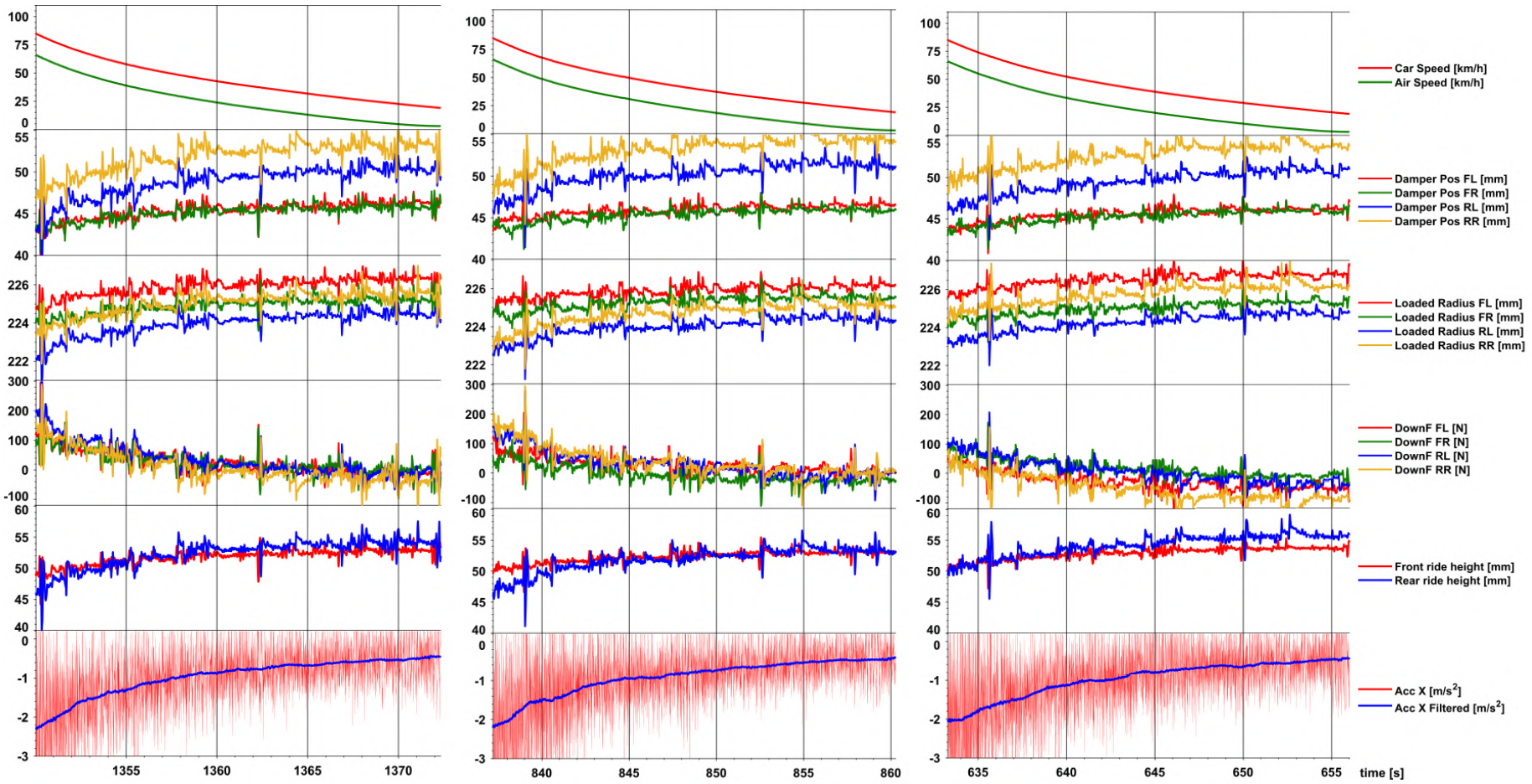

(a) Setup 1 Run 3

(b) Setup 2 Run 3

(c) Setup 3 Run 3

Figure B.5: Examples Runs 3 corresponding to tailwind condition

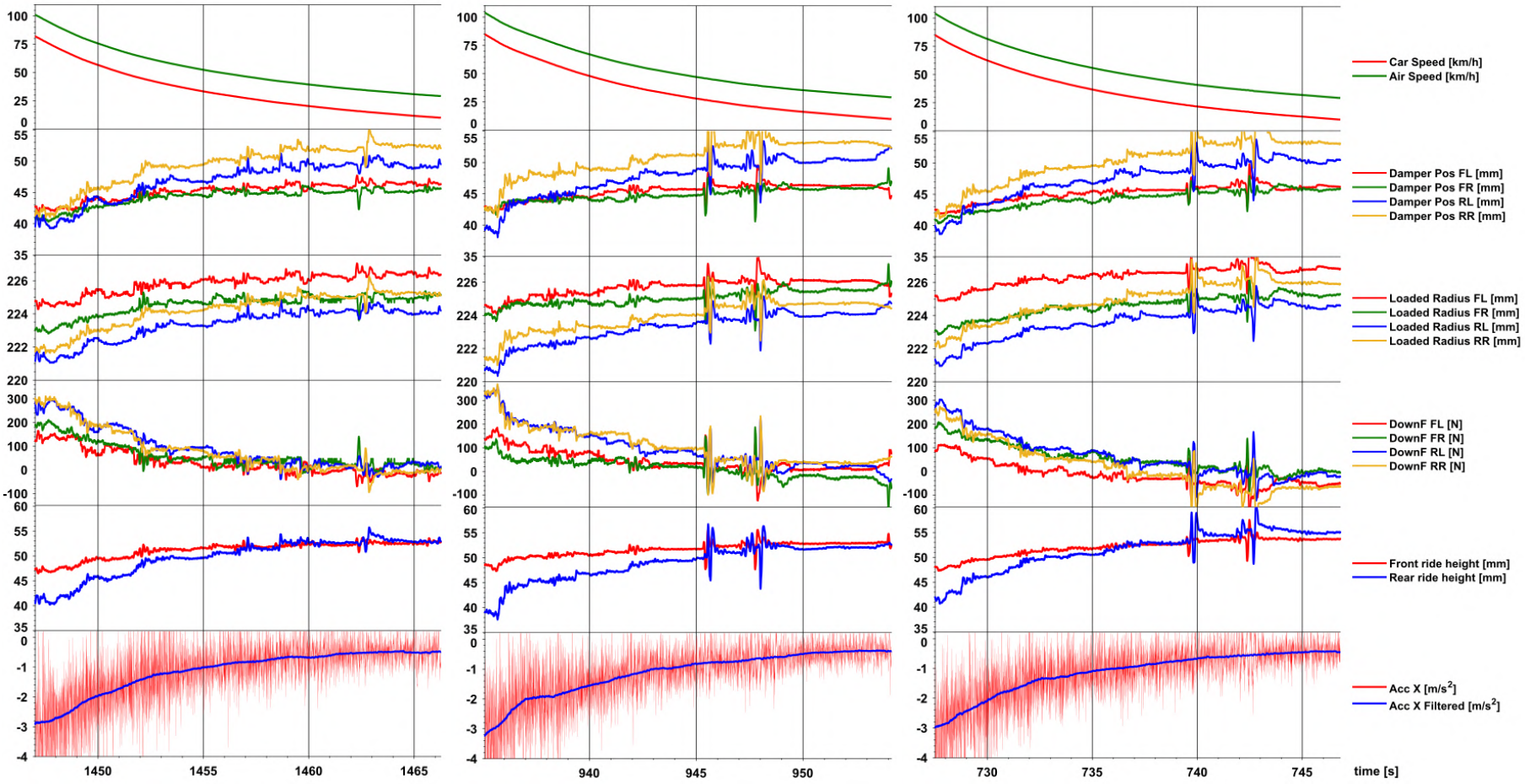

(a) Setup 1 Run 4 (b) Setup 2 Run 4 (c) Setup 3 Run 4

Figure B.6: Examples Runs 4 corresponding to headwind condition

B.5 Suspension Kinematics

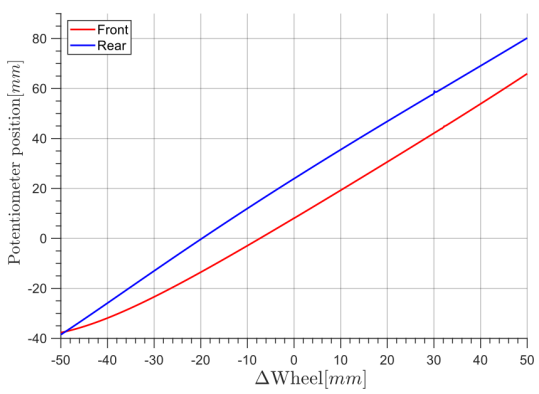

(a) Potentiometer position

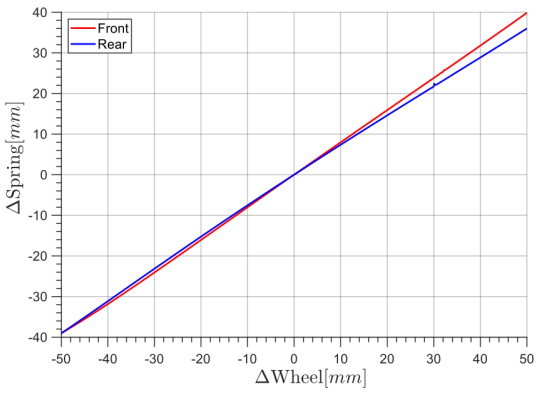

(b) Spring

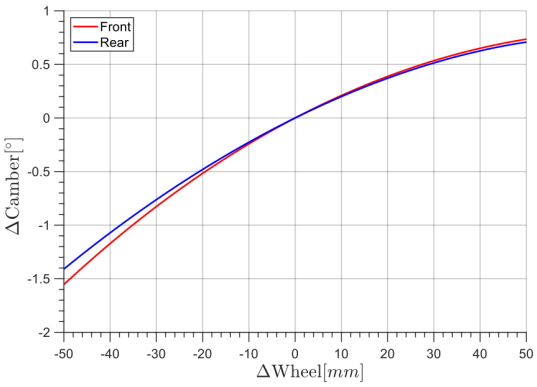

(c) Camber angle

Figure B.7: Suspension kinematics based on wheel travel for $\pm 50mm$ heave